

Examining the human influence on global climate using an empirical model

Austin Patrick Hope¹, Laura Anne McBride¹, Timothy P. Canty¹, Brian F Bennett¹, Walter R Tribett¹, and Ross J. Salawitch¹

¹University of Maryland, College Park

November 26, 2022

Abstract

We use the Empirical Model of Global Climate (EM-GC) to show that human activity has been responsible for ~ 0.14 °C/decade (range: 0.08 to 0.20) of warming from 1979 to 2010. This EM-GC based quantification of Attributable Anthropogenic Warming Rate (AAWR) is constrained by the observed global mean surface temperature and ocean heat content records; the largest contribution to the uncertainty in our estimate of AAWR is imprecise knowledge of the radiative forcing due to tropospheric aerosols (AER RF). Our value of AAWR is noticeably lower than the mean value from the IPCC 2013 models, 0.22 °C/decade (range: 0.08 to 0.32) with no overlap of interquartile ranges. We also compute probabilistic forecasts of the rise in GMST where again the largest source of uncertainty is AER RF, and cast results in terms of the likelihood of achieving either 1.5 °C or 2.0 °C warmings relative to pre-industrial. We show that the likelihoods of limiting global warming to 2°C are 92%, 50%, and 20% if greenhouse gases follow the RCP 2.6, 4.5, and 6.0 scenarios; the likelihoods of limiting warming to 1.5°C drop to 67%, 10%, and 0.1% for these same three RCPs. Warming forecasts based upon our EM-GC are more optimistic than found by CMIP5 GCMs, following how many GCMs exhibit faster warming than inferred from the recent climate record. Our EM-GC forecasts show that aggressive controls on emissions of both CO₂ and CH₄ starting this decade are needed to limit global warming to 1.5°C with high probability.

Hosted file

hope_etal20_v3a_supp.docx available at <https://authorea.com/users/555273/articles/605950-examining-the-human-influence-on-global-climate-using-an-empirical-model>

1
2
3
4
5
6
7
8
9
10
11
12
13
14
15
16
17
18
19
20
21
22

Examining the human influence on global climate using an empirical model

Austin P. Hope¹, Laura A. McBride², Timothy P. Canty¹, Brian F. Bennett¹, Walter R. Tribett¹, Ross J. Salawitch^{1,2,3}

¹Department of Atmospheric and Oceanic Sciences, University of Maryland- College Park, College Park, 20740, USA

²Department of Chemistry and Biochemistry, University of Maryland -College Park, College Park, 20740, USA

³Earth System Science Interdisciplinary Center, University of Maryland -College Park, College Park, 20740, USA

Correspondence to: Austin P Hope (ahope12@umd.edu)

Key Points

- We use an observationally-driven simple climate model to argue with multiple lines of evidence that global climate models warm too quickly
- We unequivocally agree that greenhouse gas emissions must be limited soon to avoid extreme global warming
- Achieving the goals of the Paris Agreement is more likely than global climate models suggest but still requires significant global effort

23

24 **Abstract**

25 We use the Empirical Model of Global Climate (EM-GC) to show that human activity has been
26 responsible for ~ 0.14 °C/decade (range: 0.08 to 0.20) of warming from 1979 to 2010. This EM-
27 GC based quantification of Attributable Anthropogenic Warming Rate (AAWR) is constrained
28 by the observed global mean surface temperature and ocean heat content records; the largest
29 contribution to the uncertainty in our estimate of AAWR is imprecise knowledge of the radiative
30 forcing due to tropospheric aerosols (AER RF). Our value of AAWR is noticeably lower than the
31 mean value from the IPCC 2013 models, 0.22 °C/decade (range: 0.08 to 0.32) with no overlap of
32 interquartile ranges. We also compute probabilistic forecasts of the rise in GMST where again
33 the largest source of uncertainty is AER RF, and cast results in terms of the likelihood of
34 achieving either 1.5 °C or 2.0 °C warmings relative to pre-industrial. We show that the
35 likelihoods of limiting global warming to 2 °C are 92%, 50%, and 20% if greenhouse gases
36 follow the RCP 2.6, 4.5, and 6.0 scenarios; the likelihoods of limiting warming to 1.5 °C drop to
37 67%, 10%, and 0.1% for these same three RCPs. Warming forecasts based upon our EM-GC are
38 more optimistic than found by CMIP5 GCMs, following how many GCMs exhibit faster
39 warming than inferred from the recent climate record. Our EM-GC forecasts show that
40 aggressive controls on emissions of both CO_2 and CH_4 starting this decade are needed to limit
41 global warming to 1.5 °C with high probability.

42

43 **Plain Language Summary**

44 We use a simple climate model based on observations, the Empirical Model of Global Climate,
45 to quantify past and future global warming due to human activity. Warming is driven by the
46 release of greenhouse gases; the largest source of uncertainty in the human contribution to
47 warming is due aerosols, small suspended particles that cool the planet by an amount that is not
48 well known. We compare our results to more complex global climate models that are shown to
49 warm faster than observed over the prior few decades. This pattern persists with projections of
50 future temperature: while our model produces a wide range of future temperatures due to the
51 relatively unknown strength of aerosol cooling, our ensemble generally produces lower
52 temperatures by year 2100 than given by these more complex climate models. As such, our
53 global warming forecasts provide a more optimistic view that society can keep global warming

54 beneath the thresholds set by the Paris Climate Agreement. Nonetheless, to achieve the target of
55 the Paris Climate Agreement, society must greatly reduce its dependence on fossil fuels within
56 this decade whereas to achieve the upper limit of this agreement, society must greatly limit fossil
57 fuel emissions within the next two decades.

58

59 **1. Introduction**

60 Changes in Earth’s climate on the decadal to century timescales are influenced by both
61 anthropogenic and natural factors. Anthropogenic factors include rising concentrations of
62 greenhouse gases (GHGs) that cause global warming (Lean & Rind, 2008; Santer et al., 2013)
63 and increased burdens of tropospheric aerosols (hereafter, aerosols) that offset a portion of the
64 GHG-induced warming (Bond et al., 2013; Kiehl, 2007; Smith & Bond, 2014; Stocker et al.,
65 2013). Natural factors often cited as having a significant influence on global climate include the
66 El Niño-Southern Oscillation (ENSO), the approximately 11-year solar cycle (total solar
67 irradiance, TSI), and increases in the stratospheric aerosol optical depth (SAOD) that are the
68 result of powerful volcanic eruptions (Chylek et al., 2016; Foster & Rahmstorf, 2011; Lean &
69 Rind, 2008; Santer et al., 2013). Variations in total ocean heat content (OHC), the strength of the
70 Atlantic Meridional Overturning Circulation (AMOC), and regional oceanic patterns like the
71 Pacific Decadal Oscillation (PDO) and the Indian Ocean Dipole (IOD) also can influence global
72 climate, though the extent each of these effects has on climate lacks consensus (Andronova &
73 Schlesinger, 2000; Chylek et al., 2014; England et al., 2014; Rahmstorf et al., 2015; Rose et al.,
74 2014; Saji et al., 1999; Steinman et al., 2015; Tokarska et al., 2019; Tung & Zhou, 2013).
75 Feedbacks within the climate system driven by changes in atmospheric water vapor, lapse rate,
76 clouds, and the surface albedo in response to radiative forcing (RF) induced by GHGs and
77 aerosols also play a large role in the climate system (Andrews et al., 2012; Bony et al., 2006; Lin
78 et al., 2019; Sherwood et al., 2020; Zelinka et al., 2013; Zhou et al., 2015).

79 Our focus is on quantification of the human influence on global climate. We examine the
80 global monthly mean near surface air temperature anomaly relative to preindustrial (ΔT) from
81 four data centers, collected over the past century and a half; for the purposes of this paper, we
82 use a baseline of 1850-1900 as “preindustrial”. We quantify the human influence on ΔT , termed
83 the Attributable Anthropogenic Warming Rate (AAWR), using an Empirical Model of Global
84 Climate (EM-GC) (Canty et al., 2013; Hope et al., 2017) that represents all of the factors

85 described above. Our determination of AAWR is motivated by Box 10.1 of IPCC’s Fifth
86 Assessment Report, Working Group I (Stocker et al., 2013), except we divide their Attributable
87 Anthropogenic Warming (AAW, units of °C) by time to arrive at warming rate (units of
88 °C/decade). We primarily examine AAWR from the start of 1979 to the end of 2010 (hereafter
89 1979 to 2010) because AAW is nearly linear over this 32-year interval and this time period has
90 also been studied by several other papers (Foster & Rahmstorf, 2011; Stocker et al., 2013; Zhou
91 & Tung, 2013). We also quantify AAWR from archived output of the General Circulation
92 Models (GCMs) used throughout Stocker et al. (2013) – hereafter, AR5 – as part of Phase 5 of
93 the Climate Model Intercomparison Project (CMIP5) (Taylor et al., 2012).

94 Another key aspect of this study is projection of the rise in ΔT to year 2100 (ΔT_{2100}).
95 Here, we use values of key model parameters (i.e. ocean heat export efficiency and the sum of
96 climate feedback mechanisms, defined in section 2) obtained from fitting the historical climate
97 record to forecast how ΔT and total ocean heat content will rise based on prescribed
98 anthropogenic GHGs and aerosols. The projections focus solely on the anthropogenic component
99 of ΔT so that our model results can be related to the Paris Agreement (UNFCCC, 2015). The
100 agreement seeks to reduce future emissions of GHGs such that the increase in ΔT is “well below
101 2°C” and to “pursue efforts to limit the temperature increase to 1.5°C above preindustrial”
102 (UNFCCC, 2015). Of course, future ΔT will also be influenced by natural variability, including
103 TSI, ENSO, AMOC, and major volcanic eruptions (Chylek et al., 2016; Kavvada et al., 2013;
104 Lean & Rind, 2009). Although variations in TSI have been forecast and could therefore be used
105 in our projections, TSI exerts a relatively minor influence on ΔT (Lean & Rind, 2009; Zharkova
106 et al., 2015). Since the other natural factors cannot be reliably predicted over the coming
107 decades, we limit our projections of ΔT to the policy-relevant human component. Finally, the
108 projections of ΔT are also framed in terms of the cumulative amount of carbon that can be
109 emitted to achieve either the goal (1.5°C) or upper limit (2°C) of the Paris Agreement.

110

111 1.1 Previous estimates of AAWR

112 Multiple previous studies have examined AAWR, often focusing on 1979 to 2010 and
113 using multiple linear regression (MLR) to quantify natural and anthropogenic influences on ΔT .
114 Foster & Rahmstorf (2011) (FR11) suggested an AAWR of 0.170 ± 0.012 °C/decade based on
115 analysis of version 3 of the ΔT record provided by the Climate Research Unit (HadCRUT3,

116 hereafter CRU3) of East Anglia (Jones et al., 2012). They used MLR to remove the influence of
117 ENSO, SAOD, and TSI on observed ΔT , and then fit the residual to quantify AAWR. Similar
118 numerical values were reported for AAWR using ΔT from the Goddard Institute of Space
119 Sciences (GISS, version 4) (Hansen et al., 2010) and the National Centers for Environmental
120 Information (NCEI, blend of the Global Historical Climate Network-Monthly version 4 and the
121 International Comprehensive Ocean-Atmosphere Data Set release 3) (Smith et al., 2008). Zhou
122 & Tung (2013) (ZT13) examined version 4 of the CRU record (HadCRUT4, hereafter CRU4)
123 and also used an MLR/residual method and concluded AAWR was 0.169 ± 0.019 °C/decade if
124 temporal variations in the strength of the Atlantic Multidecadal Oscillation (AMO) are ignored.
125 Most importantly, ZT13 stated that AAWR was 0.070 ± 0.019 °C/decade upon consideration of
126 variations in the strength of the AMO. We highlight what we believe are shortcomings in the
127 approaches of the FR11 and ZT13 studies in section §3.2.

128 Recently, Christy & McNider (2017), hereafter CM17, examined lower-tropospheric
129 temperatures measured from satellite and radiosondes collected from the start of 1979 to the end
130 of 2017. They concluded AAWR is 0.096 ± 0.023 °C/decade over this time period. This estimate
131 covers a range of AAWR that includes the lower value of ZT13 but also suggests the value could
132 be much higher, between the two possibilities for AAWR given by ZT13. Similar to CM17, we
133 suggest the actual value of AAWR over 1979 to 2010 lies between the various estimates of FR11
134 and ZT13, though our value lies closer to the upper end of the range spanned between FR11 and
135 ZT13.

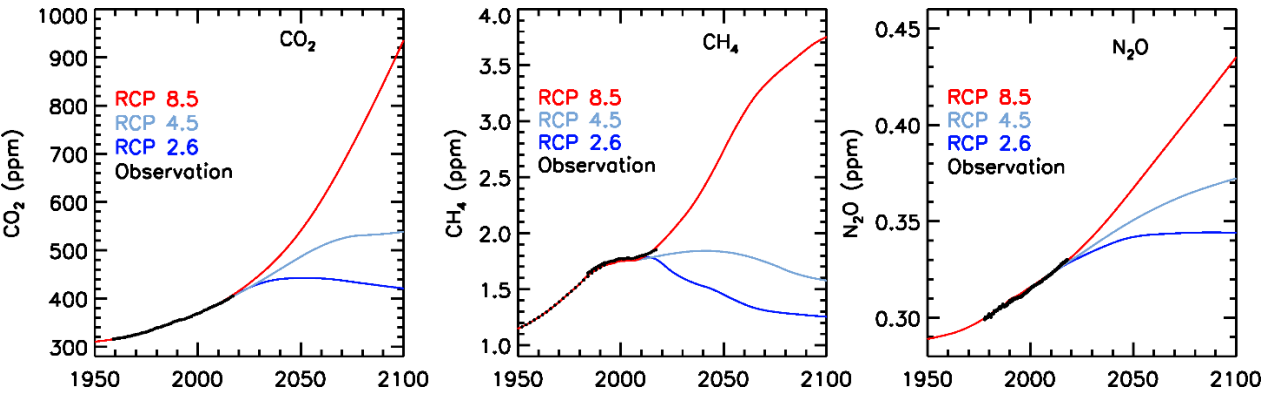
136

137 1.2 Prior projections of future temperature

138 While it is certain that continued emissions of GHGs will cause a rise in ΔT , future
139 warming is also subject to a wide range of uncertainties. One class of uncertainty, termed
140 scenario uncertainty, is dependent on future atmospheric abundances of GHGs and aerosols. The
141 CMIP5 community and AR5 adopted the Representative Concentration Pathways (RCPs) (Van
142 Vuuren, Edmonds, et al., 2011) of GHGs and aerosols as part of an effort to address scenario
143 uncertainty. Table SPM.2 of AR5 (IPCC, 2013) states that RCP 2.6 (Van Vuuren, Stehfest, et al.,
144 2011) would result in 1.6 ± 0.7 °C warming (5-95% of model range of projections) relative to
145 preindustrial temperature by the end of the 21st century, while RCP 8.5 (Riahi et al., 2011) would
146 result in a warming of 4.3 ± 1.1 °C.

147
148
149
150
151
152
153
154
155
156
157
158

In addition to the two extreme RCP scenarios of RCP 2.6 and RCP 8.5, our study also focuses on the RCP 4.5 scenario (Thomson et al., 2011). While we have also examined RCP 6.0 (Masui et al., 2011) we choose to not focus on RCP 6.0 for several reasons. First, there is significant overlap between the projections for RCP 4.5 and RCP 6.0 among the CMIP5 GCMs used by AR5: ΔT_{2100} values of 2.4 °C warming (1.7 °C to 3.2 °C, 5-95% of model range of projections) for RCP 4.5 compared to 2.8 °C warming (2.0 °C to 3.7 °C) for RCP 6.0. Second, the CMIP5 GCMs collectively ran many more simulations for RCP 4.5 than for RCP 6.0. Third, there is much more literature concerning RCP 4.5 for comparison to our results. The time evolution of atmospheric CO₂, CH₄, and N₂O for the three RCPs we consider, together with recent observed globally averaged mixing ratios, are shown in **Figure 1**.



159
160
161
162
163
164
165
166
167
168
169
170

Figure 1. Greenhouse gas abundances for CO₂, CH₄, and N₂O, 1950 to 2100, taken from the RCP scenarios. Each scenario’s GHG abundances are portrayed in a different color: red for RCP 8.5, light blue for RCP 4.5, and dark blue for RCP 2.6 (Meinshausen et al., 2011). These mixing ratio time series are combined with those of other minor GHGs to create the GHG RF times series used in this study. With the exception of CH₄, the RCP scenarios are visually hard to distinguish from each other between their divergence in 2005 and present, though their divergence becomes clear within the next ten years. Also shown for comparison are observations (black) for each GHG (data from <https://www.esrl.noaa.gov/gmd/ccgg/trends/>).

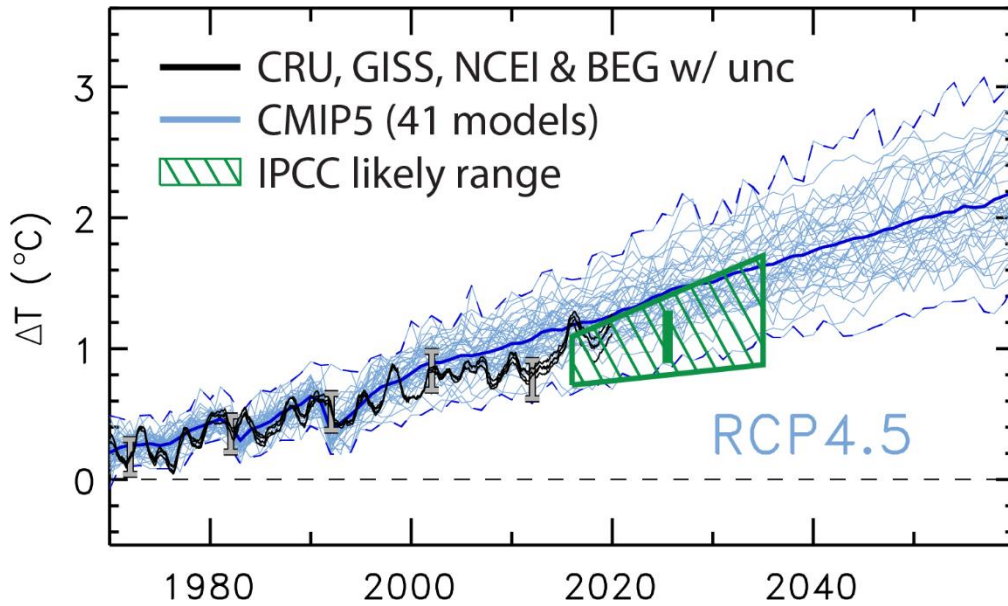
171 For a specific GHG scenario, such as RCP 4.5, there is a considerable range in end-of-
172 century warming among various CMIP5 GCMs (e.g., figure SPM.7 of AR5 (IPCC, 2013)), i.e.
173 model uncertainty. Primary drivers of these differences are uncertainties in climate feedback, the
174 radiative forcing of climate due to aerosols, and the uptake of heat by the oceans (Forster et al.,
175 2013; Kiehl, 2007; Knutti & Hegerl, 2008). Such model uncertainty can cause a large range of
176 ΔT_{2100} found by different GCMs even if they use the same prescribed evolution of GHGs. Policy
177 decisions geared towards meeting the Paris Climate Agreement must be made considering
178 scenario and model uncertainty.

179 Several other approaches have been developed to forecast ΔT . Some approaches use
180 similar regression analyses of historical records of ΔT (Chylek et al., 2016; Folland et al., 2018;
181 Lean & Rind, 2009; Suckling et al., 2017). Other simple models use a small number of boxes to
182 represent the atmosphere, ocean, and/or global carbon cycle (Meinshausen et al., 2009;
183 Schwartz, 2012). Projections of future ΔT have also been constructed from simple calculations
184 using emissions or mixing ratios of carbon dioxide that are from prescribed scenarios such as the
185 RCPs or are based on forecasts of population, economic growth, and other factors (Raftery et al.,
186 2017; Zeng & Geil, 2016).

187 Many of these studies reach conclusions concerning future global warming generally in
188 agreement with the CMIP5 GCMs. Often this consensus is due to their models or analyses being
189 driven by CMIP5 inputs and/or results. Fawcett et al. (2015) used a reduced complexity climate
190 model constrained by the climate sensitivities from CMIP5 GCMs to conclude GHG emissions
191 reductions based on the Paris Climate Agreement fall well short of the reductions needed to limit
192 global warming to 2 °C, and suggest emissions scenarios similar to that associated with RCP 2.6
193 are needed. Similarly, Raftery et al. (2017) examined projections of population, global economic
194 output, and the carbon intensity of the world's economies to conclude that median warming in
195 2100 would be 3.2 °C (likely range 2 °C to 4.9 °C) with only a 5% chance of remaining beneath
196 2 °C. Raftery et al. (2017) relied on the relationship between carbon emissions and global
197 warming from the CMIP5 GCMs.

198 In slight contrast, Chylek et al. (2016) used a standalone regression model to project a
199 rise in future ΔT of slightly less than 2 °C by end-of-century for RCP 4.5. This warming is
200 somewhat less than the projected 2.5 °C multi-model mean of 42 CMIP5 GCMs. Another
201 empirical analysis of ΔT using an energy balance model (Mauritsen & Pincus, 2017) examines

202 the relationship between transient, equilibrium, and committed warming for scenarios that either
203 omit or include the uptake of CO₂ by the world's oceans. They determined that there is a 50%
204 chance of global warming remaining below 1.5 °C if additional future radiative forcing of
205 climate (RF) does not exceed 1.2 W m⁻². This limit would be realized in year 2053 if the current
206 rate of RF increase (+0.033 W m⁻² yr⁻¹) was kept constant. We reach a broadly similar
207 conclusion based on our modeling effort with the EM-GC.
208



209
210
211 **Figure 2.** Observed and GCM-simulated global warming, 1970-2060. The observed ΔT time
212 series are taken from four data centers (CRU4, GISS, NCEI, and a fourth option from the
213 Berkeley Earth group notated as BEG) and are shown in black, with grey error bars representing
214 the uncertainty from the CRU4 record every ten years. The modeled ΔT time series are taken
215 from the output of 41 GCMs that participated in CMIP5 over the RCP historical and RCP 4.5
216 future experiment time periods and are shown individually in light blue. The maximum, mean,
217 and minimum from the GCM ensemble are shown in dark blue. The green trapezoid represents
218 the indicative likely range for annual average ΔT for the years 2016 to 2035, and the green bar
219 represents the likely range for the mean value of ΔT for this two-decade time period, both given
220 in Chapter 11 of AR5.

221
222

223 Chapter 11 of AR5 (Kirtman et al., 2013) showed that the CMIP5 GCMs tend to
224 overestimate ΔT for the early part of the 21st century, as shown in **Figure 2**. This figure
225 compares time series of ΔT from 41 CMIP5 GCMs (light blue) with the observed temperature
226 record from the four data centers shown in figure 11.25 of AR5. Due to the tendency for
227 observed ΔT to be overestimated by the climate models, the authors of Chapter 11 of AR5
228 prepared an expert judgement of the expected rise in ΔT over the next few decades (green
229 trapezoid in Figure 2). Notably, these likely ranges of global warming lie below the GCM
230 ensemble mean. This expert judgement of global warming covers a time period for which all four
231 RCPs have similar values of RF. As will be shown in section §3, global warming forecasts by the
232 EM-GC are in close quantitative agreement with this green trapezoid.

233 Crafting environmental policy based on such a wide range of possible futures is difficult,
234 even if the physical link between rising GHGs and increasing temperature is well established.
235 The Transient Climate Response to cumulative carbon Emissions (TCRE) is a metric that was
236 developed to link global warming to future anthropogenic emissions of CO₂ (Gregory et al.,
237 2009). As such, TCRE provides a means for policy makers to exert direct control of global
238 warming through regulation of CO₂ emissions. Chapter 12 of AR5 (Collins et al., 2013) defines
239 TCRE as the modeled transient increase in ΔT per 1000 GtC of CO₂ released to the atmosphere.
240 Most climate models show that future ΔT increases in a nearly linear fashion with respect to
241 cumulative emissions of CO₂, but this relationship is dependent on the physics and structure of
242 the climate model, as well as assumptions regarding emissions of other GHGs and the time rate
243 of change of emitted CO₂ (Figure 12.45 of AR5). For example, model experiments that have CO₂
244 concentrations increasing at the rapid rate of 1% per year find a relatively low value for TCRE
245 compared to simulations with a slower rate of CO₂ increase (e.g. Figure SPM.10 (IPCC, 2013))
246 because the inertia of the climate system limits the transient temperature response relative to
247 faster emissions. It is commonly accepted that the transient response of ΔT to rising GHGs is less
248 than the equilibrium response because certain aspects of the climate system such as the
249 cryosphere and the transfer of heat into the ocean occur on multi-year timescales. Chapter 12 of
250 AR5 (Collins et al., 2013) states that TCRE likely lies between 0.8°C to 2.5°C per 1000 GtC.
251 The CMIP5 GCMs tend to lie toward the high end of this range for TCRE, whereas projections
252 of global warming found using our approach (section §3) lie toward the lower end.

253

254 1.3 Overview of this work

255 The Empirical Model of Global Climate (EM-GC) used in this study builds upon the
256 framework first described by Canty et al. (2013). This work also builds on Hope et al. (2017),
257 who used an earlier version of the model to conduct similar analysis. The EM-GC uses MLR
258 combined with a two-module ocean-atmosphere approach to simulate observed monthly
259 variations in ΔT . The MLR component uses an equation that represents numerous anthropogenic
260 and natural factors that drive variations in global climate. The version of the EM-GC used here
261 considers several factors not present in most other MLR-based analyses, and includes several
262 important updates since Hope et al. (2017), especially in the ocean module, as described in
263 section 2.

264 Section 3 presents results from the EM-GC concerning AAWR and projection of ΔT out
265 to year 2100. Differences in these quantities between the EM-GC and other works are also
266 described in section 3, as are analyses of these differences and how the EM-GC works. We
267 present our conclusions and how the EM-GC results fit into the climate modeling community's
268 knowledge of the climate system in section 4.

269

270 **2. Model construction**

271 The EM-GC provides a mathematical representation of the factors that govern the global
272 mean surface temperature anomaly (ΔT). We compute numerical values of climate amplification
273 (γ) and the efficiency of heat transfer from the atmosphere to the ocean (κ) based on the observed
274 climate record. We then use these values of γ and κ to project future ΔT . While MLRs have been
275 used to conduct similar calculations by other groups, our EM-GC includes several components
276 not included in these other models. These differences include the long-term export of heat from
277 the atmosphere to the ocean, a comprehensive treatment of tropospheric aerosols, and the
278 influence on global climate from variations in the strength of Atlantic Multidecadal Variability
279 (AMV, which we use as a proxy for AMOC), and a new probability weighting method for the
280 large ensemble of ΔT projections that incorporates the expert judgement of aerosol RF given in
281 Chapter 8 of AR5 (Myhre et al., 2013).

282 The EM-GC is an ensemble-based model whose parameter space spans a large range of
283 possible values for both the strength of the climate feedback and the historical strength of
284 anthropogenic aerosol forcing. The overall ensemble is filtered based on a set of model

285 parameters that quantify a statistically acceptable fit ($\chi^2 \leq 2$, described below) between observed
 286 and modeled historical ΔT and ocean heat content (OHC). These simulations of historical ΔT
 287 and OHC are then used to create a corresponding ensemble forecasts of ΔT , which allows for a
 288 detailed statistical analysis of the impact of uncertainty in aerosol RF and climate feedback on
 289 future global warming.

290 In the four following sections, we describe the model equations and input data,
 291 representation of the ocean component, climate sensitivity and feedbacks, and the different
 292 modes of the EM-GC.

293

294 2.1 EM-GC core equations

295 The EM-GC simulation of observed ΔT uses a MLR-based analysis of the flow of energy
 296 between major components of Earth's climate system. The main equations of the EM-GC are:

297

$$\begin{aligned} \Delta T_{MDL i} = & \frac{1 + \gamma}{\lambda_p} \{GHG RF_i + AER RF_i + LUC RF_i - 0.671 Q_{OCEAN i}\} + C_0 + C_1 \\ & \times SAOD_{i-6} + C_2 \times TSI_{i-1} + C_3 \times ENSO_{i-2} + C_4 \times AMV_i + C_5 \\ & \times PDO_i + C_6 \times IOD_i \end{aligned} \quad 1a)$$

298

$$Cost Function = \sum_{i=1}^{N_{MONTHS}} \frac{(\Delta T_{MDL i} - \Delta T_{OBS i})^2}{\sigma_{OBS i}^2} \quad 1b)$$

299

$$\chi^2 = \frac{1}{(N_{YRS} - N_{DOF} - 1)} \sum_{j=1}^{N_{YRS}} \frac{(\langle \Delta T_{MDL} \rangle_j - \langle \Delta T_{OBS} \rangle_j)^2}{\langle \sigma_{OBS} \rangle_j^2} \quad (1c)$$

300 where $\lambda_p = 3.2 \text{ W m}^{-2} \text{ }^\circ\text{C}^{-1}$ (Planck response), γ is the dimensionless climate amplification term,
 301 C_0 to C_6 are regression coefficients, and i is an index for month. This model representation of
 302 $\Delta T_{MDL i}$ considers four anthropogenic factors (GHGs, net anthropogenic tropospheric aerosols
 303 [AER], land use change [LUC], and ocean heat export [Q_{OCEAN}]) as well as six natural factors
 304 (SAOD, TSI, ENSO, AMV, PDO, and IOD). The data inputs for all factors aside from Q_{OCEAN}
 305 are either taken directly or modified slightly from outside sources, while Q_{OCEAN} is calculated
 306 within the EM-GC. (Section §2.2 below defines Q_{OCEAN} and its governing equations; the

307 multiplication of Q_{OCEAN} by 0.671 in Equation 1a represents an area correction between Q_{OCEAN}
308 as computed in the ocean module and its effect on the atmosphere.) The sources for all of our
309 input data and the small changes we apply to them are fully documented in sections §2.1.1 and
310 §2.1.2 below.

311 Each member of an EM-GC ensemble uses the same natural factors, ΔT_{OBS} record, OHC
312 record, GHG forcing time series, and LUC forcing time series. The ensemble members vary as
313 each is constrained to different assumed values for AER radiative forcing and γ . The
314 anthropogenic components for each run are fed into the OHC submodule of the EM-GC to
315 calculate Q_{OCEAN} . The submodule produces estimates for global average sea surface temperatures
316 (SSTs) and the human component of ΔT_{MDL} . These two temperature time series are used to
317 recalculate Q_{OCEAN} , and the submodule iterates this process until those three quantities (i.e. SSTs,
318 $T_{\text{MDL-HUMAN}}$, and Q_{OCEAN}) remains stable between iterations.

319 We then solve for the seven regression coefficients (C_i) by minimizing the cost function
320 (Equation 1b), accounting for the 1σ uncertainty in each value of monthly global mean observed
321 temperature ($\Delta T_{\text{OBS } i}$). The temperature records used to prescribe $\Delta T_{\text{OBS } i}$ are based on one of the
322 previously mentioned CRU4, GISS, and NCEI data sets, as well as a fourth option from the
323 Berkeley Earth group (BEG) (Rohde et al., 2013). The terms in the cost function are indexed
324 over the total number of months (N_{MONTHS}) for which $\Delta T_{\text{OBS } i}$ are available, either 2040 months
325 (Jan.1850 to Dec.2019) for CRU4 and BEG or 1680 months (Jan.1880 to Dec.2019) for GISS
326 and NCEI.

327 Our modeling approach also makes use of reduced chi-squared (χ^2) that defines the
328 goodness-of-fit between observed and modeled ΔT (Equation 1c). In equation 1c, N_{YRS} represents
329 the total number of years for which $\Delta T_{\text{OBS } i}$ are available (170 years for CRU4 and BEG; 140
330 years for GISS and NCEI) and $\langle \rangle$ denotes annual average. Unless otherwise stated, the number
331 of degrees of freedom (N_{DOF}) in this study is nine: the climate amplification term, an ocean heat
332 surface diffusivity parameter, and the seven regression coefficients. The EM-GC can run with
333 any selection of our natural and anthropogenic variables included or excluded, potentially
334 reducing N_{DOF} . The equation for χ^2 is based on annual averages of observed and modeled ΔT
335 because the autocorrelations of ΔT_{OBS} and ΔT_{MDL} exhibit similar shapes when examined as
336 annual averages, but do not match on the monthly time grid (Canty et al., 2013). Therefore, the
337 use of annual averages reduces the effect of high-frequency variations of ΔT_{OBS} that are not

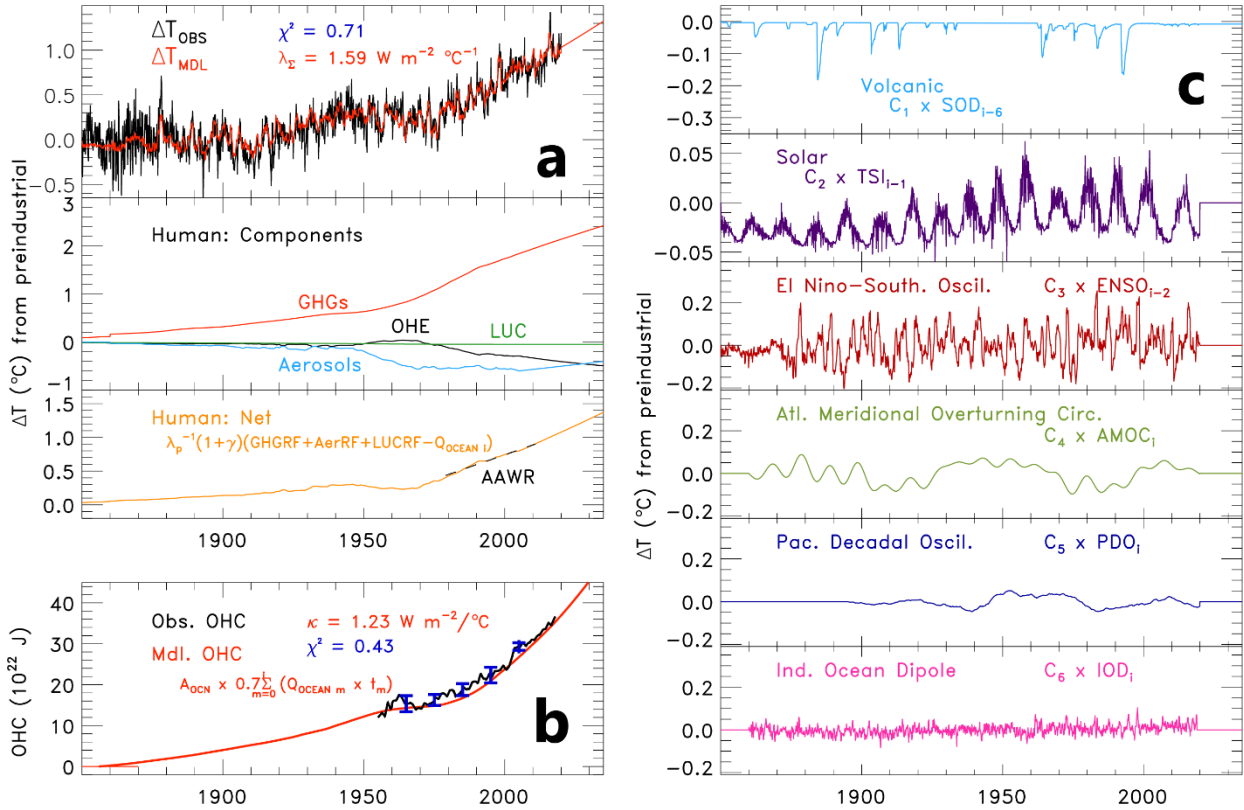
338 captured by the model. Nonetheless, the model framework is expressed in terms of monthly time
339 series for all quantities to properly quantify the effect of factors such as major volcanic eruptions
340 and ENSO on global climate.

341 We compute two other versions of χ^2 as well. While equation 1c as described above is
342 defined for ΔT over the full time period of available observations, we additionally compute
343 reduced chi-squared using the same framework both for OHC over the full time period of OHC
344 and for ΔT over the most recent 80 years. As the EM-GC is designed to fit both atmospheric and
345 oceanic observations, we do not consider simulations with acceptable fits to ΔT_{OBS} if they do not
346 also provide an acceptable fit between OHC_{MDL} and OHC_{OBS} . We then consider χ^2 for ΔT over
347 the past 80 years because a combination of factors makes it possible to achieve an acceptable fit
348 (i.e., $\chi^2 \leq 2$) for the full time series of ΔT_{OBS} while significantly over- or under-estimating
349 warming during the last 30 to 50 years. Since the most recent several decades are a focus of our
350 study, a lack of fit of ΔT_{OBS} over this period would confound meaningful analysis. We choose a
351 length of 80 years to assure that all semi-oscillatory natural forcing factors experience at least
352 one full cycle within the years of consideration (PDO and AMV vary on time scales of up to 60
353 or 70 years).

354 **Figure 3** provides a visual representation of our model (i.e. Equations 1a-c) by showing a
355 single run from an EM-GC ensemble with the best fits to ΔT_{OBS} when using a time series for
356 aerosol radiative forcing (AER RF) that matches the IPCC most-likely value of AER RF in 2011.
357 We refer to this depiction of the EM-GC's components as a "ladder plot". The top rung of Figure
358 3a shows model input ($\Delta T_{\text{OBS } i}$, black) and output ($\Delta T_{\text{MDL } i}$, red). The second and third rungs of
359 Figure 3a show the anthropogenic components of ΔT_{MDL} , both separated (second rung) and
360 combined (third rung). GHG RF in this run is based on the RCP 4.5 time series for CO_2 , CH_4 ,
361 N_2O , and other GHGs (Meinshausen et al., 2011; Thomson et al., 2011). Nearly identical results
362 are found upon use of RCP 8.5 or RCP 2.6, because the RCP scenarios use the same historical
363 data for all species until 2005 (Figure 1). The time series for AER RF used in Figure 3a is based
364 upon our analysis of direct RF due to six aerosol types provided by RCP (Lamarque et al., 2011),
365 combined and expanded to include the indirect aerosol effect as well, as described in section
366 §2.1.2. LUC RF is taken from Table AII.1.2 of AR5. Our Q_{OCEAN} , the export of heat from the
367 atmosphere to the ocean, is found by simulating the long-term observed rise in OHC, as

368 described in section §2.2. The net human time series in the third rung (gold line) serves as the
 369 basis for calculating AAWR and is further discussed in section §2.3.

370



371

372 **Figure 3.** Observed and modeled ΔT , 1850 to 2019, relative to a preindustrial baseline (1850 to
 373 1900). Ladder plots showing observed ΔT from CRU4 (top rung of Figure 3a, black line), the
 374 EM-GC simulation of ΔT from CRU4 (top rung, red line), ΔT_{HUMAN} (third rung of Figure 3a,
 375 gold line) and its components (second rung of 3a), AAWR (third rung of 3a, dashed black line),
 376 and contributions to ΔT from various natural factors (TSI, second rung of 3c, purple line; SAOD,
 377 first rung of 3c, light blue line; ENSO as measured by the Multivariate ENSO Index version 2,
 378 third rung of 3c, crimson line; AMV with 9-year Fourier filtering as our AMOC proxy, fourth
 379 rung on 3c, green line; PDO with 10-year smoothing, fifth rung of 3c, indigo line; IOD, sixth
 380 rung of 3c, pink line). Figure 3b shows the model-simulated rise in OHC (red line) from the top
 381 700 m compared to the average of five OHC data sets (black line; blue error bars show the 1σ
 382 standard deviation of these data about mean OHC).

383

384

385 The lower-left rung of the ladder plot (Figure 3b) depicts the modeled increase in OHC
 386 (red curve, proportional to the summation of Q_{OCEAN} via equation 2) and the observed rise in
 387 OHC (black line). In Figure 3b, the observed OHC is based upon the average of five data sets
 388 (Balmaseda et al., 2013; Carton et al., 2018; Cheng et al., 2016; Ishii et al., 2017; Levitus et al.,
 389 2012) such that the average is taken for each year when at least three of the five data sets provide
 390 an annual value (see **Figure S1**). The modeled increase in OHC is related to Q_{OCEAN} as follows:

$$OHC_{MDL\ i} = A_{OCEAN} \times 0.7 \sum_{m=0}^i [Q_{OCEAN\ m} \times t_m] \quad (2)$$

391 In equation 2, A_{OCEAN} is 3.3×10^{14} m² (Domingues et al., 2008), and t_m is the time length
 392 for month m in seconds, with $m=0$ representing the first month of a model run (e.g. January 1850
 393 for runs using CRU4). The factor of 0.7 is used to account for the fact that the OHC data sets we
 394 use represent only the top 700 m of the oceans, which hold roughly 70% of the total heat content
 395 of the ocean (Sect. 5.2.2.1 of Solomon (2007)). We verified this value of roughly 70% by
 396 comparing the OHC time series for the upper 700 m to the time series for the upper 2000 m or
 397 full ocean for the three data sources that provided time series for multiple depths (Balmaseda et
 398 al., 2013; Carton et al., 2018; Levitus et al., 2012).

399 The influences on ΔT of solar irradiance, volcanoes, ENSO, AMOC, PDO, and IOD are
 400 shown on the six rungs on Figure 3c. The sum of the variations in ΔT due to the six natural
 401 factors (Figure 3c) and the four anthropogenic factors (third rung of Figure 3a) plus the
 402 regression constant (C_0) equal ΔT_{MDL} . The overall agreement between the black and red lines in
 403 Figure 3a demonstrates the ability of the EM-GC to capture much of the variability and rise in
 404 global mean surface temperature over the past century and a half.

405

406 2.1.1 Model input, natural factors

407 In this section, we describe the data used to define model inputs for stratospheric optical
 408 depth (SAOD), total solar irradiance (TSI), the El Niño-Southern Oscillation (ENSO), the
 409 Atlantic Multidecadal Variability (AMV), Pacific Decadal Oscillation (PDO), and the Indian
 410 Ocean Dipole (IOD). Table A1 provides URLs of the websites that host these data records.

411 The time series for SAOD is a combination of two data sources. The first source is the
 412 recommended input for Phase 6 of the Climate Model Intercomparison Project (CMIP6). This
 413 CMIP6 SAOD time series is a combination of the Volcanic Model Intercomparison Project

414 (Zanchettin et al., 2016) for enhanced values of SAOD before the satellite era, Arfeuille et al.
415 (2014) for background values before the satellite era, and the GloSSAC data set (Thomason et
416 al., 2016) for all values during the satellite era. GloSSAC has since been extended past the last
417 year of CMIP6 (Thomason et al., 2018). We then use the Cloud-Aerosol Lidar and Infrared
418 Pathfinder Satellite Observations (CALIPSO) data (Vaughan et al., 2004) for year 2019 as our
419 second source since the GloSSAC record available at time of paper submission ends in Dec
420 2018. The GloSSAC and CALIPSO data are available as SAOD values by latitude; we create
421 SAOD values by latitude for years before 1979 by taking extinction coefficients and integrating
422 them from the tropopause to the top of the atmosphere. We then weight each latitude band by
423 area to reach a near-global SAOD time series (80°S to 80°N). The three data sets, as presently
424 available, match very closely during their respective time periods of overlap, though we do apply
425 a small adjustment to bring CALIPSO in line with GloSSAC. We treat SAOD after 2019 in the
426 same way that we treat all of our natural factors from 2020 onward: we flatline the data at a
427 value near zero representative of the current, non-volcanic background. As SAOD has a small
428 background value, it is the only natural time series in the EM-GC that uses a nonzero value into
429 the future (specifically, the December 2019 value of SAOD from CALIPSO). The final SAOD
430 time series is then lagged by six months in equation 1a to match the delay between surface
431 forcing and the thermodynamic response to major volcanic eruptions found by Thompson et al.
432 (2009) which is the same time lag that has been used in other MLR studies (Foster & Rahmstorf,
433 2011; Lean & Rind, 2008).

434 The time series of TSI used in the EM-GC is constructed from two data sets. TSI data up
435 to 2014 are an average of two solar models, one empirical and one semi-empirical (Matthes et
436 al., 2017); TSI data after 2014 are from satellite-based solar radiance measurements (Dudok de
437 Wit et al., 2017). These two data sets agree well at the point of merging. The EM-GC can
438 propagate the underlying 11-year solar cycle past 2019, but in this analysis we flatline TSI in the
439 future. We make this choice so that future projections of ΔT are based solely on anthropogenic
440 forcing. A one-month lag for TSI is used in equation 1a, because this lag yields the largest value
441 of C_2 . Lagging TSI is a common approach for quantifying the slight temporal offset of ΔT in
442 response to variations in total solar output (Lean & Rind, 2008).

443 The proxy for variations in the strength of the El Niño-Southern Oscillation used here is
444 built around the Multivariate ENSO Index version 2 (MEIv2) (Wolter & Timlin, 1993; Zhang et

445 al., 2019). The MEI time series, regularly updated, consists of a principle component analysis of
446 five physical quantities (sea level pressure, sea surface temperature, surface zonal winds, surface
447 meridional winds, and outgoing longwave radiation) that represent the state of the tropical ocean-
448 atmosphere system. The MEIv2 record begins in 1979. To provide data back to 1870, we
449 prepend the MEI-extended record (Wolter & Timlin, 2011), which uses a weighted combination
450 of two components (SSTs and the Southern Oscillation time series); the MEI-extended was
451 created as an extension of the original MEI record (Wolter & Timlin, 1993) that uses six physical
452 quantities instead of five. To extend the MEI-based data record from 1869 back to 1850, we
453 manually compute the SST average over the ocean surface area considered in the MEI records.
454 To prevent data shock, we increase the MEIv2 values by a constant offset so that its average
455 from 1979 to 2005 matches the average of the MEI-extended over the same time period (which is
456 the extent of their overlap). A two-month lag has been applied to the ENSO index in equation 1a,
457 because this lag provides the highest correlation with the simulated response of ΔT to ENSO
458 found using a thermodynamic approach (Thompson et al., 2009). The process used to determine
459 this lag from ENSO is described in Canty et al. (2013); this two-month lag is the same as used in
460 other MLR studies (e.g. Lean & Rind (2008) and FR11). The EM-GC is capable of using five
461 other ENSO data sets: the original MEI-based record (i.e. not MEIv2-based) as used in previous
462 iterations of the EM-GC (Canty et al., 2013; Hope et al., 2017), the Tropical Pacific Index
463 (Zhang et al., 1997), the Niño 3.4 index (Trenberth, 1997), the Cold Tongue Index (Deser &
464 Wallace, 1990), and the thermodynamic index of Thompson et al. (2009). Our scientific
465 conclusions are entirely insensitive to which ENSO index is used. Here we choose to focus on
466 the MEIv2 as its multiple-component construction leads to a robust time series with less noise
467 than other ENSO time series, particularly those that are based only on SST averages.

468 Our AMV index is based on the area weighted, monthly mean SST in the Atlantic Ocean,
469 between the equator and 60°N (Schlesinger & Ramankutty, 1994). We detrend the AMV index
470 using the RF anomaly due to human activity over the century-and-a-half time period of analysis,
471 as described in section §3.2.3 of Canty et al. (2013). This detrending process removes the
472 influence of long-term global warming on the AMV time series; without this external influence,
473 the detrended index can serve as a proxy for variations in the strength of the Atlantic Meridional
474 Overturning Circulation (AMOC) (Knight et al., 2005; Medhaug & Furevik, 2011; Stouffer et
475 al., 2006). Since AMOC is slowly varying, if it affects the climate with AMV as a proxy, then

476 high-frequency components of the AMV would be indicative of influence from non-AMOC
477 factors (such as ENSO) or noise. As such, our AMV index is also Fourier-filtered to remove all
478 components with temporal variations shorter than nine years, as described in Canty et al. (2013).
479 The resulting index represents anomalies in the north Atlantic SST that vary on time scales of a
480 decade or longer and are decoupled from human influence.

481 For the Atlantic signal, we have also tested the LOWESS filtering of ZT13, the “Atlantic
482 Water Variability index” of Pausata et al. (2015), and the “Atlantic gyre index” of Rahmstorf et
483 al. (2015), and two other levels of Fourier filtering of the AMV. Our main results concerning
484 AAWR are insensitive to the proxy used for AMOC, though the water variability index and gyre
485 index both have little to no expression in the climate record (i.e. the EM-GC returns near-zero
486 values for regression coefficient C_4). As such, we favor using the AMV with nine-year filtering
487 and anthropogenic detrending as the AMOC proxy in our regressions. Including AMV produces
488 relatively low values for χ^2 , allowing our ensembles to include more members without biasing
489 either AAWR or γ (which determines the trend of future temperatures). We have not yet tested
490 the North Atlantic Variability Index (NAVI), an alternative to AMV (Haustein et al., 2019).
491 However, near-zero values for C_4 are found for several other proxies for AMOC and the
492 resulting values of AAWR and ΔT_{2100} are similar to those shown when AMV is used in the
493 regression. We expect the NAVI (Haustein et al., 2019) to be inconsequential for our general
494 scientific conclusions (section §3.1) because values of AAWR and ΔT_{2100} found in our model
495 framework are insensitive to various other proposed proxies for AMOC, as well as the omission
496 of a proxy for AMOC from our regression.

497 Directly measuring the AMOC, namely its overall rate and volume of flow, is inherently
498 difficult and has not been done over a long enough time period to be used in the EM-GC.
499 However, observations of AMOC have been made in recent years. An analysis of a 14 year
500 (April 2004 to September 2018) time series of data from the RAPID-AMOC program (Duchez et
501 al., 2014) reveals a decline in the strength of AMOC over this time period (Smeed et al., 2017;
502 Srokosz & Bryden, 2015), similar to that shown by the AMV over these same years (Figure 3c).

503 The PDO represents the temporal evolution of temperature and sea level pressure of the
504 Pacific Ocean poleward of 20°N (Zhang et al., 1997). The PDO index, which begins in 1900 and
505 extends to present, represents the response of circulation in the Pacific Ocean to atmospheric
506 forcing (Saravanan & McWilliams, 1998; Wu & Liu, 2003). This index is regularly updated by

507 the University of Washington. The EM-GC also has the capability to use the Interdecadal Pacific
508 Oscillation (IPO) index to represent the influence of the Pacific Ocean on global climate, rather
509 than the PDO. For comparison to our decadal-filtered Atlantic signal, we use a 10-year running
510 mean of PDO (or IPO) in our analysis, a method reflected in other studies that attempt to link the
511 Pacific signal to global temperature patterns (England et al., 2014). In this paper, we use the 10-
512 year average of the PDO; using the IPO or using different smoothing times does not change our
513 results. We have also attempted to take the integral of the PDO to address the idea that the sign
514 of PDO affects the trend of ΔT , but taking the integral of PDO produces a time series with an
515 uncharacteristically large peak in the middle of the time series and few other features relating to
516 ΔT_{OBS} , leading to very small values for C_5 . As detailed in Canty et al. (2013), variations in ΔT
517 are more strongly influenced by the Atlantic Ocean than the Pacific, regardless of the treatment
518 of PDO. That said, the Pacific signal is stronger than the Atlantic signal in some select ensemble
519 members with strong aerosol forcing or with Atlantic proxies that exhibit inherently weak fits to
520 the ΔT_{OBS} record.

521 A proxy for variations in the circulation of the Indian Ocean is also used, so that all three
522 major ocean basins are represented. We use the Indian Ocean Dipole (IOD) index as defined Saji
523 et al. (1999), which represents the temperature gradient between the Western and Southeastern
524 portions of the equatorial Indian Ocean. The IOD time series we use is made with SSTs from the
525 Centennial in situ Observation-Based Estimate record (Ishii et al., 2005). We find that influence
526 of the Indian Ocean on ΔT is small, likely due to the size of this ocean basin relative to those of
527 the Atlantic and Pacific.

528

529 2.1.2 Model inputs, anthropogenic factors

530 The anthropogenic inputs included in the EM-GC are greenhouse gases, tropospheric
531 aerosols, land use change, and the long-term export of heat into the ocean in response to
532 anthropogenic atmospheric warming. All data mentioned below can be found online, with source
533 websites and other comments listed in Table A2.

534 Atmospheric abundances of the main drivers of the anthropogenic RF of climate – the
535 well-mixed greenhouse gases CO_2 , CH_4 , and N_2O – are taken directly from the RCP scenarios
536 (Meinshausen et al., 2011). For these and other GHGs referenced to Meinshausen et al. (2011),
537 we specifically use data from files provided by the Potsdam Institute for Climate Research

538 (PICR, URL in Table A2). Annual mixing ratios for each gas are converted to radiative forcing,
539 using the equations from Myhre (1998) and initial values from table AII.1.1a in AR5. The RF
540 values are interpolated onto the EM-GC's monthly time grid, with annual RF treated as midyear
541 conditions. The projected mixing ratio of CH₄ in year 2100 is dramatically higher in RCP 8.5
542 (3.48 ppm) compared to RCP 4.5 (1.54 ppm) (Figure 1). To quantify the sensitivity of global
543 warming to CH₄, we have defined four new hybrid scenarios for CH₄ that are linear
544 combinations of RCP 4.5 and RCP 8.5 (**Figure S2**). The RF of CH₄ for the RCPs used here
545 differs slightly from values of RF for CH₄ archived at PICR, due to the update for the
546 preindustrial value for CH₄ given in table AII.1.1a of AR5.

547 Other greenhouse gases include tropospheric ozone (O₃), stratospheric-ozone-depleting
548 substances (CFCs, HCFCs, CCl₄, CH₃Cl, CH₃Br, etc.), and other F-gases (HFCs, PFCs, and
549 SF₆). Prior and future RF of climate due to tropospheric O₃ is taken directly from Meinshausen et
550 al. (2011) for each RCP scenario. The increase in RF of climate due to tropospheric O₃ between
551 1750 and 2011 is nearly equal to that of CH₄, albeit with much larger uncertainty. The various
552 RCPs project different future RFs due to tropospheric O₃, with RCP 8.5 being the largest. The
553 RF of climate due to ozone-depleting substances (ODS), HFCs, PFCs, and SF₆ are all also taken
554 directly from the RCPs, via PICR.

555 We consider numerous anthropogenic aerosol scenarios that represent a wide range of
556 total (direct and indirect) RF of climate due to the aerosols. This wide range is essential for
557 consideration because the historical effect of aerosols on climate is not well-known (Myhre et al.,
558 2013), whereas future AER RF is projected to decline due to air quality regulations (Smith &
559 Bond, 2014). The climate record can be well-simulated by an aerosol scenario for which the RF
560 of climate due to GHGs has been considerably offset by aerosol cooling: in this case, large
561 values for the sum of climate feedback mechanisms (section §2.3) are needed to match the
562 observed rise in ΔT . The climate record can be fit just as well by a scenario for which RF due to
563 GHGs has barely been offset by aerosol cooling, in which case small values for the sum of
564 climate feedback mechanisms are required to match ΔT . If we assume that the feedback inferred
565 from the prior climate record will persist into the future, the strong aerosol cooling case will lead
566 to much larger future warming than the weaker cooling case (Knutti & Hegerl, 2008). The need
567 to consider this relation between AER RF and feedback drives the wide range of scenarios for
568 AER RF described below. We will often refer to a given AER RF time series by the value in year

569 2011 (AER RF₂₀₁₁) in order to relate our results to estimates of AER RF₂₀₁₁ given in chapter 8 of
570 AR5 (Myhre et al., 2013).

571 We construct our AER RF scenarios based on forcing data from the RCP database. First,
572 the direct RF for six types of aerosols (sulfate, black carbon, nitrate, dust, organic carbon, and
573 biomass burning products) are obtained from PICR for each RCP scenario (Lamarque et al.,
574 2011). These direct RF estimates were tied to the state of knowledge that guided the fourth IPCC
575 assessment report (Solomon, 2007). As was done in Canty et al. (2013), we use direct RF as
576 given by PICR for five of the six aerosol species; for sulfate, Smith et al. (2011) is used instead
577 because the PICR sulfate data do not reflect sulfate emissions well. In our study, the direct RF
578 time series for each component has been scaled to match values of direct RF in 2011 given by
579 chapter 8 of AR5 (Myhre et al., 2013), as noted in the caption of **Figure S3**. This matching
580 process includes eliminating the effect of biomass burning on RF of climate, as AR5 chapter 8
581 estimated that the RF due to biomass burning in 2011 was zero. Physically, biomass burning can
582 conceivably provide no RF impact as a result of cancellation between the warming due to black
583 carbon and the cooling due to organic aerosols products (sections 7.5.2.2 and 8.3.4.2 of AR5).
584 Our scientific conclusions would be unaffected had we used the RCP AER RF time series
585 directly, as archived by PICR. Nonetheless, we scale to AR5 values of direct RF in 2011 so that
586 our study is consistent with the consensus of the scientific community at the time of paper
587 submission.

588 We perform a second scaling on the aerosol direct RF time series to mathematically
589 simulate the aerosol indirect effect, e.g. cloud-aerosol interactions, with the goal of reaching the
590 AR5 best estimate for total aerosol forcing of -0.9 W/m^2 in 2011. First we separate the direct RF
591 time series into a cooling group – sulfates, mineral dust, primary and secondary organic aerosols,
592 and nitrates – and a warming “group” of black carbon; as biomass burning products were zeroed
593 earlier, they do not factor into the remainder of this analysis. Second, we take the ratio of the
594 sulfate total RF to the sulfate direct RF based on Smith et al. (2011) and Stern (2006) as
595 described in Canty et al. (2013), a scaling of 2.432. We apply this ratio to the cooling group
596 overall as the scaling factor to change the direct RF time series of the cooling group to the
597 respective total RF time series. We term the value used to scale direct-to-total RF for the cooling
598 group as α_{COOL} . Next, we find the respective direct-to-total ratio for the heating group – α_{HEAT} , in
599 this case 2.188 – needed to make the total cooling RF times series and total heating RF time

600 series add together such that the value in 2011 is -0.9 W/m^2 , which is AR5’s best estimate of
601 effective AER RF₂₀₁₁.

602 To simulate the uncertainty in historical AER RF, we create other AER RF time series by
603 varying α_{COOL} and α_{HEAT} . In doing so, we can create a potentially infinite number of AER RF
604 times series of different shapes and strengths. For each ensemble run of the EM-GC, we
605 constrain our AER RF times series to those constructed using a finite length of a cross-section
606 through this α -space, which we term “roads”, shown visually in **Figure S4a**. The “middle road”
607 of aerosol scenarios is anchored by the α -space point obtained by attaining the best-estimate
608 AER RF₂₀₁₁ (-0.9 W/m^2) as described in the previous paragraph. The slope of the middle road is
609 found by determining four other statistical combinations of the six aerosol direct RF time series
610 that produce values of total AER RF₂₀₁₁ corresponding to the AR5 confidence intervals (-0.4
611 W/m^2 to -1.5 W/m^2 , likely range, and -0.1 W/m^2 to -1.9 W/m^2 , 5 to 95% confidence range). The
612 “low road” and “high road” are then anchored by points in α -space that also have an AER RF₂₀₁₁
613 value of -0.9 W/m^2 . **Figure S4b** then shows the fifteen resulting AER RF time series that
614 correspond to the intersections of the three roads and five forcing isopleths.

615 Variations in the composition of Earth’s surface due to deforestation and other human
616 activities can also exert a change in the radiative forcing of climate. The ΔRF effect of
617 anthropogenic land use change (LUC) is taken directly from table AII.1.2 of AR5, with the
618 annual values linearly interpolated to the EM-GC’s monthly time grid. We assume the annual
619 values are centered at midyear in the interpolation. The release of GHGs from land-use-change
620 activities such as deforestation or concrete laying are factored into the GHG term itself, as the
621 LUC term only represents surface reflectivity.

622 We consider the rise in OHC as an anthropogenic signal because increases in the RF of
623 climate due to human activity cause a rise in temperature of both the atmosphere and the oceans
624 (Raper et al. 2002; Hansen et al. 2011; Schwartz 2012). The focus of many OHC studies has
625 been the top 700 m or top 2 km of the world’s oceans, and our work considers data from five
626 such studies (Balmaseda et al., 2013; Carton et al., 2018; Cheng et al., 2016; Ishii et al., 2017;
627 Levitus et al., 2012); three of these five studies consider both depths. For proper comparison, the
628 five data sets are normalized to a common value of 0 in 1986 (the midpoint year for the range of
629 time where three or more of the five OHC records are provided) before being averaged together.
630 The magnitude of an input OHC data set at any given point in time is not important in our model

631 framework, because we rely upon change in OHC over time. In this study, we focus on EM-GC
 632 runs that use 700 m OHC data, in which case we multiply the OHC values by 1.429 (1/0.7)
 633 before the model computes κ , the ocean heat diffusivity term, so as to scale the OHC from the
 634 upper 700 m to a value that approximates OHC for the full ocean.

635

636 2.2 EM-GC ocean components

637 The formulation for Q_{OCEAN} is based on finding the value of κ that best fits observed
 638 OHC data. Raper, Gregory, & Stouffer (2002) define κ as the ratio between the atmosphere-to-
 639 ocean temperature difference and the heat lost to the ocean. We assume Q_{OCEAN} is
 640 anthropogenically driven and we define the monthly values of Q_{OCEAN} as:

$$\begin{aligned}
 Q_{OCEAN\ i} &= \kappa(\Delta T_{ATM,HUMAN\ i} - \Delta T_{OCN,HUMAN\ i}) \\
 &= \kappa \left(\left[\frac{1+\gamma}{\lambda_p} \{GHG\ RF_i + AER\ RF_i + LUC\ RF_i\} \right] - \Delta T_{OCN,HUMAN\ i} \right) \quad 3)
 \end{aligned}$$

641

$$\kappa = \frac{\Delta OHC \div A_{OCEAN}}{\int_{t_{START}}^{t_{END}} (\Delta T_{ATM,HUMAN} - \Delta T_{OCN,HUMAN})_{i-72} dt} \quad (4)$$

$$= \frac{OHE \times \Delta t}{\int_{t_{START}}^{t_{END}} \left(\left[\frac{1+\gamma}{\lambda_p} \{GHG\ RF_{i-72} + AER\ RF_{i-72} + LUC\ RF_{i-72}\} \right] - [f_o \sum_0^{i-72} Q_{OCEAN}] \right) dt}$$

642 The main improvement from Hope et al. (2017) is the inclusion of $\Delta T_{OCN,HUMAN}$, which
 643 represents the temperature response of the well-mixed upper 100 m of the ocean due to the total
 644 rise in OHC. In the previous version of the EM-GC, heat exited the atmosphere without any
 645 modulation from an ocean response (i.e. $T_{OCN,HUMAN\ i} = 0$ for all i) allowing the ocean to function
 646 as an infinite sink. By allowing the model ocean to warm in response to the increase in
 647 atmospheric temperature, the amount of heat lost to the ocean per month is reduced over time
 648 due to the smaller difference in temperatures between the ocean surface and overlying air,
 649 providing a more realistic description of the climate system than earlier versions of our model.
 650 The new interactive ocean module provides a reduction in Q_{OCEAN} over time compared to the
 651 earlier version of the model, resulting in a slight rise in total anthropogenic RF and in computed
 652 future global mean surface temperature relative to that found using a static ocean. This new

653 model formulation thus also introduces a mechanism for the climate system to continue warming
654 even after total anthropogenic RF plateaus, as it does in both RCP 4.5 and RCP 2.6.

655 The integral in the denominator and the delta time in the numerator of equation 4 are both
656 taken over the entire time extent of the OHC record being considered, i.e. t_{START} and t_{END} are the
657 first and last months corresponding to the years of the OHC record being used. Ocean Heat
658 Export (OHE) is an average over area and time of the export of heat from the atmosphere to the
659 ocean, obtained by estimating the total rise in OHC over time with a linear fit (Canty et al.,
660 2013). We apply a six-year (72 month) lag to account for the time needed for a given amount of
661 heat leaving the atmosphere to penetrate to depth (Schwartz, 2012). Other studies (Lean & Rind,
662 2008; Suckling et al., 2017) infer or apply a ten-year lag; key model outputs such as AAWR are
663 insensitive to choices for the time delay between atmospheric perturbation and mean oceanic
664 response (equation 4) for any timescales ranging from annual to multidecadal. The new
665 formulation for Q_{OCEAN} allows the model parameter κ to be directly compared to literature values
666 derived from GCMs (Raper et al., 2002).

667 The term f_o in the denominator of the last part of equation 4 represents a combination of
668 the heat capacity of ocean water, the fraction of ocean volume in the surface layer of interest, and
669 the fraction of total Q_{OCEAN} that warms the surface layer. To calculate f_o , decadal ocean warming
670 as a function of depth was extracted from a selection of CMIP5 models' output, smoothed, and
671 then normalized to the warming in the layer from 0-100 m. A simplified warming profile was
672 then selected for the remaining depth of the ocean down to 4 km, (green segments of **Figure S5**)
673 favoring the group of warming profiles from RCP 4.5 and RCP 8.5. This stratified warming
674 profile was used in combination with the ocean depth profile to determine the percentage of
675 ocean heat export that warmed the 0-100 m layer, producing $\Delta T_{\text{OCN,HUMAN}}$. This 100 m top layer
676 is used as the section of ocean that interacts directly with the atmosphere, because it is well-
677 mixed. We represent the ocean as being 1 km deep for 10% of the ocean area (representing the
678 continental shelves) and 4 km deep for the remaining 90%. This simplified depth profile
679 approximates the average depth of the real ocean to within 3%, 3.7 km compared to 3.682-3.814
680 km (Charette & Smith, 2010); using the ocean surface area estimate of $3.3 \times 10^8 \text{ km}^2$ from
681 (Domingues et al., 2008), our simplified ocean also approximates the total volume of the real
682 ocean to within 10%, $1.221 \times 10^9 \text{ km}^3$ compared to $1.33\text{-}1.37 \times 10^9 \text{ km}^3$. Taken together, this
683 CMIP5-based warming profile with depth implies that 13.7% of the rise in total OHC occurs in

684 the well mixed, upper 100 m of the ocean, resulting in the $\Delta T_{\text{OCN,HUMAN}}$ term in equations 3 and
685 4. As a result, the value of f_o in equation 4 is $8.76 \times 10^{-5} \text{ }^\circ\text{Cm}^2/\text{W}$.

686 Output from the ocean module, Q_{OCEAN} , is area corrected to scale the average forcing
687 applied to the atmosphere by the ocean before this quantity is used in the MLR. The ocean
688 module is based upon the total surface area of the world's oceans, but the inputs to the
689 atmospheric module are applied to the entire surface area of the Earth. As such, we scale Q_{OCEAN}
690 in the model atmosphere by the ratio of ocean surface area to Earth's total surface area, (i.e. the
691 multiplier 0.671 in equation 1a,) to ensure that the total amount of energy leaving the atmosphere
692 is the same as the total amount of energy entering the oceans.

693 Four alternate values for the fraction of OHC in the upper 100 m were also considered to
694 test the sensitivity of future atmospheric temperatures to the ocean's response to global warming.
695 At one extreme, warming due to the rise in OHC is distributed linearly in just the upper 1 km of
696 the ocean with no warming deeper, putting 18.2% of the rise in OHC into the top 100 m of the
697 global ocean. At the other extreme, a warming profile that assumes a constant warming rate
698 throughout the entire ocean has only 2.7% of the rise in OHC going into the upper 100 m. Both
699 scenarios are physically unrealistic but provide bounds for the range of how much $\Delta T_{\text{OCN,HUMAN}}$
700 can change for a given OHC record. All five warming profiles with depth and their associated
701 top 100 m fractions are summarized in **Table S1**. Choice of ocean warming profile does not
702 affect our results significantly, as the interplay between $\Delta T_{\text{OCN,HUMAN}}$ and κ means that Q_{OCEAN} is
703 largely driven by the choice of OHC_{OBS} .

704

705 2.3 Climate feedback and sensitivity

706 Climate feedback processes and overall climate sensitivity define how changes in RF,
707 particularly the rise in anthropogenic RF, drive ΔT . In the EM-GC, the sum of RF due to GHGs,
708 aerosols, LUC, and OHE is multiplied by $(1+\gamma)/\lambda_p$, where λ_p is the Planck response parameter
709 ($3.2 \text{ W m}^{-2} \text{ }^\circ\text{C}^{-1}$) and γ is the dimensionless climate amplification term, to determine ΔT
710 (equation 1a). If the net response of changes in humidity, lapse rate, clouds, and surface albedo
711 that occur in response to anthropogenic RF of climate is positive, as is the case for the vast
712 majority of simulations conducted for this study, then the numerical value of γ is positive. This
713 model framework is based on that described in Bony et al. (2006) and section 8.6 of the previous

714 IPCC report (Solomon, 2007). The EM-GC’s variable for the sum of climate feedback
 715 mechanisms, λ_Σ , has units of $\text{W m}^{-2} \text{ }^\circ\text{C}^{-1}$ and is related to γ and λ_p via:

$$1 + \gamma = \frac{1}{1 - \frac{\lambda_\Sigma}{\lambda_p}} = \frac{\lambda_p}{\lambda_p - \lambda_\Sigma} \quad 5)$$

716 This relation between γ and λ_Σ is commonly used in the climate modeling community
 717 (section 8.6 of Solomon (2007)). We can also relate λ_Σ to the traditional climate feedback
 718 parameter λ (Bony et al., 2006; Gregory, 2000; Schwartz et al., 2014; Sherwood et al., 2020) by
 719 reducing equation 1a to just the anthropogenic terms to produce the relations:

$$\Delta T_{Human\ i} = \frac{1 + \gamma}{\lambda_p} \{GHG\ RF_i + AER\ RF_i + LUC\ RF_i - Q_{OCEAN\ i}\} \quad 6a)$$

$$\Delta T_{Human} = \frac{1 + \gamma}{\lambda_p} \Delta F_{Human} \quad 6b)$$

$$\lambda^{-1} = \frac{1 + \gamma}{\lambda_p} \rightarrow \lambda = \lambda_p - \lambda_\Sigma \quad 6c)$$

720
 721 We choose to focus on λ_Σ instead of λ for the majority of this paper. This choice allows
 722 for an intuitive comparison between λ_Σ , γ , and ΔT – as one quantity rises, so do the others. This
 723 intuitive relationship highlights how uncertainty in various climate feedback mechanisms (i.e.
 724 aside from the blackbody response) can be the driving force in future ΔT uncertainty. We assume
 725 a constant value for λ_Σ (and λ) for each ensemble member in most of the results shown below, as
 726 this assumption provides a multitude of simulations of ΔT with χ^2 values less than 1, well below
 727 our acceptable fitting limit of 2. We view this as a reasonable approximation because section
 728 12.5.3 of AR5 and references therein suggest λ changes slowly over millennia; any changes in λ
 729 over a few centuries should be unnoticeable unless gradual changes force the climate system past
 730 a significant tipping point. For completeness, we also examine the effect on EM-GC ΔT of a
 731 slowly- or moderately-varying λ in section §3.4 of this paper (also see **Table S2** and **Figure S6**).

732
 733 **3. Results and Analysis**

734 Our results focus mainly on Attributable Anthropogenic Warming Rate (AAWR) and
 735 projections of the global mean surface temperature anomaly relative to preindustrial (ΔT). We
 736 first present here a summary of the probabilistic distribution of these two quantities for our best

737 representative ensemble of EM-GC simulations, and next describe how these distributions
738 compare to CMIP5 and other studies. Then, in each subsection to follow, we delve further into
739 our results for AAWR and ΔT_{2100} , providing a detailed description of their sensitivities as well as
740 comparisons to other published results. The first three subsections present discussion of AAWR,
741 in which we describe our approach, possible shortcomings in prior efforts used to evaluate
742 AAWR, and the uncertainties involved in proper quantification of AAWR. The last five
743 subsections present results for ΔT , including quantification of the sensitivity to uncertainty in
744 future emissions of CH_4 and relating our projections of future warming to cumulative,
745 anthropogenic emissions of CO_2 .

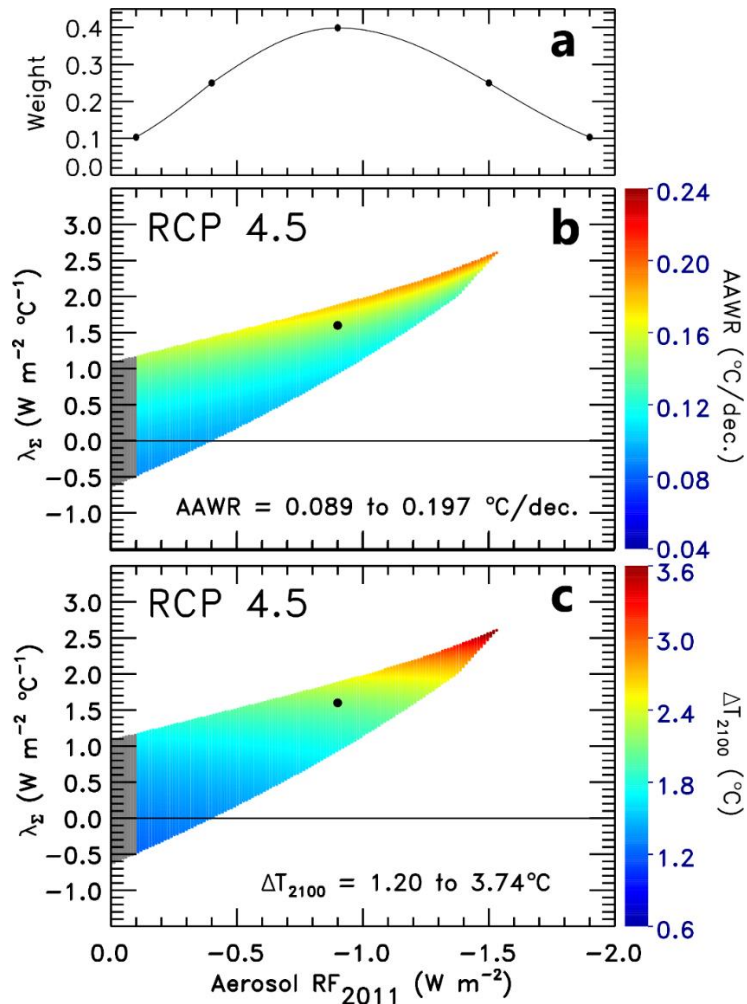
746 Overall, our numerical estimates of AAWR for 1979 to 2100 fall between prior estimates.
747 Our best estimate of AAWR is $\sim 0.14^\circ\text{C}/\text{decade}$, which is noticeably lower than the value for
748 AAWR from CMIP5 GCMs ($\sim 0.22^\circ\text{C}/\text{decade}$). Our value for AAWR falls between estimates of
749 AAWR from FR11 (0.170 ± 0.012) and the AMOC-based AAWR from ZT13 (0.070 ± 0.019).
750 Below, we describe the sensitivity of AAWR to various estimates of radiative forcing by
751 aerosols, the sum of climate feedback mechanisms, and multiple records for ΔT_{OBS} . Notably,
752 AAWR in our model is largely insensitive to whether AMOC is included (see §2.1.1 and **Figure**
753 **S7a and S7b**).

754 Our ensemble median value for global warming at the end of this century, ΔT_{2100} , is
755 consistently cooler than the CMIP5 ensemble median value for ΔT_{2100} . Indeed, our ensemble
756 median of ΔT_{2100} often lies close to the CMIP5 ensemble minimum warming. The EM-CG
757 framework, with its tendency for cooler results, assigns each RCP scenario a higher probability
758 of fulfilling the Paris Agreement warming limitations, compared to the CMIP5 GCMs. The near-
759 term warming found by our EM-GC also closely matches the expert assessment of CMIP5
760 results shown in chapter 11 of AR5, represented by the green trapezoid in Figure 2.

761 **Figure 4** shows AAWR and ΔT_{2100} for the same ensemble run of the EM-GC and depicts
762 the weighting function we use to create probabilistic summaries of our results. Each simulation
763 in this ensemble has the same set of inputs except for varying λ_{Σ} and varying the shape and
764 strength of anthropogenic aerosol forcing, pinned to the value of AER RF in 2011. Computed
765 values of AAWR are sensitive to AER RF and λ_{Σ} because of differences in the shape of the
766 aerosol term (blue line Figure 2a) that is subtracted from the GHG term (red line Fig 2a), for
767 various members of the ensemble. Values of ΔT_{2100} are particularly sensitive to climate

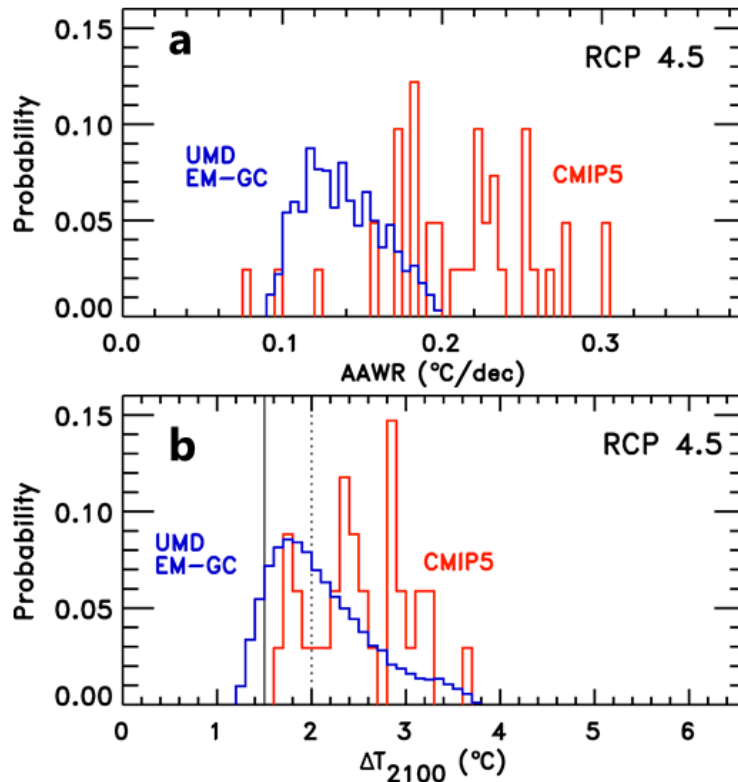
768 feedback, because by end of century the RF due to aerosols is expected to be considerably
769 smaller than contemporary values (Smith and Bond, 2014). The EM-GC ensemble shown in
770 Figure 4 is based on RCP 4.5 GHGs and constrained by the CRU4 record for ΔT_{OBS} from 1850
771 to 2019. The values of AAWR and ΔT_{2100} shown in Figure 4 are for those members of the
772 ensemble for which all three χ^2 filters yield a value less than or equal to 2: i.e., those sets of
773 model results able to provide a “good fit” to ΔT_{OBS} from 1850 to 2019, from 1940 to 2019, and
774 to OHC averaged among five data centers from 1955 to 2018. We also eliminate any simulations
775 for which AER RF_{2011} does not lie between -1.9 and -0.1 W m^{-2} , the 5% and 95% confidence
776 intervals for RF due to anthropogenic aerosols given in AR5, which is why model results shown
777 on the left side of Figure 4b and 4c are shown in grey. **Figure 5** then aggregates these results into
778 probability density functions (PDFs) of AAWR and ΔT_{2100} from the EM-GC (blue) using a
779 weighting method, described in section §3.1, that is based on the AR5 likelihoods for the values
780 of AER RF_{2011} (Figure 4a). Similar PDFs based on results from 41 CMIP5 GCMs (without any
781 weighting, red) are also shown in Figure 5.

782



783

784 **Figure 4.** AAWR and ΔT_{2100} as a function of AER RF₂₀₁₁ and λ_{Σ} over a single EM-GC ensemble
 785 (panels b and c) and the AER RF₂₀₁₁-based weighting function used to aggregate our ensemble
 786 statistics (panel a). Values of AAWR are for 1979 to 2010 and values of ΔT_{2100} are relative to the
 787 preindustrial baseline. We show all simulations for which $\chi^2 \leq 2$ for all three fitting comparisons,
 788 (i.e. fitting ΔT for the full time period, fitting ΔT for the most recent 80 years, and fitting OHC
 789 over its time period,) though any model results that for AER RF₂₀₁₁ outside of the range -0.1 to
 790 -1.9 W m^{-2} , the 5% and 95% confidence intervals given in AR5, are covered using the color
 791 grey. All runs in this ensemble use RCP 4.5 GHG RF and RCP 4.5-based AER RF scenarios
 792 along the middle road of Figure S4 to simulate the CRU4 ΔT_{OBS} record. The black dot in panels
 793 b and c represents the single run from the ensemble with the lowest χ^2 over the full ΔT record
 794 among simulations forced with the AER RF times series that gives -0.9 W/m^2 in 2011, the best
 795 estimate for AER RF₂₀₁₁ stated in AR5. Results from this single simulation, broken into
 796 component time series, are shown in Figure 3.



798

799 **Figure 5.** Probability density functions (PDFs) of the EM-GC computations of AAWR and
 800 ΔT_{2100} for RCP 4.5 shown in Figs. 4b and 4c, weighted by the associated value of AER RF_{2011}
 801 using the weighting function shown in Figure 4a (blue lines). PDFs of AAWR and ΔT_{2100} from
 802 CMIP5 GCMs, also for RCP 4.5, are also shown (red lines). The height for each bin (0.1°C
 803 width for ΔT_{2100} , $0.05^\circ\text{C}/\text{decade}$ width for AAWR) for the UMD EM-GC PDFs represents the
 804 probability of a run with that value being randomly selected from the respective model output
 805 shown by non-grey colors in Figure 4b and 4c, when each model run is weighted by the AER
 806 RF_{2011} -based weighting function shown in Figure 4a. Similar probabilities can be taken from the
 807 CMIP5 ensemble giving results from each GCM equal weighting (red). For panel b, the Paris
 808 Agreement goal of 1.5°C warming and upper limit of 2°C warming are shown by the vertical
 809 solid and dotted lines, respectively.

810

811 3.1 AAWR from the EM-GC

812 We base our estimate of AAWR on the slope of ΔT_{HUMAN} over the years 1979 to 2010.
 813 To calculate AAWR, our empirical model is first run over a chosen time period to produce the
 814 ΔT_{HUMAN} series; then a linear fit is calculated from this series over the years 1979 to 2010.

815 Except when otherwise stated, the chosen time period for the model run is the entire available ΔT
816 record, which for the CRU4 record used in Figure 3 is January 1850 to December 2019. To
817 choose which ensemble member from Figure 4 would be shown in Figure 3, we selected the run
818 with the best estimate of AER RF_{2011} from AR5 (-0.9 W/m^2) that had the lowest value of χ^2 for
819 fitting the full ΔT_{OBS} record. This selected run gives a value for AAWR of $0.146 \text{ }^\circ\text{C/decade}$.

820 To aggregate the EM-GC ensemble results from Figure 4b, we assign probabilities to
821 each ~ 150 long time series for the RF due to aerosols, tied to the value of AER RF_{2011} for each
822 time series. We create an approximate Gaussian distribution of AER RF_{2011} based upon AR5
823 estimates of this quantity (Figure 4a). This weighting function peaks at -0.9 W/m^2 (AR5 best
824 estimate of AER RF_{2011}) and the cumulative probability of AER RF_{2011} values between -0.4 and
825 -1.5 W/m^2 is set at 66.7%. Similarly, the cumulative probability of the weighting function
826 between -0.1 and -1.9 W/m^2 is 90%, which corresponds to the AR5 specification of -0.1 and $-$
827 1.9 W/m^2 being the 5% and 95% confidence intervals for this quantity (Myhre et al., 2013). We
828 then take all runs shown as non-grey colors for AAWR in Figure 4b (i.e. all runs for which a
829 good fit to ΔT for the full time period, ΔT for the most recent 80 years, and OHC from 1955 to
830 2018 can be obtained), bin by AER RF_{2011} , and find the probability distribution for AAWR
831 within each of these bins. The PDFs for AAWR within each bin are then aggregated using the
832 IPCC-based weightings (Figure 4a) for each value of AER RF_{2011} (Figure 4a) to create the final
833 PDF shown as a blue line in Figure 5a. We use this superposition of PDFs weighting method to
834 account for the fact that the EM-GC finds many more acceptable fits to the climate record (i.e. χ^2
835 ≤ 2) for combinations of λ_Σ and AER RF_{2011} associated with less-negative values of AER RF_{2011} ,
836 whereas AR5 suggests that -1.5 W/m^2 is as likely as -0.4 W/m^2 for the RF of climate in 2011
837 due to aerosols. This weighting method gives model runs with stronger aerosol cooling the same
838 weight as runs with weaker aerosol cooling. For the AAWR ensemble shown in Figure 4b, this
839 weighting process produces a median of $0.135 \text{ }^\circ\text{C/decade}$, with a full range of $0.089 \text{ }^\circ\text{C/decade}$
840 to $0.197 \text{ }^\circ\text{C/decade}$. Through most of the ensemble, the resulting time series for ΔT_{HUMAN} and the
841 resulting values of AAWR agree well with another recent estimate found using a similar
842 approach (Chylek et al., 2014).

843 Our estimate of AAWR is sensitive to which aerosol forcing time series is used,
844 especially in relation to λ_Σ , and is partially sensitive to ΔT_{OBS} , but insensitive to the inclusion of
845 terms for AMV, the PDO, and the IOD in the model framework. The insensitivity of AAWR to

846 AMV extends to all of the other proxies for variations in the strength of the AMOC we have
847 considered. The modeled strength of the PDO varies noticeably depending on the proxies and
848 filtering methods chosen for both this climate signal and as well as AMV and RF due to aerosols.
849 Specifically, the contribution of the PDO to ΔT_{MDL} increases in magnitude with stronger-cooling
850 aerosol scenarios – but these model results do not show any strong effect on AAWR. We can
851 also run the EM-GC with specific single records for OHC instead of using the average of five
852 OHC data records; varying the input OHC time series does not produce any noticeable variation
853 in AAWR.

854 One EM-GC simplification that deserves mention is the lack of spatial variability in the
855 effect of the oceans. Rose et al. (2014) showed that the climatic effect of ocean heat uptake is
856 weaker if heat export from the atmosphere is concentrated in the tropics and stronger if heat
857 export is concentrated in high latitudes. While the EM-GC cannot directly separate the locality of
858 ocean heat export, it corroborates the Rose et al. (2014) result in the sense that almost all runs
859 show a stronger climatic signal from the AMOC (driven by high-latitude deep water formation)
860 and a weaker signal from the PDO (an expression of comparatively shallow-water heat storage in
861 the tropics (England et al., 2014); see §2.1.1 for a summary of the various AMOC and PDO
862 proxies tested). While various other MLR studies (Chylek et al., 2016; Zhou & Tung, 2013)
863 focus on the AMOC as the main oceanic driver of the climate system, other literature suggests
864 the PDO has a stronger influence on global temperature, either overall or specifically for the last
865 few decades (England et al., 2014; Steinman et al., 2015; Tokarska et al., 2019). Due to the
866 structure of MLR models, finding regression coefficients for time spans less than the
867 multidecadal characteristic time of known natural variability is not practical, nor is attempting to
868 define climate drivers using fewer total years than this characteristic time scale. Some research
869 suggests that the sign of the PDO is what drives trends in ΔT (England et al., 2014), meaning an
870 integral of the original PDO time series might be a stronger regressor. However, using a time
871 series calculated as such did not produce lower values of χ^2 or higher values of the PDO
872 regression coefficient than found using the raw PDO signal, further suggesting that AMOC is
873 likely the stronger driver of variations in ΔT .

874 Our method of determining AAWR is also relatively insensitive to the choice of
875 beginning and end years (**Table S3**). For example, using the EM-GC simulation shown in Figure
876 3, AAWR only varies from 0.130 to 0.156 °C/decade when we vary both the initial year (1975 to

877 1985) and final year (2006 to 2016) around the default AAWR time range of 1979 to 2010. This
878 insensitivity derives from the fact that ΔT_{HUMAN} follows from the known rise in CO_2 , CH_4 , and
879 N_2O that leads to a RF of climate due to GHGs that rises in a roughly linear manner over the past
880 four to five decades. Our calculation of AAWR is thus robust and, as detailed in the following
881 section, does a better job of isolating the underlying anthropogenic climate trend than methods
882 that rely on analysis of ΔT using the residual method.

883

884 3.2 Comparison to previous AAWR estimates

885 We assert that the slope of ΔT_{HUMAN} provides a more accurate method for quantifying
886 AAWR than the use of a residual method. As described in section §3.1, our median estimate of
887 AAWR with RCP 4.5 GHGs and “middle road” aerosols is $0.135\text{ }^\circ\text{C/decade}$, with range of
888 possible values extending from $0.089\text{ }^\circ\text{C/decade}$ to $0.197\text{ }^\circ\text{C/decade}$ based on uncertainty in RF
889 due to aerosols and climate feedback. The best estimate of AAWR given by FR11 for 1979 to
890 2010, upon analysis of ΔT from CRU3, is $0.170\text{ }^\circ\text{C/decade}$. The residual method used by FR11
891 involves finding the slope of observed ΔT after the contributions from solar irradiance,
892 volcanoes, and ENSO have been removed. By not including AMV (green curve in Figure 3c)
893 and by focusing their analysis solely on a 31 year period of time, FR11 do not account for the
894 significant warming trend that occurred from 1979 to 2010 that our analysis suggests is due to
895 natural variability and instead attributed this component of the rise in ΔT to anthropogenic
896 warming. Although the precise magnitude of the AMV influence is sensitive to how North
897 Atlantic SST is detrended (Canty et al., 2013) and smoothed, an independent analysis of SST
898 using spectral methods (DelSole et al., 2011) supports our suggestion that internal climate
899 variability contributed significantly to the relative warming over our default time period for
900 AAWR.

901 We note that Haustein et al. (2019) emphatically state “we argue that AMV must not be
902 used as a regressor” because “AMV is found to be primarily controlled by external forcing”.
903 Booth et al. (2012) implicate tropospheric aerosols due to pollution and stratospheric sulfate
904 aerosols due to major volcanic eruptions of the primary driver of SST variability in the North
905 Atlantic. There are numerous other studies making similar claims (Knight et al., 2005; Medhaug
906 & Furevik, 2011; Meehl et al., 2011; Stouffer et al., 2006), including a study of palaeocurrent
907 speed that extends over a time period of 230 years (Boessenkool et al., 2007), that suggests our

908 AMV proxy does represent interval variability of the climate record. Regardless, we find nearly
909 identical values of AAWR based on the slope of ΔT_{HUMAN} , with or without the use of AMV as a
910 term in the regression model (Figure S7a vs S7b). We are therefore confident FR11 have
911 overestimated the true value AAWR, either because there is a component of natural variability
912 present in the residual they have computed, or because their analysis is restricted to such a short
913 period of time. In contrast, our computation of AAWR for 1979 to 2010 is found using a
914 physical model that provides consistent treatment of RF due to GHGs, aerosols, and natural
915 factors such as ENSO, TSI, and SAOD, over a century and a half period, which mitigates a host
916 of potential complications present when one examines a residual (Silver, 2012).

917 Other studies suggest the PDO or changes in SAOD from minor volcanic eruptions could
918 have also played a role in driving variations of ΔT over this time period (e.g. Tokarska (2019)
919 and the references therein). Our estimates of AAWR include all of these factors and based on
920 analysis of data collected over a ~150 year time period; in our model framework the most
921 important natural drivers of ΔT over the past four to five decades are ENSO, major volcanic
922 eruptions, and AMV. If temperature is affected by a natural process not represented by the
923 exogenous factors used to compute the residual, then quantification of AAWR will be unduly
924 influenced (Supporting Information Text S2 and Figure S7). As shown in our SI, the difference
925 between our best estimate of AAWR and that given by FR11 is nearly completely explained by
926 the proper attribution of the signal from variations in the strength of AMOC.

927 Conversely, the estimate of AAWR over 1979 to 2010 provided by ZT13 upon
928 consideration of the variations in the strength of AMOC is likely biased low. They suggest
929 AAWR drops from 0.170 °C/decade in a regression without AMV to 0.070 °C/decade with
930 AMV included. Even though they considered AMV as a proxy for variations in the strength of
931 AMOC, they used a linear function to describe ΔT_{HUMAN} over the entire 1860 to 2010 time
932 period as an input to their MLR. We are able to closely reproduce their estimate of AAWR if we
933 replace our formulation of ΔT_{HUMAN} with a linear function spanning 1860 to 2010 (Supporting
934 Information Figure S7c+d). However, it is well known that anthropogenic RF of climate, which
935 drives ΔT_{HUMAN} , has varied in a non-linear manner that generally follows human population over
936 the past century and a half. While ZT13 state that the use of an RCP-shaped anthropogenic
937 forcing causes trends in their computed residual between ΔT_{OBS} and ΔT_{MDL} , we cannot
938 reproduce this result. With our use of RCP-based anthropogenic forcing that underlies the

939 CMIP5 GCMs, for the entire historical record (1850-present) and our method of calculating
940 AAWR, we find that both ΔT_{HUMAN} and AAWR are insensitive to the inclusion or exclusion of a
941 proxy for AMOC in the regression analysis (Supporting Information Text S2).

942 The uncertainty in AAWR is likely much higher than the small values suggested by FR11
943 and ZT13. As detailed in section §3.3, our estimate of AAWR based on the full uncertainty in
944 AER RF and analysis of ΔT_{OBS} from multiple data centers spans the range 0.08 °C/decade to
945 0.20 °C/decade. FR11 state that the computation of AAWR upon use of ΔT_{OBS} from various data
946 centers provides a range of 0.158 °C/decade to 0.187 °C/decade (these values are the 1 σ lower
947 and upper uncertainties of the standard error of their regression). The final estimate of AAWR
948 given by ZT13 is 0.05 °C/decade to 0.09 °C/decade based solely on the mathematical uncertainty
949 from calculating a linear fit to their ΔT_{HUMAN} . In our model framework, uncertainties in the
950 strength and temporal shape of AER RF over the past four decades cause ΔT_{HUMAN} to vary much
951 more than allowed by uncertainties from any linear fit to ΔT_{HUMAN} . The variation of AER RF
952 used in our study results in a range for AAWR of 0.089 to 0.197 °C/decade for a single ensemble
953 (Figure 4); this range extends slightly further to 0.084 to 0.202 °C/decade when considering all
954 ensembles. Figure 4 and **Figure S8** show that EM-GC runs with small amounts of aerosol
955 cooling tend to have both lower values of χ^2 (i.e good fits to the climate record span a wider
956 range of values for λ_{Σ}) and lower values of AAWR than model runs constrained by larger aerosol
957 cooling.

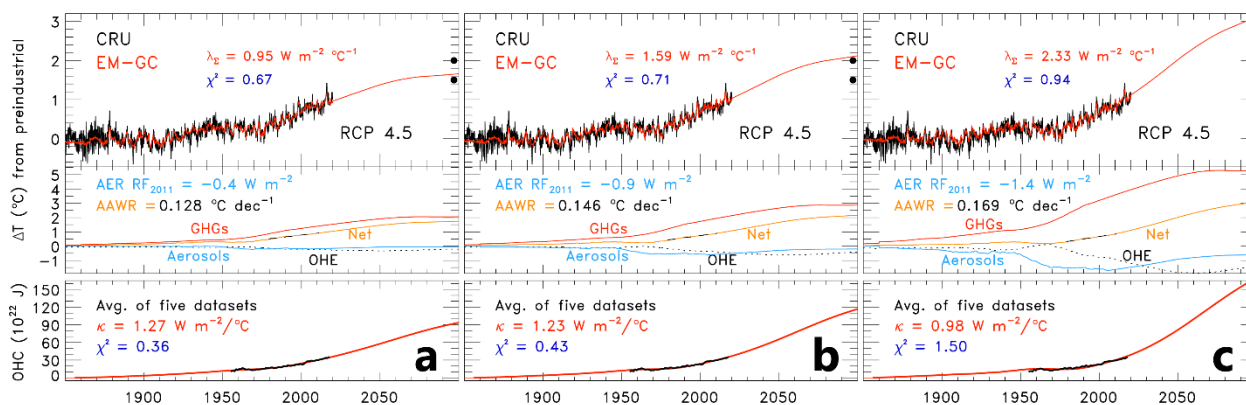
958 Individual runs demonstrating the effect AER RF has on ΔT_{HUMAN} and χ^2 are highlighted
959 in **Figure 6**. As AER RF cooling was largest in the 1970s and decreased in past decade (Smith
960 and Bond, 2014), larger aerosol cooling implies higher values of AAWR due to the nature of the
961 definition of ΔT_{HUMAN} (equation 6a). This relationship explains why Figure 6a, with a relatively
962 weak AER RF₂₀₁₁ value of -0.4 W/m^2 , has a relatively low AAWR value of 0.128 °C/decade;
963 conversely, the simulation in Figure 7c with strong aerosol cooling (AER RF₂₀₁₁ of -1.4 W/m^2)
964 results in a relatively high AAWR value of 0.169 °C/decade. If the global warming due to black
965 carbon aerosols and co-emitted species over the industrial era were as large as the best-estimate
966 of Bond et al. (2013), this term would place the actual value of AER RF₂₀₁₁ close to -0.4 W/m^2
967 rather than the AR5 best estimate of -0.9 W/m^2 , rendering AAWR well below the best estimate
968 of 0.170 °C/decade given by FR11. On the other hand, if the cooling of climate due to
969 anthropogenic aerosols was as large as suggested by the recent study of Shen et al. (2020), this

970 finding would likely place AER RF₂₀₁₁ close to -1.4 W/m^2 , leading to a value of AAWR similar
971 to the $0.170 \text{ }^\circ\text{C/decade}$ estimate of FR11. FR11 do not address the quite large uncertainty in
972 AAWR due to imprecise knowledge of the RF of climate by tropospheric aerosols.

973 There remains an important distinction to be made when comparing values of AAWR
974 based on specific estimates of AER RF₂₀₁₁. While Figure 6b shows that using an AER RF time
975 series with the AR5 best estimate for AER RF₂₀₁₁ (-0.9 W/m^2) gives an AAWR of 0.146
976 $^\circ\text{C/decade}$, whereas our weighted ensemble median value of AAWR is $0.135 \text{ }^\circ\text{C/decade}$. The
977 lower value for the ensemble median follows from how our χ^2 strength-of-fit filters eliminate
978 more runs with stronger aerosol cooling than runs with weaker aerosol cooling. Runs that use
979 weaker aerosol cooling have lower resulting values for AAWR, so even though our ensemble
980 weighting method theoretically assigns equal weighting to runs with -0.1 W/m^2 and -1.9 W/m^2 ,
981 the relative lack of high values of AAWR corresponding to stronger aerosol cooling that pass
982 this filter causes the weighted median AAWR to be slightly lower than $0.146 \text{ }^\circ\text{C/decade}$.

983 We state our estimate of AAWR for 1979 to 2010 as $0.14 \pm 0.06 \text{ }^\circ\text{C/decade}$, where the
984 uncertainty covers the full range of model runs that yield a good fit to ΔT_{OBS} from CRU4. Our
985 estimate of AAWR is larger than the trend in lower tropospheric temperature of 0.096 ± 0.012
986 $^\circ\text{C/decade}$ reported by CM17. Their estimate is based upon analysis of satellite and radiosonde
987 measurements of temperature throughout the global lower troposphere (GLT, the atmospheric
988 layer from the surface to approximately 300 hPa) over the time period Jan. 1979 to June 2017.
989 Similar to FR11, CM17 do not address the contribution of imprecise knowledge of AER RF to
990 their estimate of AAWR, which leads to their small uncertainty for AAWR compared to our
991 uncertainty. We reach similar results, though, when comparing the drop seen between the trend
992 in observed ΔT and the trend after removing natural components of ΔT . They report a significant
993 difference between the temperature trend for raw data ($0.155 \text{ }^\circ\text{C/decade}$) and the trend after the
994 data have been adjusted to account for natural influences due to major volcanoes and ENSO
995 ($0.095 \text{ }^\circ\text{C/decade}$). Our best estimate of AAWR for the Jan. 1979 to June 2017 time period,
996 based on a linear fit to ΔT_{HUMAN} shown in Figure 3a, remains $\sim 0.14 \text{ }^\circ\text{C/decade}$, compared to the
997 trend in ΔT_{OBS} of $\sim 0.18 \text{ }^\circ\text{C/decade}$ for this time period. As such, we compute the drop from the
998 trend in ΔT_{OBS} to trend in ΔT_{HUMAN} to be about two-thirds of the corresponding drop reported by
999 CM17. Given the presence of two major volcanic eruptions in the first half of this time period
1000 and a major ENSO event in 2015-16, the drop in value from the observed trend to the

1001 anthropogenic trend should be expected. We caution that precise determination of the effect of
 1002 major volcanic eruptions for analysis of GLT data collected during the satellite era is affected by
 1003 whether or not one includes the effect of AMV in the analysis (section 4.5 of Canty et al., 2013),
 1004 which may explain the difference between our drop and the drop from CM17. Finally, and most
 1005 importantly, CM17 emphasize (i.e. their figure 2) that CMIP5 GCM simulations of GLT result in
 1006 considerably more rapid warming than is discerned from their adjusted observations. We reach a
 1007 similar conclusion based on our analysis of ΔT , as described in the following section.
 1008
 1009



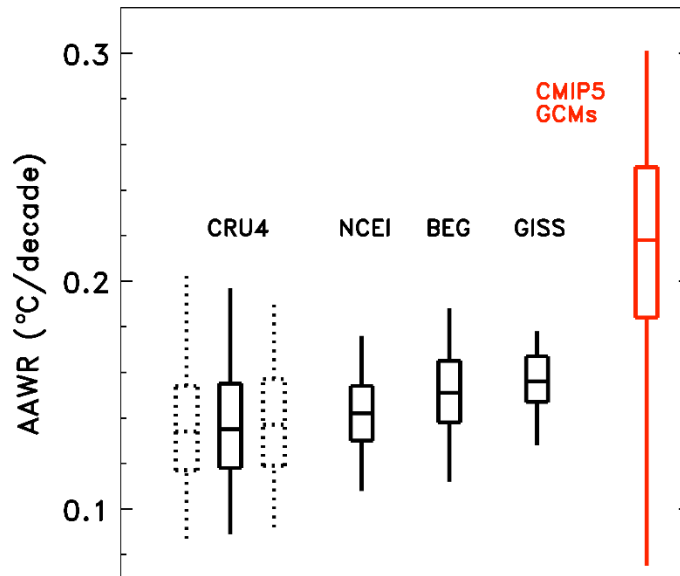
1010
 1011 **Figure 6.** Observed and modeled ΔT , 1850 to 2019, as well as projected global warming to
 1012 2100. The model runs pictured are identical to the run in Figure 3, except 7a and 7c use alternate
 1013 middle road constructions of AER RF. We show a run with AER RF₂₀₁₁ of -1.4 W m^{-2} instead
 1014 of -1.5 W m^{-2} because the simulation with -1.5 W m^{-2} exists at the far edge of acceptable χ^2
 1015 values, producing unrealistic individual anthropogenic components and OHC₂₁₀₀. (AER RF₂₀₁₁ of
 1016 -0.4 W m^{-2} to -1.5 W m^{-2} would match the upper and lower limits respectively of AR5’s likely
 1017 range of anthropogenic, tropospheric forcing values in 2011 relative to preindustrial values). The
 1018 upper rung of each abbreviated ladder plot here is the same format as those in figure 3a. The
 1019 second rungs show the anthropogenic effect on the climate in gold as well as three of its four
 1020 components: the temperature rise from GHG forcing (red), the temperature fall from aerosol
 1021 cooling (light blue), and the temperature fall from OHE (dashed black). For clarity, the LUC
 1022 component is not shown as its value is consistently near-zero compared to the other components.

1023
1024
1025
1026
1027
1028
1029
1030
1031
1032
1033
1034
1035
1036
1037
1038
1039
1040
1041
1042
1043
1044

3.3 Comparison to AAWR from GCMs

In this section, we conduct a comparison of estimates of AAWR found using our EM-GC to AAWR inferred from CMIP5 GCMs. First, we further characterize uncertainties in AAWR. **Figure 7** shows the sensitivity of AAWR to AER RF and the choice of data record for ΔT_{OBS} . The middle of box and whicker (BW) plot under the label CRU4 summarizes the weighted median (0.135 °C/decade), weighted interquartile range (IQR), and extrema of AAWR for the EM-GC determined PDF shown in Figure 5a.

The EM-GC ensembles shown thus far relied only on time series of AER RF found using scaling factors for aerosol cooling (α_{COOL}) and heating (α_{HEAT}) along the “middle road” of Figure S4 (section §2.1.2). The shape of the AER RF time series varies by choosing values for α_{COOL} and α_{HEAT} along either the “low” or “high” road of Figure S4. The dashed BW plots surrounding the solid BW labeled CRU4 show the AAWR ensemble changes by a small amount, upon modification of the shape of the input AER RF time series. Scatter plots of AAWR versus AER RF₂₀₁₁ and λ_{Σ} as well as ladder plots documenting the computation of ΔT_{HUMAN} and AAWR for the AR5 best estimate of AER RF₂₀₁₁, for these “high” and “low” road simulations, are shown in **Figures S8** and **S9**. The value of AAWR exhibits only a small sensitivity to variation of the shape of AER RF. We include this comparison for the CRU4 record of ΔT_{OBS} because the various time series for AER RF that underlie the model inputs for these simulations cover a large range of possibilities, similar to that shown in figure 4 of Smith & Bond (2014).



1045
 1046 **Figure 7.** Comparison of EM-GC values of AAWR to CMIP5 GCM values of AAWR, for 1979
 1047 to 2010. Each black box-and-whisker plot shows the weighted median, weighted IQR, and
 1048 extrema from PDFs for AAWR found using the EM-GC, as shown in Figure 5. The solid black
 1049 box-and-whisker plots represent EM-GC ensembles fit to records of ΔT_{OBS} from various data
 1050 centers (as indicated), found using RF from RCP 4.5 with the middle road construction of AER
 1051 RF as shown in Figure S4. The dashed box-and-whisker plots show AAWR for ΔT_{OBS} from
 1052 CRU4, found using the low (left) and high (right) road constructions for AER RF (section
 1053 §2.1.2); for simplicity, this comparison is not shown for the other temperature records. Among
 1054 all of the EM-GC results, the maximum value of AAWR is 0.202 °C/decade and minimum is
 1055 0.084 °C/decade. The red box and whisker plot at the right shows AAWR found using the
 1056 regression method described in section §2.4, using archived output of ΔT from 112 individual
 1057 CMIP5 GCM runs, all constrained by RCP 4.5.

1058
 1059 The choice of data center for the ΔT_{OBS} record contributes another small uncertainty to
 1060 AAWR. Figure 7 shows BW plots for ΔT_{OBS} from other data centers. The median values of
 1061 AAWR for AER RF computed with α_{COOL} and α_{HEAT} along the “middle road” of Figure S4 are
 1062 0.142, 0.151, and 0.156 °C/decade for the use of temperature data from NCEI, BEG, and GISS,
 1063 respectively. The choice of data center exerts a difference of 0.021 °C/decade between the largest
 1064 and smallest median values, which is quite a bit larger than the value of 0.005 °C/decade
 1065 difference reported by FR11 for selection of data between CRU3, NCDC (this dataset is now

1066 termed NCEI), and GISS. We find the largest value of AAWR upon use of ΔT_{OBS} from GISS
1067 and the smallest value upon use of data from CRU4. We have featured data from CRU4
1068 throughout our paper, as well as in our earlier studies (Canty et al., 2013; Hope et al., 2017)
1069 because so many other published papers over the prior decade have used CRU temperature
1070 records as their baseline dataset. The 0.021 °C/decade difference in AAWR that arises between
1071 our use of ΔT from CRU4 compared to GISS is much smaller than the difference between any
1072 AAWR from the EM-GC and the Coupled Model Intercomparison Project (CMIP5) (Taylor et
1073 al., 2012) GCM multi-model mean value of AAWR.

1074 The far-right red BW plot in Figure 7 shows AAWR from the CMIP5 GCMs used by
1075 AR5. Archived output from the CMIP5 (Taylor et al., 2012) for 112 runs of 41 GCMs driven by
1076 RCP 4.5 (Thomson et al., 2011) has been used to estimate AAWR from these GCM results
1077 (Supporting Information Text S1). We find good agreement between values of AAWR from
1078 these 112 runs found using two analysis methods, termed linear fit (LIN) and regression (REG)
1079 (Supporting Information **Figure S10, Figure S11, and Table S4**). For the AAWR found using
1080 LIN, we perform a linear least squares regression to archived output of global mean two-meter
1081 air temperature (TAS) or years 1979 to 2010, ignoring years with obvious of major volcanic
1082 eruptions (1982, 1983, 1991, and 1992). The rationale behind this method is natural variability in
1083 TAS due to internally model generated ENSO events will be randomly distributed in time; the
1084 influence of variations in the strength of AMOC on TAS tend to be small within these GCMs
1085 (Kavvada et al., 2013). For AAWR found using REG, we perform a multiple linear regression of
1086 TAS versus TSI and SAOD in a two-step process, as described in section 2.6 of Hope et al.
1087 (2017). Values of AAWR found using both methods are also given in Table S4 for each GCM.
1088 Comparing AAWR from LIN versus REG shows the two methods result in values of AAWR
1089 with a high correlation coefficient ($r^2 \geq 0.95$) and a mean ratio close to 1, providing confidence
1090 that AAWR has been computed accurately from the CMIP5 GCMs.

1091 All of the CMIP5 GCM output used here are global, two-meter air temperature (TAS)
1092 data. According to Cowtan et al. (2015), the blending of TAS (over land) with GCM output of
1093 sea surface temperature (SST, termed TOS in the CMIP5 archive) provides a more appropriate
1094 manner for sampling GCM output than use of global TAS, since datasets such as CRU4-based
1095 ΔT are a combination of near surface air temperature over land and SST over water. Cowtan et
1096 al. (2015) state the use of blended temperature rather than air temperature accounts for 25% of

1097 the difference between the GCM-based and observed variations in global temperature over
1098 2009–2013 and 38% of this difference over 1975-2014. Our own analysis using TAS-TOS
1099 blended temperature from CMIP5 GCMs results in a reduction of AAWR by roughly 2-5%,
1100 depending on which GCM is considered. This 2-5% reduction in GCM-AAWR translates to
1101 explaining 6-14% of the difference between median GCM-based and median EMGC-based
1102 values of AAWR, as well as 11-28% of the difference between GCM-based AAWR and the
1103 observed CRU4 slope of 0.18 °C/decade over the AAWR time period. While our use of blended
1104 temperature from a handful of CMIP5 GCMs rather than TAS does lead to a reduction in GCM-
1105 based values of AAWR, we find this effect is small (i.e. 2 to 5 %). A similar conclusion was
1106 reached by Tokarska et al. (2020). Therefore, other than this paragraph, our paper focuses
1107 entirely on TAS from the GCMs because the use of blended temperature introduces a modest
1108 effect that does not alter any of our major conclusions, plus the information needed to produce
1109 blended temperature is no longer available on the CMIP5 archive for enough GCMs to complete
1110 an ensemble similar in size to our initial the GCM ensemble shown in Figures 4 and 5.

1111 The median value of the CMIP5 GCM-based AAWR found with the regression method
1112 0.22 °C/decade. This value for AAWR is slightly more than 50% larger than our best empirical
1113 estimate of 0.14 °C/decade. The IQR for AAWR inferred from CMIP5 GCMs is 0.184 to 0.250
1114 °C/decade, and the extrema are 0.075 and 0.301 °C/decade. More than two-thirds of the 112
1115 archived CMIP5 GCM runs (Table S4) exhibit a value for AAWR larger than our upper limit of
1116 0.202 °C/decade, and there is no overlap between the CMIP5 IQR and any IQR from the EM-GC
1117 – the 25th percentile of the CMIP5 ensemble is 0.184 °C/decade, while the highest 75th percentile
1118 from an EM-GC ensemble is 0.167 °C/decade (Figure 7, GISS). Also, only 3 of the 41 CMIP5
1119 GCMs exhibit a value of AAWR less than 0.14 °C/decade: INM-CM4 (Volodin et al., 2010),
1120 IPSL-CM5B-LR (Hourdin et al., 2013), and MRI-CGCM3 (Yukimoto et al., 2012) (Table S4).
1121 We conclude therefore that the large majority of the CMIP5 GCMs exhibit anthropogenically
1122 induced warming that is considerably more rapid than what has actually occurred over the time
1123 period 1979 to 2010. This finding is not closely tied to the chosen time period for AAWR:
1124 whereas AAWR does exhibit some dependence on start and end year (Table S3), the median
1125 value of CMIP5 GCM-based AAWR exceeds these empirical values by about the same amount
1126 for any similar time period. The tendency of most GCMs to overestimate empirical AAWR is
1127 evident in plots of time series of archived ΔT shown in AR5 (i.e. figure 11.25a) and persists

1128 whether the GCM output is examined in terms of individual runs, various GCMs, or specific
1129 modeling centers (Supporting Information Figure S11, Table S4). A similar tendency of GCM-
1130 based warming rates to lie considerably above empirical estimates has been noted by multiple
1131 recent, complementary studies (Christy & McNider, 2017; Chylek et al., 2014; Fyfe et al., 2013;
1132 Millar et al., 2017; Tokarska et al., 2020).

1133 A GCM retrospective paper by Hausfather et al. (2020) shows that many past GCMs
1134 have predicted the observed rise in ΔT quite well. By comparing older GCM predictions of ΔT to
1135 the rise in ΔT_{OBS} since those predictions were made, Hausfather et al. (2020) show that the skill
1136 in predicting $\Delta T/\Delta t$ up to 2017 increased through the first three IPCC assessment reports. This
1137 ability to predictively match $\Delta T/\Delta t$ with the realized ΔT_{OBS} is quantified with unitless skill
1138 values, which increase from 0.63 to 0.73 to 0.81 for the first three assessment reports. However,
1139 the predictions of ΔT_{OBS} for GCMs used in the fourth IPCC assessment report overestimated
1140 observed $\Delta T/\Delta t$ from 2007-2017, resulting in an overall skill value of 0.56 despite being a short-
1141 term prediction using the most advanced GCMs available at the time. While this excess warming
1142 in the GCMs that underlie the fourth report is argued to be due to overestimated scenario RF,
1143 excess warming continued into the AR5 GCMs with CMIP5, as documented here and in figure
1144 11.25b of AR5. Early indications are that the tendency for GCMs to warm more quickly than the
1145 actual climate system extends into the CMIP6 GCMs being used as the backbone of the sixth
1146 assessment report (Belcher et al., 2019; Tokarska et al., 2020; Voosen, 2019). While the increase
1147 in GCM complexity over the years certainly provides many benefits, it appears that such
1148 complexity has had the unintended consequence of providing a noticeable warming bias
1149 compared to older GCMs.

1150 It is possible that some of the differences between AAWR found using our EM-GC and
1151 that inferred from CMIP5 GCMs are due to unaccounted internal variability in the observed
1152 temperature record. In particular, common explanations for the inability of models to match the
1153 lack of warming from 1998-2012 include shifts in the PDO and the strength of SAOD from
1154 minor volcanic eruptions (England et al., 2014; Tokarska et al., 2019), as well as variations in
1155 transport of heat to the deep ocean (Meehl et al, 2011) that we have attempted to simulate using
1156 AMV as a proxy for the strength of AMOC. Some members of the EM-GC ensemble produce
1157 results consistent with a climatically important role for the PDO: as mentioned in sections §2.1.1
1158 and §3.1, simulations with high values of AER RF₂₀₁₁ show relatively stronger influence of the

1159 PDO and relatively weaker influence of AMOC compared to the results shown in Figure 3.
1160 These ensemble members also result in an increase in the climatic importance of SAOD
1161 following major volcanic eruptions (Canty et al., 2013). However, consistent with the conclusion
1162 of Chylek et al. (2020), we find enhancements of SAOD due to recent minor eruptions to have a
1163 negligible effect on ΔT for all members of our EM-GC ensemble. The very low values of
1164 globally averaged SAOD following minor eruptions in the past decade will not noticeably affect
1165 ΔT , unless the climate response to SAOD is highly nonlinear.

1166

1167 3.4 The effects of aerosols and climate feedback on future ΔT

1168 We turn our attention to the effects of the radiative forcing due to AER RF and λ_{Σ} on
1169 future projections of ΔT . Figure 6, in addition to showing the effect on AAWR of varying the
1170 input model time series for AER RF, also shows how these three simulations differ in ΔT out to
1171 year 2100 (ΔT_{2100}). The projection of ΔT is produced by applying the solutions for λ_{Σ} and κ that
1172 best fit the historical record to the prescribed GHG forcing pathways of RCP 4.5 out to the end
1173 of this century. Natural variations of all climatically important factors are assumed to be zero in
1174 the future to highlight only the rise in human driven rise in the global mean surface temperature
1175 anomaly (ΔT_{HUMAN}). We focus on projecting the underlying trend of future warming due to
1176 anthropogenic GHGs, as opposed to attempting to predict year-to-year variations in
1177 temperatures.

1178 The full historical time series for ΔT can be fit reasonably well ($\chi^2 \leq 2$) for many
1179 combinations of time series of AER RF (indexed by their value in 2011) and value of λ_{Σ} . As a
1180 result, there exist a wide range of possible future temperature projections assuming the value for
1181 the sum of climate feedback mechanisms needed to simulate prior warming will persist into the
1182 future. This ability to fit the historical global temperature record with a wide range of possible
1183 climate feedback values is the main source of the resulting uncertainty in our estimate of ΔT_{2100} .
1184 If aerosol cooling to date has been low, then aerosols have counteracted only a small amount of
1185 the GHG forcing that warms the atmosphere, necessitating a low value of λ_{Σ} , resulting in modest
1186 future warming. By the same logic, a high amount of aerosol cooling to date leads to a large
1187 amount of future warming (Goodwin et al., 2018; Kiehl, 2007; Knutti & Hegerl, 2008).

1188 Figure 6a shows a value for ΔT_{2100} of just 1.7°C for weak aerosol cooling (AER RF₂₀₁₁ of
1189 -0.4 W/m^2) offsetting the warming from RCP 4.5 GHGs. Conversely, if aerosol cooling has been

1190 large (AER RF₂₀₁₁ of -1.4 W/m^2), global warming will be much more intense: Figure 6c shows a
1191 ΔT_{2100} slightly above 3.1°C . Warming can reach over 4°C by 2100, still with RCP 4.5 GHGs, for
1192 the upper range of aerosol cooling scenarios stated in AR5 (i.e. AER RF₂₀₁₁ from -1.6 W/m^2 to $-$
1193 1.9 W/m^2). However, under these strong aerosol cooling scenarios, it is not possible in our
1194 modeling framework to obtain values of χ^2 below 2 for the full historical ΔT fit and particularly
1195 for the OHC fit, which is why the largest aerosol cooling case shown in Figure 6c is for AER
1196 RF₂₀₁₁ of -1.4 W/m^2 . The individual simulations pictured in Figure 6 were chosen by finding the
1197 value of λ_Σ that minimizes χ^2 over the entire CRU4 record of ΔT (equation 1c), for each value of
1198 AER RF₂₀₁₁. This difference in ΔT_{2100} results from the fact that aerosol concentrations, and thus
1199 aerosol forcings, are set to return to near-zero values in the future as an effect of air quality
1200 regulations that arise from human health concerns (Smith & Bond, 2014). As such, all
1201 simulations approach the same net human RF by 2100 but have different values of λ_Σ based on
1202 the amount of GHG RF that was offset by anthropogenic aerosols over the historical record.

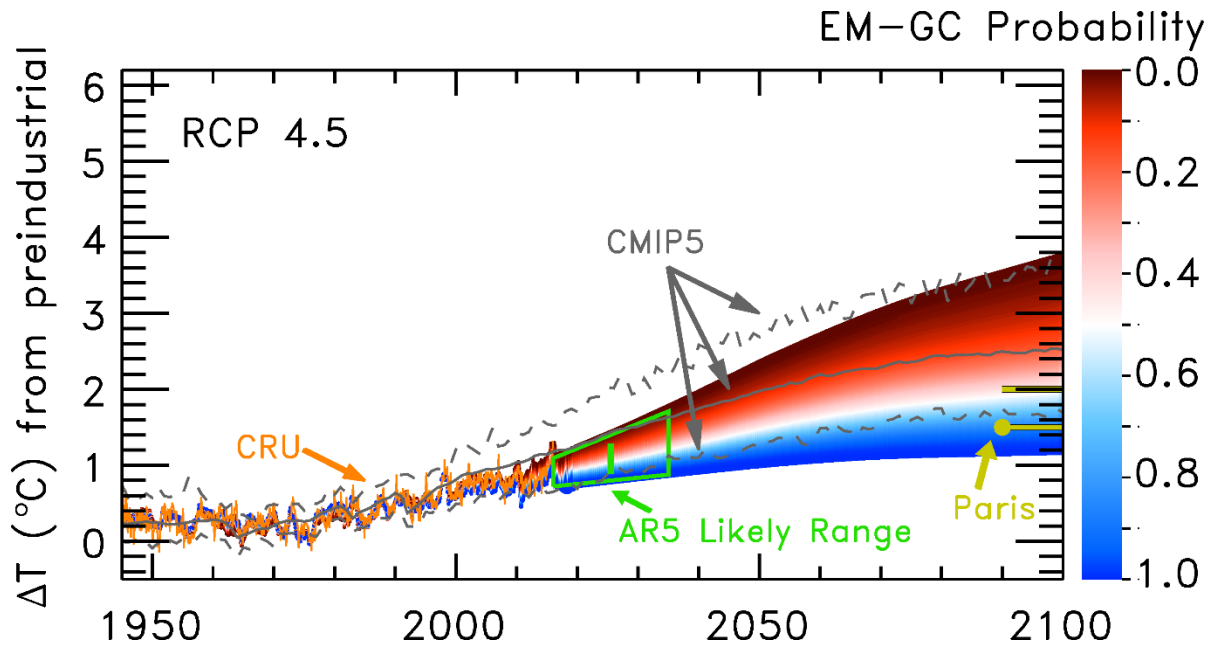
1203 Figure 4c shows ΔT_{2100} as a function of λ_Σ and AER RF₂₀₁₁ for RCP 4.5. Figure 5b shows
1204 a PDF of ΔT_{2100} for the ensemble members shown in Figure 4c, computed using the weighting
1205 method based on the AR5 likelihoods for the values of AER RF₂₀₁₁ (Figure 4a) described in
1206 section §3.1. Figures 4c and 5b illustrate a vitally important aspect of the climate system: the
1207 present uncertainty in the amount of GHG warming offset by aerosols causes a large spread in
1208 future warming, for a single future GHG abundance scenario, in this case RCP 4.5. If warming
1209 due to black carbon aerosols and co-emitted species were as large as the best-estimate of Bond et
1210 al. (2013), this term would place the actual value of AER RF₂₀₁₁ close to -0.4 W/m^2 , resulting in
1211 values of ΔT_{2100} in our model framework close to the low end (i.e. 1.20°C) of this forecast. On
1212 the other hand, if the climate cooling due to aerosols was as large as suggested by Shen et al.
1213 (2020), values of ΔT_{2100} would lie towards the high close on end (i.e. 3.74°C) of our forecast. A
1214 reduction in the uncertainty of the amount of warming offset by tropospheric aerosols for the
1215 contemporary atmosphere, which requires obtaining consensus on the role of black carbon (Bond
1216 et al., 2013) as well as various aerosol indirect effects (Chen & Penner, 2005; Gryspeerdt et al.,
1217 2020), would enable more accurate forecasts of end of century warming.

1218 A PDF of ΔT_{2100} for the output from 41 GCMs is also shown in Figure 5b. For GCMs
1219 that have submitted multiple runs using RCP 4.5 to the CMIP5 archive, ΔT in year 2100 is first
1220 averaged for these runs, such that the PDF consists of the distribution of ΔT_{2100} for the 41 GCMs

1221 shown in Table S4. The median warming of T_{2100} from our EM-GC simulations for RCP 4.5 is
1222 2.00 °C, with lower and upper limits of 1.20 and 3.74 °C, respectively. The median ΔT_{2100} from
1223 the 41 GCMs is 2.52 °C, with lower and upper limits of 1.69 and 3.64 °C. Only 7 of the 41
1224 CMIP5 GCMs exhibit a value for ΔT_{2100} less than the EM-GC median of 2 °C.

1225 **Figure 8** shows a probabilistic forecast of the future rise in ΔT from our EM-GC for RCP
1226 4.5. Colors denote the probability of reaching at least that temperature by each year. The figure
1227 also contains the CMIP5 GCM ensemble minimum, multi-model mean, and maximum values of
1228 ΔT (gray lines) as well as the likely range of warming (green trapezoid) from figure 11.25b of
1229 AR5 (Kirtman et al., 2013). Temperature projections from our EM-GC agree well with the
1230 expert judgement of the near-future rise ΔT provided by Chapter 11 of AR5. The white color in
1231 Figure 8 for EM-GC probability is the median warming projection in our model framework.
1232 Similar to the comparison shown in section §3.3 for AAWR, projections of warming from the
1233 CMIP5 GCMs tend, on average, to be larger than the warming projection from our empirical
1234 model of global climate. Notably from a policy perspective, our most likely outcome for ΔT lies
1235 slightly above the CMIP5 GCM multi-model minimum, with both the EM-GC-based median and
1236 the GCM-based minimum lying below the Paris Climate upper limit of 2 °C. As explored further
1237 in section §3.7, carbon emissions consistent with the CO₂ trajectory of RCP 4.5 provide a more
1238 likely chance of limiting global warming to either the Paris goal (1.5 °C) or upper limit (2 °C)
1239 than is projected by CMIP5 GCMs constrained by RCP 4.5. Most notably, observed ΔT over the
1240 years ~2005 to 2020 lies between the CMIP5 GCM multi-model minimum and mean, which of
1241 course was the driving factor behind the formulation of the green trapezoid in Figure 8 by the
1242 authors of Chapter 11 of AR5 (Kirtman et al., 2013).

1243



1244
 1245 **Figure 8.** Global warming projections for RCP 4.5 relative to the preindustrial baseline. The
 1246 EM-GC ensemble is shown with red-to-blue envelope and the CMIP5 GCM ensemble is shown
 1247 with grey lines. Color at any given point within the EM-GC envelope represents the chance of
 1248 ΔT reaching at least that temperature at that time. The three CMIP5 lines represent the minimum,
 1249 multi-model mean, and maximum of ΔT from the GCMs that submitted projections of each RCP
 1250 scenario respectively to the CMIP5 archive (grey lines). One set of observed temperatures to date
 1251 (CRU4, orange line), the expert judgement from Figure 11.25 of AR5 (green trapezoid and
 1252 vertical bar), and the targets of the Paris Agreement (gold spikes at right) are also shown for
 1253 comparison.

1254
 1255

1256 The values of λ_{Σ} for the EM-GC-based projections shown above suggest less future
 1257 warming than similar values provided by most CMIP5 GCMs. Table 9.5 of AR5 (Flato et al.,
 1258 2013) suggests model mean values for λ_{Σ} of 1.6, 2.04, or 2.15 $\text{W/m}^2/\text{°C}$ depending on which
 1259 quantities are used to infer λ_{Σ} ; specifically, the first value is the sum of the average value of the
 1260 four individual feedbacks, the second value is based upon their estimate of ECS and the RF
 1261 associated with $2\times\text{CO}_2$, and the third value is based upon the values for the climate sensitivity
 1262 parameter and climate feedback parameter given. Table 1 of Sherwood et al. (Sherwood et al.,
 1263 2020) gives a value for λ_{Σ} of 1.9 $\text{W/m}^2/\text{°C}$, with a 66% confidence range of 1.46 to 2.34

1264 W/m²/°C. Although tabulations of λ_{Σ} from CMIP5 models exist (Andrews et al., 2012; Forster et
1265 al., 2013; Vial et al., 2013), particularly Table 9.5 of AR5 (Flato et al., 2013) and Table 1 and
1266 Figure 4 of Sherwood et al. (Sherwood et al., 2020), comparison to our values is complicated by
1267 the sensitivity of λ_{Σ} to AER RF for good fits to the climate record (Figure 4). In general, our λ_{Σ}
1268 (and thus λ) suggest less future warming than those from the CMIP5 GCMs.

1269 An important assumption for our quantification of both AAWR and ΔT_{2100} using the EM-
1270 GC is that λ_{Σ} (and thus λ) has remained constant over time. However, we can also simulate time
1271 dependent climate feedback to address the possibility that λ_{Σ} may change over time (section
1272 12.5.3 of AR5 and references therein; also Rose et al. (2014), Shindell (2014), and Marvel et al.
1273 (2018)). Recall that $1/\lambda = (1 + \gamma)/\lambda_p = 1/(\lambda_p - \lambda_{\Sigma})$ from equations 5 and 6; we have used λ_{Σ}
1274 up to this point as simulations with higher values of λ_{Σ} have higher future ΔT . For this reason,
1275 we prefer to examine a time dependent λ in terms of its inverse, $1/\lambda$, also known as the climate
1276 sensitivity parameter, because this quantity also has a positive correlation with ΔT . Figure S6
1277 and Table S2 summarize how ΔT_{2100} changes if we allow $1/\lambda$ to vary over time while still
1278 keeping the strength of fit between ΔT_{OBS} and ΔT_{MDL} at acceptable levels ($\chi^2 \leq 2$) for either the
1279 full historical time period or the most recent 80 years.

1280 For four different cases of aerosol forcing, we find that allowing $1/\lambda$ to scale with
1281 anthropogenic forcing while still keeping $\chi^2 \leq 2$ over the full historical time period results in
1282 roughly doubling of ΔT_{2100} compared to the constant feedback case (Table S2). This scenario
1283 with time-varying feedback, which results in our maximum warming, implies an increase in $1/\lambda$
1284 by nearly a factor of three over two and a half centuries (Figure S6e). This rise in $1/\lambda$ is much
1285 more rapid than expected. Even one of the most extreme estimates from recent work (Marvel et
1286 al., 2018) suggests an increase in median estimated equilibrium climate sensitivity (ECS) from
1287 1.8°C (for simulations constrained to match data acquired over 1979-2005) to a long-term (end
1288 of century) value of 3.1°C, which corresponds to a 72% increase. This rise in ECS postulated by
1289 Marvel et al. (2018) is predicated on the assumption that current atmospheric and oceanic
1290 conditions are truly exceptional. The validity of preliminary results for a handful of CMIP6
1291 models suggesting even higher ECS (Belcher et al., 2019; Gettelman et al., 2019; Zelinka et al.,
1292 2020) has been questioned by numerous recent papers based upon analysis of paleoclimate data
1293 as well as climatic conditions over the past several decades (Forster et al., 2020; Nijssen et al.,
1294 2020; Sherwood et al., 2020; Voosen, 2019; Zhu et al., 2020). Such scenarios that greatly

1295 increase $1/\lambda$ by the end of the century also produces a time dependent drift in the residual
1296 between observed and modeled over the historical record in our model framework (Figure S6f).
1297 Coincidentally, the comparison between modeled and measured ΔT in Figure S6f looks similar
1298 to the comparison of the CMIP5 GCM multi-model mean and ΔT_{OBS} shown in Figure 2. This
1299 time dependent drift between ΔT_{OBS} and our modeled ΔT , combined with the large temporal
1300 change in λ that underlies this simulation, suggests this might be an unreasonable scenario for
1301 use in CO₂ emission mitigation strategies.

1302 We also calculate a medium-varying feedback case by considering a $\chi^2 \leq 2$ strength-of-fit
1303 restriction that focuses only on the most recent 80 years of the ΔT_{OBS} record (Figure S6c,d)
1304 instead of $\chi^2 \leq 2$ over the full ΔT_{OBS} time series. This scenario results in a simulation of ΔT that
1305 appears more reasonable upon inspection of the residuals and the smaller rise in $1/\lambda$. However,
1306 depending on the strength of AER RF, the increase in $1/\lambda$ can still range from roughly 50% to
1307 more than a factor of two (Table S2). Changes in $1/\lambda$ of this magnitude over two and a half
1308 centuries are faster than the millennia-order timescale changes usually referenced (e.g. section
1309 12.5.3 of AR5 and references therein) when discussing noticeable changes in λ , ECS, and other
1310 related quantities such as transient climate sensitivity (TCS). While a factor of two or more rise
1311 in $1/\lambda$ does not match literature, an increase of roughly 50% falls in line with a 50% increase in
1312 TCS (Shindell, 2014) and neatly between the 28% increase (1.8 °C to 2.3 °C) and the 72%
1313 increase (1.8 °C to 3.1 °C) (Marvel et al., 2018) seen in other re-analyses of historical forcing
1314 results from GCMs. As there is no strong evidence from the climate record for a noticeable rise
1315 in $1/\lambda$ on the multidecadal time scale consistent with the simulations shown in Fig S6, we assert
1316 that the assumption of constant feedback within the EM-GC framework seems to be a reasonable
1317 assumption for the next few decades. There also certainly exists the possibility that by end of
1318 century, the rise in ΔT could be a few tenths of a degree warmer than our current best estimates
1319 assuming constant λ_{Σ} due to a slow rise in $1/\lambda$.

1320 We also assume for our computation of Q_{OCEAN} that κ is constant over time. This
1321 assumption follows from the fact that, like λ , the rate of change of κ is most likely small enough
1322 to not have a significant effect on the time scale of our calculations of ΔT (Raper et al., 2002).
1323 Our application of κ requires a monotonic increase in the magnitude of this term, we solve for
1324 Q_{OCEAN} based on $\Delta T_{ATM,HUMAN}$ instead of total ΔT_{MDL} because the latter displays strong natural
1325 variability and thus is not monotonically increasing. The anthropogenically-forced temperature

1326 itself is not strictly monotonic either, especially for AER RF time series corresponding to more
1327 negative values of AER RF₂₀₁₁, but the short, small, instances of cooling in those scenarios are
1328 relatively insignificant. Also, those cooling instances are pre-1950, and the OHC record we fit
1329 does not extend earlier than 1950. As such, the few instances when ΔT_{HUMAN} includes short,
1330 small cooling periods should not affect the overall approximation of κ as a constant. As with λ
1331 and fitting ΔT_{OBS} , a constant value of κ results in modeled OHC that fits the observed OHC quite
1332 well (Figure 3b and Figure 6).

1333 Model treatment of aerosols and clouds are two possible explanations for why λ from the
1334 EM-GC differs from CMIP5 models. About half of the CMIP5 GCMs do not include aerosol
1335 indirect effects (Schmidt et al., 2014). A lack of the indirect effect in our EM-GC would result in
1336 cooler projections of future ΔT , as less total AER RF over the historical record would favor
1337 lower values of λ_{Σ} and thus lower ΔT_{2100} . Such a relationship between ΔT_{2100} and the presence of
1338 the indirect effect does seem to appear in CMIP5 results as well: models without the indirect
1339 aerosol effect consistently warm less from 2014 to 2100 than models that do include it (Chylek et
1340 al., 2016). Considering that the CMIP5 GCMs tend to warm more than the EM-GC in terms of
1341 both AAWR (§3.3) and ΔT_{2100} (§3.5), a lack of the indirect effect in some GCMs does not
1342 explain the excess warming in GCMs, meaning it seems more likely that the difference between
1343 the EM-GC and CMIP5 GCMs lies in cloud feedback. (This should not eliminate considerations
1344 of aerosols and their complex interactions, however, especially given that aerosol indirect effects
1345 and cloud feedback processes are related.) It is widely known that uncertainty in the cloud
1346 feedback is much larger than that of other major feedbacks and this uncertainty is a main driver
1347 for the spread between CMIP5 models (Dolinar et al., 2015; Stocker et al., 2013; Zhou et al.,
1348 2015). While the fourth IPCC report (Solomon, 2007) suggested a cloud response spread
1349 centered around zero feedback within the CMIP3 GCMs, AR5 suggests a largely positive cloud
1350 feedback, in line with some recent observations (Dolinar et al., 2015; Zhou et al., 2015).
1351 However, there is considerable spread in the determination of cloud feedback from observations,
1352 including the possibility of a neutral or even negative feedback (Ceppi et al., 2017; Vial et al.,
1353 2013; Zelinka et al., 2016). While some recent studies suggest that cloud feedback and overall
1354 ECS interpreted from observation are higher than those from modeling studies based solely on
1355 observations since 2000 (Dessler, 2013; Sherwood et al., 2020), other observational studies offer
1356 lower ECS values than those found in modeling studies (Lewis & Curry, 2018; Masters, 2014;

1357 Otto et al., 2013; Schwartz, 2012). If the actual cloud feedback is less positive than the models
1358 currently suggest, that could also be a factor in the high bias of GCMs for AAWR, ECS, and
1359 ΔT_{2100} (Hope et al., 2017; Tokarska et al., 2020; Weaver et al., 2020; Zelinka et al., 2020).

1360

1361 3.5 Other RCPs and comparisons to projections from GCMs

1362 One advantage of simple models such as the EM-GC is the ability to perform sensitivity
1363 testing by completing many more runs of the model with less computing power. For example,
1364 each ensemble represented in Figure 7, originally consisting of 160,000 simulations, takes
1365 roughly two hours to complete. All those ensembles focus on ΔT_{HUMAN} driven by RF from GHG
1366 abundances from RCP 4.5, and a full treatment of the effects of uncertainty in RF due to
1367 aerosols. **Figures 9a and 10a**, driven by RCP 2.6, and **Figures 9b and 10b**, driven by RCP 8.5,
1368 show the results of EM-GC ensembles constrained by low and high ends of RF tested in CMIP5,
1369 respectively. The panels of Figure 9 and Figure 10 are the same as Figure 4b and Figure 5b,
1370 respectively, except for the different RCP scenario driving the ensembles. As the RCP scenarios
1371 are identical up to 2005 and do not differ greatly until after 2020, the shape of the model output
1372 shown in Figure 4b and Figure 9 are nearly identical, because the three χ^2 calculations (fits to
1373 total ΔT , recent ΔT , and OHC) used to select good fits to the climate record consider only
1374 historical data. The difference in end-of-century RF drives the differences in ΔT_{2100} , shown both
1375 in the colors of the model output and the positions of the PDFs in Figure 5b, Figure 10a, and
1376 Figure 10b. The probabilities of the rise in ΔT_{2100} staying beneath 2°C are 92%, 50%, and 0% for
1377 RCP 2.6, 4.5, and 8.5 respectively; probabilities for ΔT_{2100} remaining below 1.5°C fall to 67%,
1378 10%, and 0%. For RCP 6.0, (not pictured,) the probability of staying beneath 2°C is 20%, which
1379 falls to 0.1% for 1.5°C .

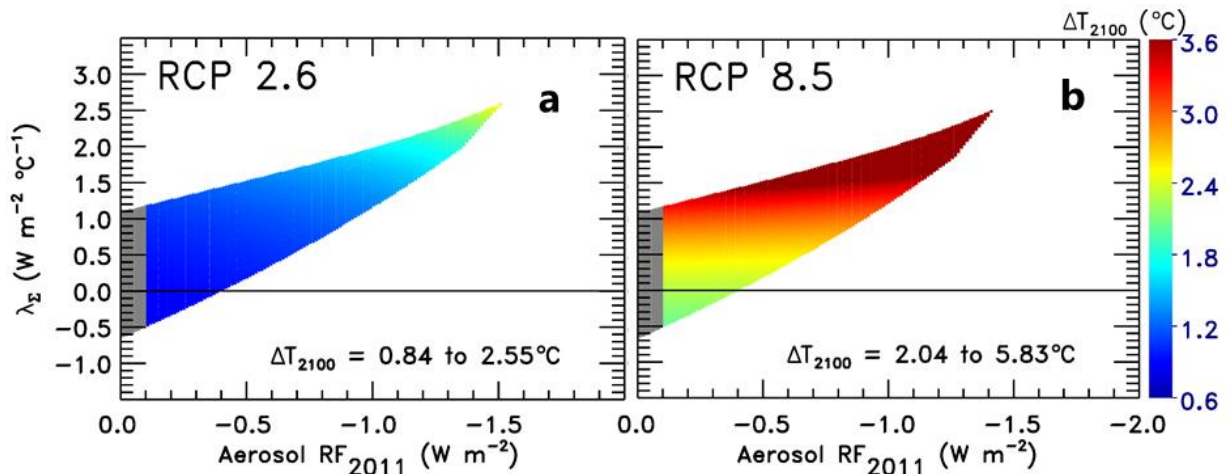
1380 Figure 10c and 10d also compare ΔT_{2100} from the EM-GC to temperatures at the end of
1381 the century presented in Sherwood et al. (2020). The probabilistic estimate of end of century
1382 warming given in Sherwood et al. (2020) is based upon their expert evaluation of climate
1383 sensitivity combined with the assumption of a linear relation between the transient climate
1384 response and radiative forcing. They estimate that by end of century warming will be less than
1385 2°C relative to pre-industrial are 83%, 17%, and 0% for RCP 2.6, 4.5, and 8.5, respectively. The
1386 probabilistic estimate of the upper end of warming given by Sherwood et al. (2020) is
1387 considerably less than indicated by the CMIP5 GCMs (green versus red lines in Fig. 10). They

1388 also compute a lower probability for the low end of the distribution of ΔT_{2100} than we find using
1389 our EM-GC, which is traceable to their judgement that the most likely value of total cloud
1390 feedback is positive (Klein et al., 2017).

1391 There are three clear takeaways from Figures 5b and 10. First, earth's climate allows for
1392 a wide range of future temperatures, even when a model such as our EM-GC is sufficiently
1393 trained with historical data due to uncertainty in quantities such as AER RF_{2011} . Second,
1394 consistent with the expert assessment of temperature projections from CMIP5 GCMs given in
1395 Chapter 11 of AR5 (Kirtman et al., 2013), our EM-GC projects smaller future increases in ΔT
1396 than provided by most of the CMIP5 GCMs. Third, while temperature projections from our EM-
1397 GC agree with CMIP5 GCM results in that society must avoid a GHG pathway consistent with
1398 RCP 8.5 to achieve the goals of the Paris Climate Agreement, our model simulations show that
1399 RCP 4.5 and particularly RCP 2.6 are GHG pathways more likely to achieve limited warming
1400 than indicated by GCM results within the CMIP5 archive. Our model projections suggest that
1401 adhering to the RCP 4.5 pathway is as likely as not (=50%) to give Earth a future that limits
1402 global warming to 2°C above preindustrial; placing GHGs on the RCP 2.6 pathway is highly
1403 likely (>90%) to limit global warming to 2°C and likely (>66.7%) to stay beneath 1.5°C.

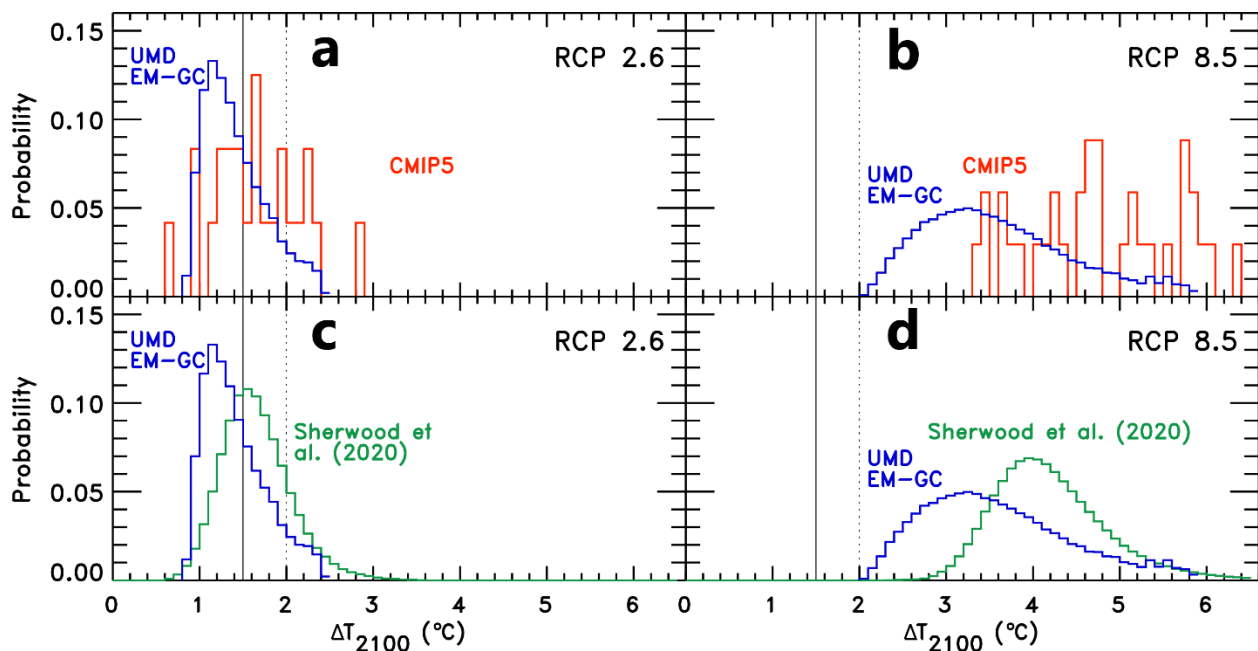
1404 Our probabilistic temperature projections disagree somewhat with AR5. According to
1405 CMIP5 GCM results as presented in AR5, RCP 2.6 is likely but not highly likely (that is,
1406 >66.7% but not >90%) to keep global temperatures beneath 2°C. AR5 also says RCP 4.5 is more
1407 likely than not (>50%) to *exceed* 2°C. The power of RCP 2.6 to keep us beneath 2°C of warming
1408 appeared in another recent study (Goodwin et al. 2018) that determined staying beneath 2°C to
1409 be highly likely, much closer to our result than to those of CMIP5.

1410

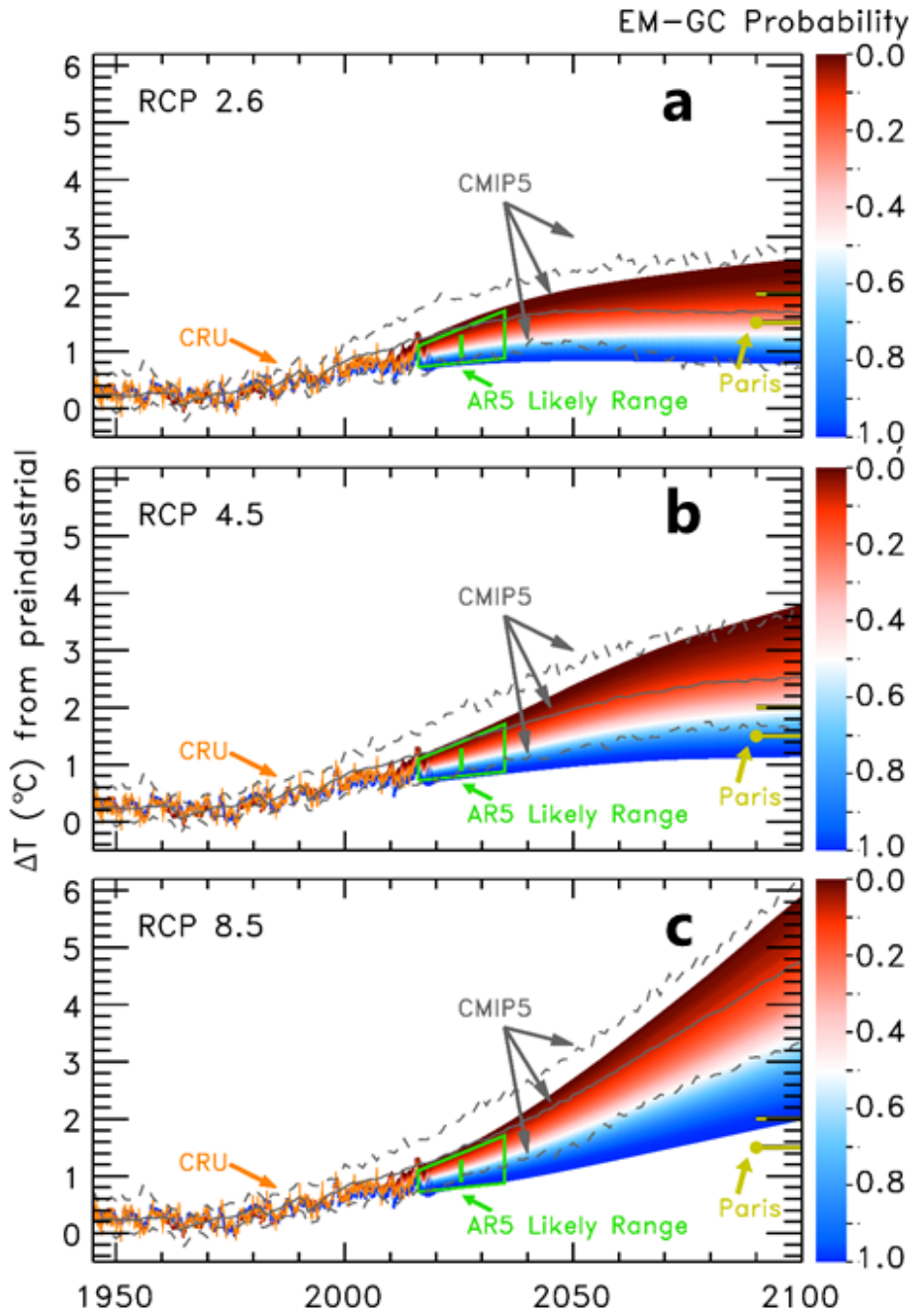


1411
 1412 **Figure 9.** Same as Figure 4a except for ensembles using RCP 2.6 and RCP 8.5 anthropogenic
 1413 forcing instead of RCP 4.5.

1414
 1415



1416
 1417 **Figure 10.** Panels a and b are the same as Figure 5a except for ensembles using RCP 2.6 and
 1418 RCP 8.5 anthropogenic forcing instead of RCP 4.5. Panels c and d then exchange CMIP5 data
 1419 for data taken from figure 23 of Sherwood et al. (2020), binned to match the structure presented
 1420 in the previous PDFs of this study.



1421

1422

1423 **Figure 11.** Global warming projections for RCP 2.6, RCP 4.5, and RCP 8.5 relative to the
 1424 preindustrial baseline. Figure 11b is the same as Figure 8; all three panels are of similar
 1425 construction. Color at any given point within the EM-GC envelope represents the chance of ΔT
 1426 reaching at least that temperature at that time.

1427

1428 **Figure 11** shows probabilistic projections of global warming for RCP 2.6, 4.5, and 8.5.
1429 This figure is the same as Figure 8 (that showed results for RCP 4.5), using the same vertical axis
1430 for all three ensembles. This figure demonstrates a fourth key takeaway from our modeled
1431 projections of future temperature. Projections of global warming computed using our EM-GC
1432 agree well with the expert judgement of near-future ΔT from AR5 of Chapter 11 (Kirtman et al.,
1433 2013), shown as a trapezoid on each panel of Figure 11. The colored envelope for each panel of
1434 Figure 11 is based upon a representative sample of the runs from each respective RCP ensemble
1435 (Figure 4b and Figure 9) and displays the rise in ΔT out to the end of the century. At each time
1436 along this envelope, the color represents the probability within the ensemble of reaching at least
1437 that temperature. Whatever RCP scenario we examine, the EM-GC results match the near-future
1438 projections (trapezoid) based on the expert judgement of AR5's Chapter 11 authors. Our
1439 projections of warming using a physically based model tied to observations of ocean heat
1440 content, natural as well as anthropogenic drivers of variations in ΔT , and the consideration of
1441 uncertainty in AER RF are thus remarkably similar to the expert assessment of the CMIP5-
1442 GCM-based future rise in ΔT sketched out in figure 11.25b of AR5 (Kirtman et al., 2013).

1443

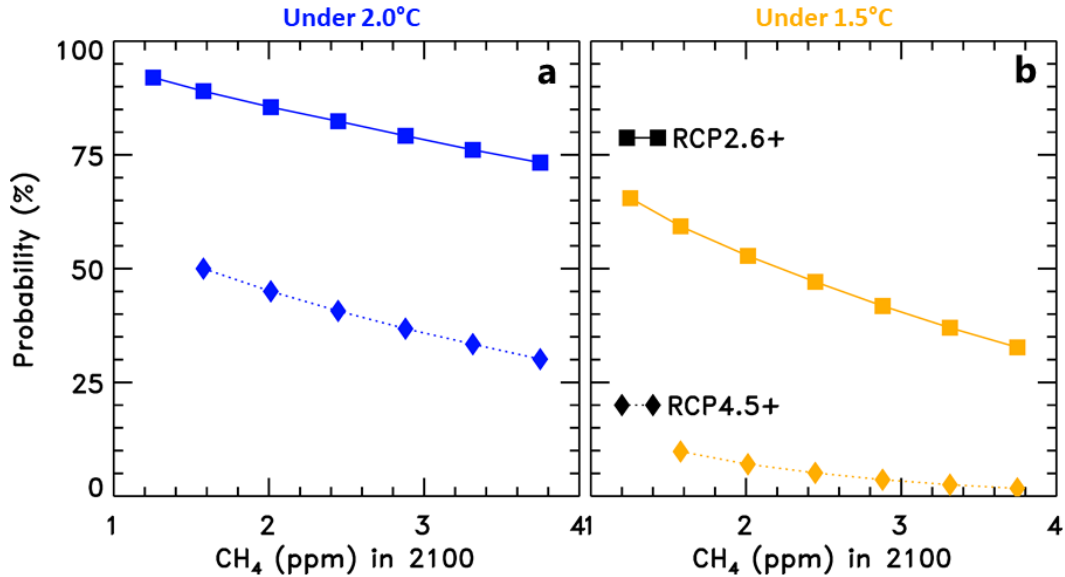
1444 3.6 The effect of increased future emissions of CH₄

1445 As many countries around the world transition from coal to natural gas as a primary fossil
1446 fuel for electricity production, assumptions about future methane scenarios must shift to account
1447 for faster growth (Molnár, 2018; Saunio et al., 2020). The RCP 4.5 scenario has future CH₄
1448 leveling off by midcentury at near-current atmospheric mixing ratios, then decreasing until the
1449 end of the 21st century (Figure 1b). The RCP 2.6 scenario has even more drastic and immediate
1450 reductions in atmospheric CH₄. This leveling off may be difficult for society to achieve due to
1451 natural gas becoming a primary source of energy for the foreseeable future (Jackson et al., 2018).
1452 This energy shift would imply more leakage of CH₄ from utility infrastructure as demand
1453 increases (Saunio et al., 2020). The atmospheric mixing ratio might also rise through
1454 anthropogenically-induced releases of natural CH₄ reservoirs, such as permafrost melting, or
1455 increased biogenic activity (Comyn-Platt et al., 2018; Voigt et al., 2017). Finally, the observed
1456 abundance of atmospheric CH₄ has already been rising faster in the past few years than in the
1457 previous two decades (Nisbet et al., 2019; Saunio et al., 2020), exceeding the RCP 4.5

1458 projection and mapping closer to the most intense RCP 8.5 scenario. These factors taken together
1459 suggest that we should expect that the abundance of CH₄ in the atmosphere may increase over
1460 time, and not level off as suggested in the RCP 4.5 scenario (Saunois et al., 2016). Therefore, we
1461 have created blended CH₄ scenarios, noted in section §2.1.2 and shown in Figure S2, to test the
1462 sensitivity of warming computed using our EM-GC to various future for atmospheric CH₄.

1463 **Figure 12** shows the probability of achieving the Paris Climate Agreement goals as a
1464 function of the atmospheric abundance of CH₄ in 2100. Each symbol in Figure 12 shows ΔT_{2100}
1465 for an ensemble of EM-GC runs where the only change between the ensembles is the input time
1466 series of CH₄. Starting from either the RCP 2.6 (squares) and RCP 4.5 (diamonds) as scenario for
1467 all GHGs other than CH₄, the time series for each ensemble calculation is based upon either RCP
1468 2.6, RCP 4.5, RCP 8.5, or one of four linear combinations of CH₄ versus time between RCP4.5
1469 and RCP 8.5 shown in Figure S2. Otherwise the ensembles are identical to those in Figs. 10a and
1470 10b for RCP 2.6 and RCP 4.5 respectively. In RCP 4.5, the abundance of CH₄ in 2100 is 1578
1471 ppb; in the ensemble driven by RCP 4.5 with no changes to CH₄, we compute a 50% probability
1472 of ΔT_{2100} remaining beneath 2°C and a 10% chance of remaining beneath 1.5°C. These
1473 probabilities correspond to the leftmost diamonds in each panel of Figure 12. As the CH₄ time
1474 series approaches the RCP 8.5 pathway, which has a CH₄ mixing ratio of 3748 ppb in 2100, the
1475 probabilities of future warming remaining beneath 2°C and 1.5°C fall to 30% and 2%,
1476 respectively (rightmost diamonds). Similarly, switching from RCP 2.6 for all GHGs to a
1477 combined scenario that uses CH₄ from RCP 8.5 causes the probability of ΔT_{2100} staying below
1478 2°C to decrease from 92% to 73% and the likelihood of staying below 1.5°C warming to
1479 decrease from 66% to 33% (left- and rightmost squares). This analysis indicates that failure to
1480 limit methane to the RCP 2.6 trajectory will have a large impact on the achievement of the 1.5°C
1481 goal of the Paris Climate Agreement.

1482



1483
 1484 **Figure 12.** Impact of CH₄ on EM-GC projections. Shown are the probabilities that ΔT_{2100}
 1485 remains below 2°C (11a, blue) or below 1.5°C (11b, gold) for both the RCP 2.6-based ensembles
 1486 (squares, solid lines) and RCP 4.5-based ensembles (diamonds, dashed lines) relative to
 1487 preindustrial. Each ensemble based on RCP 4.5 uses all GHG and aerosol forcing inputs from
 1488 RCP 4.5 except replacing the RCP 4.5 CH₄ time series with one of six linear combinations
 1489 between the RCP 4.5 CH₄ scenario and the RCP 8.5 CH₄ scenario, inclusive. Likewise, each
 1490 ensemble based on RCP 2.6 uses all forcing inputs from RCP 2.6 except substituting the RCP 2.6
 1491 CH₄ with one of the six linear combinations (save for the seventh ensemble, far left, which is
 1492 purely RCP 2.6). Ensembles are placed in this figure based on the CH₄ mixing ratio in 2100 (i.e.
 1493 end values of Figure S2).

1494
 1495 3.7 Response to cumulative emissions

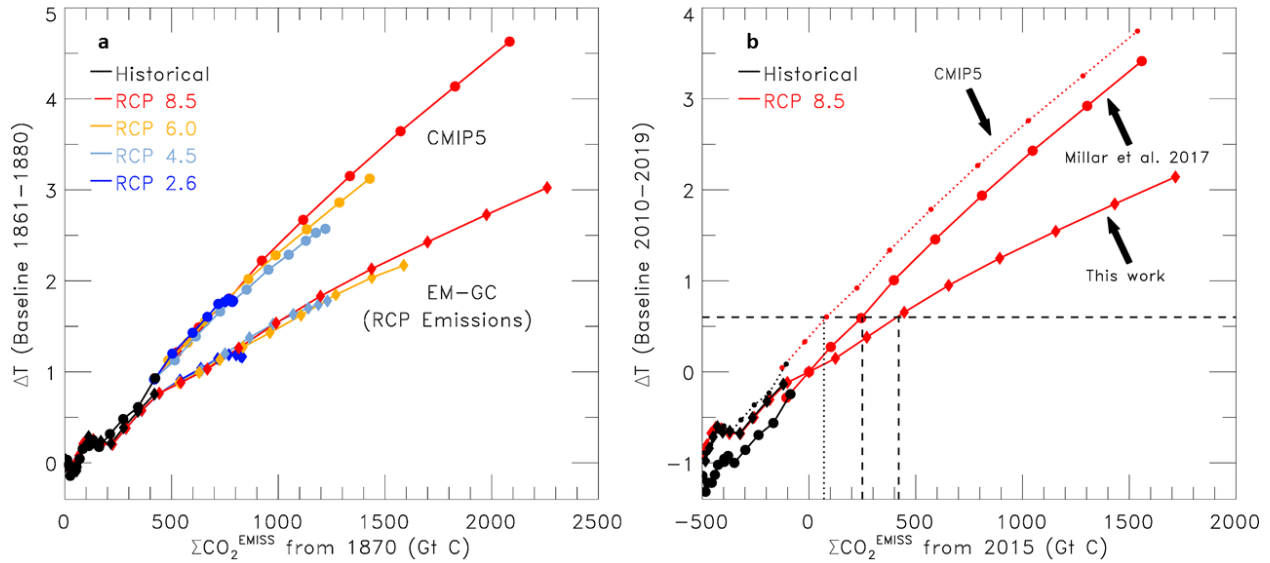
1496 The Transient Climate Response to cumulative carbon Emissions (TCRE), which relates
 1497 ΔT to accumulated anthropogenic emissions of CO₂, is an important policy metric (Gregory et
 1498 al., 2009; Millar et al., 2017). As the EM-GC projects generally less future warming than most of
 1499 the CMIP5 GCMs, it follows that TCRE derived from the EM-GC falls on the low side of the
 1500 range for TCRE given in AR5 (0.8 to 2.5°C per 1,000 GtC). **Figure 13a** shows the results of the
 1501 ensemble median EM-GC simulations for the four RCP pathways. All four EM-GC ensemble
 1502 medians suggest a TCRE of roughly 1.4°C per 1,000 GtC. The other four lines on Figure 13a
 1503 show the multi-model mean projections from the CMIP5 GCMs for the four RCP scenarios,

1504 taken from figure SPM.10 of AR5. TCRE from the CMIP5 GCMs in this figure has a value of
1505 2.3°C per 1,000 GtC, which lies well above the EM-GC estimate and in the high end of the
1506 assessed range given by AR5. Following AR5 and Millar et al. (2017), future cumulative
1507 emissions of CO₂ in figure 13a are based on the rise since 1870, with ΔT shown relative to the
1508 two-decade average for 1861-1880. The emissions along the horizontal axis represent global,
1509 atmospheric release of CO₂ due to combustion of fossil fuels, flaring, cement production, and
1510 LUC from the RCP database.

1511 **Figure 13b** shows an adjustment of the RCP 8.5 lines from Figure 13a that are set to zero
1512 for the most recent decade (2010 to 2019), as done in Millar et al. (2017). This adjustment
1513 clarifies the allowable remaining carbon budget for limiting future warming to remain beneath a
1514 given amount. Millar et al. (2017) presented this adjustment as one manner of accounting for the
1515 overestimate of ΔT_{MDL} provided by CMIP5 GCMs compared to ΔT_{OBS}; setting the ΔT baseline
1516 to recent years is also the process behind the expert judgement of Kirtman et al. (2013) that
1517 produced the AR5-based trapezoid shown in previous figures. The central finding of Millar et al.
1518 (2017) is that the best estimate of the remaining carbon budget needed to limit future warming to
1519 0.6°C relative to 2015 (which translates to 1.5°C relative to preindustrial) is higher than the best
1520 estimate suggested by AR5. They later issued a public clarification saying their estimate for
1521 future temperature (and thus their carbon budget) still lies within the AR5 uncertainty (Allen &
1522 Millar, 2017), albeit with their carbon budget on the high extreme of the AR5 range. As shown in
1523 Figure 13 and further discussed below, our EM-GC projection of ΔT_{MDL} indicates the remaining
1524 carbon budget is even larger than the values given by AR5 and Millar et al. (2017).

1525 We can also use full ensemble simulations within the EM-GC to compute probabilistic
1526 forecasts of emissions thresholds for the Paris Agreement targets. **Figure 14** displays ΔT with
1527 respect to cumulative emissions of CO₂, using the same color scheme adopted for Figures 8 and
1528 11. The colors represent the probability that a particular future value of ΔT will reach at least
1529 that temperature for the specified cumulative emission of CO₂. Figure 14 is based on the RCP 8.5
1530 scenario for GHGs, to cover the widest range of future anthropogenic emissions of CO₂.

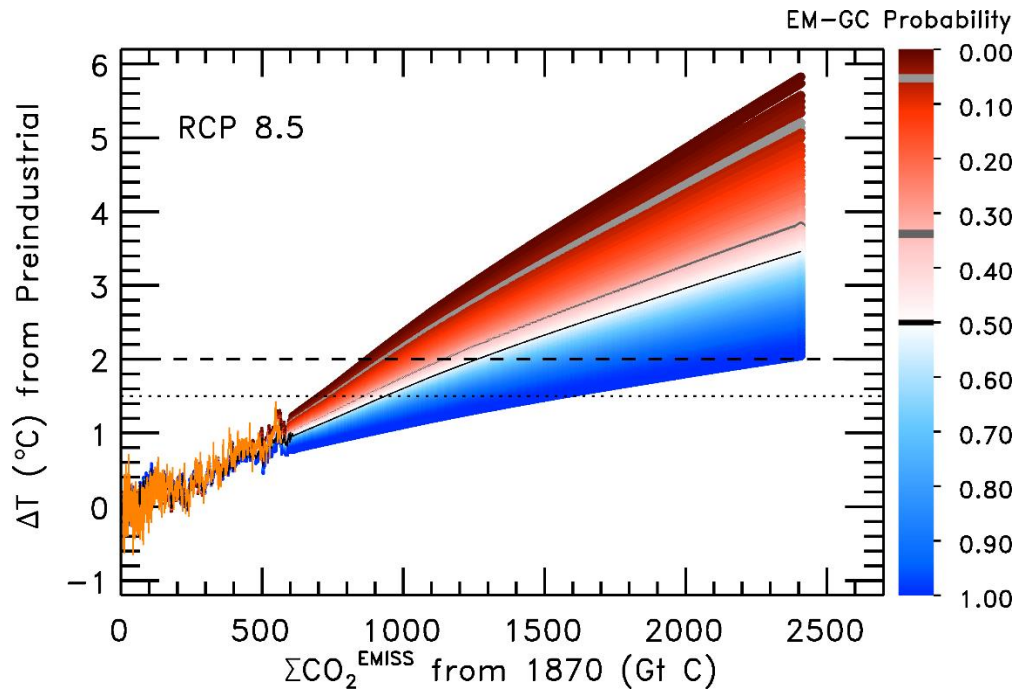
1531



1532

1533 **Figure 13. (a)** Transient climate response to cumulative CO₂ emissions, in units of GtC. Average
 1534 ΔT from CMIP5 GCMs, as taken from figure SPM.10 of AR5, is plotted against the average
 1535 cumulative emissions since 1870 modeled to meet RCP prescribed concentrations (circles). EM-
 1536 GC results show ΔT from a single EM-GC simulation for each RCP scenario representing the
 1537 median of the ensemble; CO₂ emissions for each RCP ensemble are taken directly from the RCP
 1538 database. **(b)** TCRE for different studies of RCP 8.5, illustrated using the same axes as Millar et
 1539 al. (2017). Both the EM-GC projection and the Millar et al. (2017) projection from CMIP5 are
 1540 plotted such that the point representing the decade of the 2010s (centered on 2015) is set to the
 1541 origin, based on current ΔT and estimated cumulative emission to date. For comparison, the
 1542 CMIP5 projection is also shown such that it matches the EM-GC results for roughly the first
 1543 century of the simulation, as done in panel a, i.e. instead of matching in the 2010s, so as to
 1544 demonstrate the effective shift that Millar et al. (2017) applied to the CMIP5 projection. Vertical
 1545 dotted and dashed lines indicate the remaining amount of CO₂ that can be released prior to
 1546 having ΔT rise 1.5°C above preindustrial (i.e., 0.6°C above the observed 0.9°C rise in ΔT for the
 1547 2010s) according to the three studies.

1548



1549
 1550 **Figure 14.** Full EM-GC projection of transient climate response to cumulative CO₂ emissions for
 1551 RCP 8.5. Colors and structure mirror those of figure 11c. The three grey lines of varying
 1552 darkness provide a visual guide to highlight the lines of 50%, 66%, and 95% probability for
 1553 keeping temperatures cooler than those temperatures, while the black horizontal lines are a visual
 1554 guide to the two Paris Climate Agreement target ΔT values. As such, the intersection of a grey
 1555 line with a black line determines the maximum amount of cumulative emissions that would be
 1556 allowed while remaining cooler than one of the Paris Climate Agreement targets with the given
 1557 probability.

1558
 1559 Figure 14 shows that according to calculations conducted in our model framework, if
 1560 society can keep cumulative carbon emissions below 900 GtC, then we will have a 95% chance
 1561 of preventing global warming from exceeding 2°C relative to preindustrial. Cumulative
 1562 emissions of 1140 GtC or 1250 GtC would lower the chance of ΔT remaining below 2°C to 66%
 1563 or 50%, respectively. Likewise, the 95%, 66%, or 50% probabilities for ΔT remaining below
 1564 1.5°C correspond to cumulative CO₂ emissions of 710 GtC, 850 GtC, or 930 GtC, respectively.
 1565 For comparison, these emission numbers are listed in **Table 1**, alongside comparable numbers
 1566 from other studies (Goodwin et al., 2018; Millar et al., 2017; Tokarska & Gillett, 2018). Similar
 1567 quantities from Chapter 2 of the IPCC 1.5 C Special Report are also included, and show lower

1568 allowable carbon emission budgets driven by two intermediate-complexity climate models,
1569 FAIR and MAGICC, that are constrained to approximate climate sensitivity from the CMIP5
1570 GCMs (Rogelj et al., 2018).

1571 For reference, while Millar et al. (2017) suggest that human activity has emitted roughly
1572 545 GtC from 1870 to 2014, leading to a rise in ΔT of 0.9 °C for that time (Millar et al., 2017).
1573 Improvements in the understanding of LUC emission and five more years of emitting CO₂
1574 suggest these values increase to 635 GtC (Friedlingstein et al., 2019; Le Quéré et al., 2018) and
1575 1.0 °C respectively for 1870 to 2019. Using only emissions prescribed by the RCP scenarios, the
1576 carbon budget values are 532 GtC to 2014 and 590 GtC to 2019, but similar to the 545 GtC value
1577 from Millar et al. (2017), these numbers do not reflect updated understanding of past emissions
1578 from LUC. Society has been emitting 11.0 ± 0.8 GtC per year over the past decade, a rate that
1579 has also been increasing over previous decades, with a current annual value of nearly 12 GtC per
1580 year (Friedlingstein et al., 2019).

1581 **Table 2** shows the remaining, post end of 2019 carbon budget for limiting warming to
1582 either 1.5°C or 2.0°C in our model framework. For all entries in Table 2 we assume at the end of
1583 2019 that cumulative carbon emissions are 590 GtC. We tie this cumulative carbon emission
1584 estimate to the time series used to drive the global carbon cycle model that underlies the RCP 8.5
1585 specification of atmosphere CO₂. The current annual rate of global carbon emission of nearly 12
1586 GtC would imply surpassing 710 GtC, our RCP-based threshold for staying below 1.5 °C with
1587 95% confidence, in 2029 and surpassing the 2.0 °C, 95% confidence threshold of 900 GtC in
1588 2045. These dates of passing the 95% confidence intervals for the target and upper limit of the
1589 Paris Agreement fall to 2028 and 2040, respectively, if we allow total carbon emissions to rise at
1590 the rate that underlies RCP 8.5. Similarly, year ranges for passing the 66% confidence interval
1591 for 1.5°C and 2.0°C warming are 2037-2041 and 2052-2065, respectively (Table 2). The 50%
1592 confidence interval estimates for these thresholds rise to 2042-2048 and 2057-2074. We
1593 emphasize that even though our EM-GC exhibits slower warming than the CMIP5 GCMs, the
1594 Paris Climate Agreement target of limiting warming to 1.5°C cannot be achieved unless society
1595 begins a near immediate transition to a low carbon future, and at the same time slows or
1596 eliminates the rise in atmospheric CH₄ (section §3.6).

1597

1598 **Table 1**

1599 *Carbon Budget Comparisons*

Source & reference emissions	Threshold Budget for 1.5°C			Threshold Budget for 2.0°C		
	50% prob.	65% prob.	90/95% prob.	50% prob.	65% prob.	90/95% prob.
Millar et al. (2017) - 545 GtC, 2014	768 GtC	749 GtC	709 GtC (90%)	961 GtC	940 GtC	875 GtC (90%)
Tokarsak & Gillet (2018) - 555 GtC, 2015	763 GtC	685 GtC	*	*	*	*
Rogelj et al. (2018) – 605 GtC 2017	158 GtC	114 GtC	*	*	*	*
Goodwin et al. (2018) - 572 GtC, 2016	*	767-777 GtC	*	*	967-1027 GtC	*
This study - 532 GtC, 2014 ; 590 GtC, 2019	930 GtC	850 GtC	710 GtC (95%)	1250 GtC	1140 GtC	900 GtC (95%)

1600

1601 **Table 2**

1602 *Metrics for Future Carbon Budgets Leading to Crossing the Pairs Thresholds*

Warming Targets		Future Budget to Threshold Budget ^a	Future Budget as % of Past Budget ^a	Range of Years to Meet Threshold Budget ^b
1.5 °C	95%	120 GtC	20%	2028-2029
	66%	260 GtC	44%	2037-2041
	50%	340 GtC	58%	2042-2048
2.0 °C	95%	310 GtC	53%	2040-2045
	66%	550 GtC	93%	2052-2065
	50%	660 GtC	112%	2057-2074

1603 ^aFuture Budget = Threshold Budget – Past Budget, with threshold and past budgets taken from the final row of Table 1 (2019 reference year)

1604 ^bFirst year of range is taken from RCP 8.5 prescribed emissions; last year of range assumes the current rate of emissions of roughly 12GtC
 1605 continues into the future

1606

1607 **4. Conclusions**

1608 The value of the anthropogenic contribution to global warming over the past three three
 1609 decades, termed attributable anthropogenic warming rate (AAWR), has been analyzed in detail
 1610 using both an empirical model of global climate (EM-GC) and output from CMIP5 GCMs. We
 1611 find AAWR to be as 0.14 ± 0.06 °C/decade (full range of possible values) for 1979 to 2010 using
 1612 our EM-GC, where the uncertainty covers the full range of model runs that yield a good fit to
 1613 ΔT_{OBS} from CRU4. The CMIP5 GCMs exhibit values of AAWR of 0.22 ± 0.10 °C/decade
 1614 (standard deviation among AAWR values from the CMIP5 GCMs), considerably larger than
 1615 inferred from the climate record using our EM-GC. More than two-thirds of the 112 archived
 1616 CMIP5 GCM runs exhibit a value for AAWR larger than our upper limit of 0.20 °C/decade. The
 1617 uncertainty in the EM-GC based derivation of AAWR is driven by imprecise knowledge of the
 1618 radiative forcing of climate due to tropospheric aerosols, whereas the largest source of spread in

1619 the GCM simulation of GMST is due to uncertainty in cloud feedback (Ceppi et al., 2017; Vial
1620 et al., 2013; Zelinka et al., 2016). Our finding that the CMIP5 GCMs exhibit a considerably
1621 faster rise in GMST than observed is consistent with finding of Chapter 11 of AR5 (Kirtman et
1622 al., 2013). Attempts to improve the understanding of aerosol species is an active area of current
1623 research, but large uncertainties persist (Bond et al., 2013; Collins et al., 2017; Pincus et al.,
1624 2016; Shen et al., 2020; Smith et al., 2011; Smith & Bond, 2014; Thornhill et al., 2020).
1625 Similarly, while some recent studies suggest total cloud feedback is positive (Klein et al., 2017;
1626 Sherwood et al., 2020), a recent analysis of a 40 year satellite record shows no trend in cloud
1627 reflectivity (Weaver et al., 2020), which is thought to be the largest driver of this positive trend.

1628 While it is beyond the scope of this study to thoroughly assess the possible shortcomings
1629 of the CMIP5 GCM simulations over the past three decades, we suggest that high values for the
1630 sum of climate feedback mechanisms (λ_{Σ}), in particular the various cloud feedback processes,
1631 could be responsible for the apparent warm bias of the CMIP5 GCMs. Indeed, a recent analysis
1632 of CMIP6 shows that the next generation of GCMs displays high correlation between high ECS
1633 (i.e. high λ_{Σ} in the EM-GC) and a poor fit to observed AAWR from 1981 to 2014/17 (Tokarska
1634 et al., 2020), and these high-ECS models have strongly positive cloud feedbacks (Zelinka et al.,
1635 2020). If the actual cloud feedback is less positive than currently exhibited by CMIP5 and
1636 CMIP6 GCMs, this could explain the apparent warm bias of these models.

1637 Accurate projections of ΔT are critical to the successful implementation of the Paris
1638 Agreement. However, the wide span of possible futures even in our EM-GC framework
1639 confounds policy-making efforts and confidence in achieving the desired warming limits. While
1640 our model projections show a wide range of possible warming by end of century for the same
1641 GHG scenario, our forecasts produce a more optimistic likelihood for achieving the goals of the
1642 Paris Agreement than is provided by the CMIP5 GCMs. The temperature forecasts given by our
1643 EM-GC tend to lie among the lower half of the projections provided by the CMIP5 GCMs, with
1644 our maximum forecast warming tending to lie near the CMIP5 multi-model mean. Most
1645 importantly, the projections of ΔT from our EM-GC agree extremely well with the “indicative
1646 likely range for annual mean ΔT ” from Chapter 11 of AR5 (Kirtman et al., 2013) – lending
1647 important computational support for this expert assessment of the CMIP5 GCMs driven by the
1648 fact many of the GCM-based values of ΔT have exceeded ΔT_{OBS} over the past few decades
1649 (Figure 2 here and figure 11.25b of Kirtman et al. (2013)).

1650 Projections of ΔT versus cumulative emissions provides a policy relevant framework for
1651 achieving the goals of the Paris Climate Agreement. From 1870 to date, humans have emitted
1652 roughly 600 GtC, and are currently emitting nearly 12 GtC per year. If society is to achieve the
1653 Paris Agreement by keeping the rise in ΔT below 2°C with 95% probability by 2100, then only
1654 20 to 25 years of cumulative carbon emissions remain in the allowable budget (Table 2).
1655 However, in reality society has less than 20 to 25 years when considering practical
1656 complications. Since it is unreasonable to assume that annual emissions can drop from 12 GtC to
1657 zero instantaneously, the reduction in emission rate must begin earlier to reach the same
1658 cumulative emissions total. While the 20 to 25 year limit found in our model framework suggests
1659 society has more time to act than indicated by the CMIP5 GCMs, we emphasize that the goal of
1660 the Paris Climate Agreement can only be achieved by near immediate reductions in global
1661 carbon emissions.

1662 Methane, a potent GHG, also needs to be a large part of policy considerations when
1663 considering how cumulative emissions compare to global warming projections. As the United
1664 States and other major coal-burning nations switch to natural gas, the risk of significant CH_4
1665 leakage into the atmosphere increases, potentially negating the climate benefit of switching to the
1666 less carbon intensive fossil fuel source (Jackson et al., 2018; Saunio et al., 2020). Carbon cycle
1667 feedbacks, such as higher activity in natural or agricultural wetland methane production or
1668 leakage from previously locked natural reservoirs, could further increase the atmospheric
1669 abundance of CH_4 (Comyn-Platt et al., 2018; Voigt et al., 2017). It is probably not reasonable to
1670 expect CH_4 to follow the peak-and-decline component pattern of RCP 4.5; on the other hand, the
1671 aggressive methane growth of RCP 8.5 also seems unreasonable (Figure 1). A projection of
1672 methane mid-range between RCP 4.5 and RCP 8.5 is perhaps a more likely scenario, implying a
1673 value for atmospheric methane between 2 and 3 ppm by 2100. Placing all GHGs other than
1674 methane along the RCP 2.6 trajectory would place us on a trajectory for having a reasonably
1675 favorable probability of limiting warming to 2°C , irrespective of the future methane scenario
1676 (Figure 12). However, even for RCP 2.6, achievement of the ambitious Paris Climate Agreement
1677 target of 1.5°C drops noticeably as future atmospheric methane intensifies. Quite simply,
1678 limiting warming to 1.5°C will require aggressive future controls on atmospheric release of both
1679 CO_2 and CH_4 .

1680

1681 **Appendix A: Input data sources**

1682

1683 **Table A1.**

1684 *Natural Factor Input Sources*

Variable	Data Name	Years	Location
SAOD	CMIP6	1850-2014	https://esgf-node.llnl.gov/search/input4mips/
	GloSSACv2	1979-2018	https://opendap.larc.nasa.gov/opendap/GloSSAC/contents.html
	CALIPSO	2019	https://opendap.larc.nasa.gov/opendap/CALIPSO/contents.html
TSI	CMIP6	1850-2014	https://esgf-node.llnl.gov/search/input4mips/
	SORCE	2003-2019	https://lasp.colorado.edu/home/sorce/data/tsi-data/
ENSO ^a	MEIv2	1979-2019	https://psl.noaa.gov/enso/mei/data/meiv2.data
	MEI-ext	1871-2005	https://psl.noaa.gov/enso/mei.ext/table.ext.html
AMOC ^b	AMV	1850-2019	https://crudata.uea.ac.uk/cru/data/temperature/HadSST.3.1.1.0.median.nc
PDO		1900-2018	http://research.jisao.washington.edu/pdo/PDO.latest.txt
IOD		1870-2019	http://www.jamstec.go.jp/frgcr/research/d1/iod/iod/dipole_mode_index.html
		1850-1870	http://www.jamstec.go.jp/frgcr/research/d1/iod/kaplan_sst_dmi_new.txt

1685 ^a1850-1870 ENSO constructed as an area SST average over the Nino3.4 region using

1686 <https://crudata.uea.ac.uk/cru/data/temperature/HadSST.3.1.1.0.median.nc>

1687 ^bAMV calculated as an area average of Atlantic SSTs; multiple detrending and Fourier filtering options can be applied

1688

1689 **Table A2.**

1690 *Anthropogenic Factor Input Sources*

Variable	Data Name	Years	Location
GHG RF	RCPs	1850-2099	http://www.pik-potsdam.de/~mmalte/rcps/
AER RF ^c	Sulfates	1850-2005	http://www.sterndavidi.com/datasite.html http://ciera-air.org/sites/default/files/Total_SO2.xls
	Levitus	1955-2019	http://data.nodc.noaa.gov/woa/DATA_ANALYSIS/3M_HEAT_CONTENT/DATA/basin/yearly/h22-w0-700m.dat
OHC	Balmaseda	1958-2017	http://www.cgd.ucar.edu/cas/catalog/ocean/OHC700m.tar.gz
	Cheng	1955-2019	http://159.226.119.60/cheng/
	Ishii	1955-2017	http://159.226.119.60/cheng/
	Carton	1982-2017	https://www.atmos.umd.edu/~ocean/index_files/soda3_readme.htm

1691 ^cThe six time series of AER RF for each of the six types of aerosol species considered were combined as described in section §2.1.2

1692

1693 **Appendix B: Model Input & Output Databases**

1694

1695 All EM-GC input files (for natural and anthropogenic forcings) are available at

1696 <http://dsrs.atmos.umd.edu/DATA/EMGCv4/INPUTS/> . Included are fifteen sample total AER

1697 RF time series.

1698
1699 All ΔT_{OBS} and OHC_{OBS} fitting files are available at
1700 <http://dsrs.atmos.umd.edu/DATA/EMGCv4/OBS/> .

1701
1702 Original ΔT_{OBS} data was downloaded from the following sites:
1703 CRU – <https://www.metoffice.gov.uk/hadobs/hadcrut4/data/current/download.html>
1704 NCEI – <https://www.ncdc.noaa.gov/cag/global/time-series>
1705 GISS – <https://data.giss.nasa.gov/gistemp/>
1706 BEG – <http://berkeleyearth.org/data-new/>

1707
1708 CMIP5 model output is available at <https://esgf-node.llnl.gov/search/esgf-llnl/> . All CMIP5
1709 atmospheric temperature data were downloaded over several months in 2013 and 2014, and all
1710 CMIP5 ocean data were downloaded in early 2017.

1711
1712 **Author contributions and other acknowledgements**

1713
1714 TPC, APH, and LAM developed the model code used in this analysis; APH, LAM, and BFB
1715 collected data; RJS and TPC supervised, administrated, and developed the project; APH wrote
1716 the original draft; LAM, BFB, WRT, TPC, and RJS participated in the review and editing of the
1717 manuscript.

1718
1719 We acknowledge the World Climate Research Programme’s Working Group on Coupled
1720 Modelling, which is responsible for CMIP, and we thank the climate modeling groups (listed in
1721 Table S4 of this paper) for producing and making available their model output. For CMIP the
1722 U.S. Department of Energy’s Program for Climate Model Diagnosis and Intercomparison
1723 provides coordinating support and led development of software infrastructure in partnership with
1724 the Global Organization for Earth System Science Portals.

1725
1726 We appreciate financial support for this work from the NASA Climate Indicators and Data
1727 Products for Future National Climate Assessments (INCA) program (award NNX16AG34G) as
1728 well as the NOAA Cooperative Institute for Climate and Satellites (award WAIVER5278050)

1729

1730 **References**

- 1731 Allen, M., & Millar, R. (2017, September 20). *Clarification on recent press coverage of our '1.5 degrees'*
1732 *paper in Nature Geoscience*. Oxford Martin School. Retrieved December 1 from
1733 <https://www.oxfordmartin.ox.ac.uk/opinion/view/379>
- 1734 Andrews, T., Gregory, J., Webb, M., & Taylor, K. (2012). Forcing, feedbacks and climate sensitivity in
1735 CMIP5 coupled atmosphere-ocean climate models [Article]. *Geophysical Research Letters*, 39,
1736 Article ARTN L09712. <https://doi.org/10.1029/2012GL051607>
- 1737 Andronova, N., & Schlesinger, M. (2000). Causes of global temperature changes during the 19th and 20th
1738 centuries [Article]. *Geophysical Research Letters*, 27(14), 2137-2140.
1739 <https://doi.org/10.1029/2000GL006109>
- 1740 Arfeuille, F., Weisenstein, D., Mack, H., Rozanov, E., Peter, T., & Brönnimann, S. (2014). Volcanic
1741 forcing for climate modeling: a new microphysics-based data set covering years 1600–present.
1742 *Climate of the Past*, 10(1), 359-375.
- 1743 Balmaseda, M., Trenberth, K., & Kallen, E. (2013). Distinctive climate signals in reanalysis of global
1744 ocean heat content [Article]. *Geophysical Research Letters*, 40(9), 1754-1759.
1745 <https://doi.org/10.1002/grl.50382>
- 1746 Belcher, S., Boucher, O., & Sutton, R. (2019). Why results from the next generation of climate models
1747 matter. *Carbon Brief*.
- 1748 Boessenkool, K. P., Hall, I. R., Elderfield, H., & Yashayaev, I. (2007). North Atlantic climate and deep-
1749 ocean flow speed changes during the last 230 years. *Geophysical Research Letters*, 34(13).
- 1750 Bond, T., Doherty, S., Fahey, D., Forster, P., Berntsen, T., DeAngelo, B., Flanner, M., Ghan, S., Karcher,
1751 B., Koch, D., Kinne, S., Kondo, Y., Quinn, P., Sarofim, M., Schultz, M., Schulz, M.,
1752 Venkataraman, C., Zhang, H., Zhang, S., Bellouin, N., Guttikunda, S., Hopke, P., Jacobson, M.,
1753 Kaiser, J., Klimont, Z., Lohmann, U., Schwarz, J., Shindell, D., Storelvmo, T., Warren, S., &
1754 Zender, C. (2013). Bounding the role of black carbon in the climate system: A scientific
1755 assessment [Review]. *Journal of Geophysical Research-Atmospheres*, 118(11), 5380-5552.
1756 <https://doi.org/10.1002/jgrd.50171>
- 1757 Bony, S., Colman, R., Kattsov, V., Allan, R., Bretherton, C., Dufresne, J., Hall, A., Hallegatte, S.,
1758 Holland, M., Ingram, W., Randall, D., Soden, B., Tselioudis, G., & Webb, M. (2006). How well
1759 do we understand and evaluate climate change feedback processes? [Review]. *Journal of Climate*,
1760 19(15), 3445-3482. <https://doi.org/10.1175/JCLI3819.1>

1761 Booth, B. B., Dunstone, N. J., Halloran, P. R., Andrews, T., & Bellouin, N. (2012). Aerosols implicated
1762 as a prime driver of twentieth-century North Atlantic climate variability. *Nature*, *484*(7393), 228-
1763 232.

1764 Canty, T., Mascioli, N., Smarte, M., & Salawitch, R. (2013). An empirical model of global climate - Part
1765 1: A critical evaluation of volcanic cooling [Article]. *Atmospheric Chemistry and Physics*, *13*(8),
1766 3997-4031. <https://doi.org/10.5194/acp-13-3997-2013>

1767 Carton, J., Chepurin, G., & Chen, L. (2018). SODA3: A new ocean climate reanalysis. *Journal of*
1768 *Climate*, *31*(17), 6967-6983.

1769 Ceppi, P., Brient, F., Zelinka, M. D., & Hartmann, D. L. (2017). Cloud feedback mechanisms and their
1770 representation in global climate models. *Wiley Interdisciplinary Reviews: Climate Change*, *8*(4),
1771 e465.

1772 Charette, M. A., & Smith, W. H. (2010). The volume of Earth's ocean. *Oceanography*, *23*(2), 112-114.

1773 Chen, Y., & Penner, J. E. (2005). Uncertainty analysis for estimates of the first indirect aerosol effect.

1774 Cheng, L., Trenberth, K., Palmer, M., Zhu, J., & Abraham, J. (2016). Observed and simulated full-depth
1775 ocean heat-content changes for 1970–2005. *Ocean Science*, *12*(4), 925-935.

1776 Christy, J. R., & McNider, R. T. (2017). Satellite bulk tropospheric temperatures as a metric for climate
1777 sensitivity. *Asia-Pacific Journal of Atmospheric Sciences*, *53*(4), 511-518.

1778 Chylek, P., Folland, C., Klett, J. D., & Dubey, M. K. (2020). CMIP5 climate models overestimate cooling
1779 by volcanic aerosols. *Geophysical Research Letters*, *47*(3), e2020GL087047.

1780 Chylek, P., Klett, J. D., Dubey, M. K., & Hengartner, N. (2016). The role of Atlantic Multi-decadal
1781 Oscillation in the global mean temperature variability. *Climate Dynamics*, *47*(9-10), 3271-3279.

1782 Chylek, P., Klett, J. D., Lesins, G., Dubey, M. K., & Hengartner, N. (2014). The Atlantic Multidecadal
1783 Oscillation as a dominant factor of oceanic influence on climate [Article]. *Geophysical Research*
1784 *Letters*, *41*(5), 1689-1697. <https://doi.org/10.1002/2014GL059274>

1785 Collins, M., Knutti, R., Arblaster, J., Dufresne, J.-L., Fichet, T., Friedlingstein, P., Gao, X., Gutowski,
1786 W., Johns, T., & Krinner, G. (2013). Long-term climate change: projections, commitments and
1787 irreversibility. In T. Stocker, D. Qin, G. Plattner, M. Tignor, S. Allen, J. Boschung, A. Nauels, Y.
1788 Xia, B. Bex, & B. Midgley (Eds.), *Climate Change 2013-The Physical Science Basis:
1789 Contribution of Working Group I to the Fifth Assessment Report of the Intergovernmental Panel
1790 on Climate Change* (pp. 1029-1136). Cambridge University Press.

1791 Collins, W. J., Lamarque, J.-F., Schulz, M., Boucher, O., Eyring, V., Hegglin, M. I., Maycock, A., Myhre,
1792 G., Prather, M., & Shindell, D. (2017). AerChemMIP: quantifying the effects of chemistry and
1793 aerosols in CMIP6. *Geoscientific Model Development*, *10*(2), 585-607.

1794 Comyn-Platt, E., Hayman, G., Huntingford, C., Chadburn, S. E., Burke, E. J., Harper, A. B., Collins, W.
1795 J., Webber, C. P., Powell, T., & Cox, P. M. (2018). Carbon budgets for 1.5 and 2 C targets
1796 lowered by natural wetland and permafrost feedbacks. *Nature geoscience*, *11*(8), 568.

1797 Cowtan, K., Hausfather, Z., Hawkins, E., Jacobs, P., Mann, M., Miller, S., Steinman, B., Stolpe, M., &
1798 Way, R. (2015). Robust comparison of climate models with observations using blended land air
1799 and ocean sea surface temperatures. *Geophysical Research Letters*, *42*(15), 6526-6534.

1800 DelSole, T., Tippett, M., & Shukla, J. (2011). A Significant Component of Unforced Multidecadal
1801 Variability in the Recent Acceleration of Global Warming [Article]. *Journal of Climate*, *24*(3),
1802 909-926. <https://doi.org/10.1175/2010JCLI3659.1>

1803 Deser, C., & Wallace, J. M. (1990). Large-scale atmospheric circulation features of warm and cold
1804 episodes in the tropical Pacific. *Journal of Climate*, *3*(11), 1254-1281.

1805 Dessler, A. (2013). Observations of climate feedbacks over 2000–10 and comparisons to climate models.
1806 *Journal of Climate*, *26*(1), 333-342.

1807 Dolinar, E. K., Dong, X., Xi, B., Jiang, J. H., & Su, H. (2015). Evaluation of CMIP5 simulated clouds and
1808 TOA radiation budgets using NASA satellite observations. *Climate Dynamics*, *44*(7-8), 2229-
1809 2247.

1810 Domingues, C., Church, J., White, N., Gleckler, P., Wijffels, S., Barker, P., & Dunn, J. (2008). Improved
1811 estimates of upper-ocean warming and multi-decadal sea-level rise. *Nature*, *453*(7198), 1090-
1812 1093.

1813 Duche, A., Hirschi, J.-M., Cunningham, S., Blaker, A., Bryden, H., de Cuevas, B., Atkinson, C.,
1814 McCarthy, G., Frajka-Williams, E., & Rayner, D. (2014). A new index for the Atlantic
1815 Meridional Overturning Circulation at 26° N. *Journal of Climate*, *27*(17), 6439-6455.

1816 Dudok de Wit, T., Kopp, G., Fröhlich, C., & Schöll, M. (2017). Methodology to create a new total solar
1817 irradiance record: Making a composite out of multiple data records. *Geophysical Research*
1818 *Letters*, *44*(3), 1196-1203.

1819 England, M., McGregor, S., Spence, P., Meehl, G., Timmermann, A., Cai, W., Sen Gupta, A., McPhaden,
1820 M., Purich, A., & Santoso, A. (2014). Recent intensification of wind-driven circulation in the
1821 Pacific and the ongoing warming hiatus [Article]. *Nature Climate Change*, *4*(3), 222-227.
1822 <https://doi.org/10.1038/NCLIMATE2106>

1823 Fawcett, A. A., Iyer, G. C., Clarke, L. E., Edmonds, J. A., Hultman, N. E., McJeon, H. C., Rogelj, J.,
1824 Schuler, R., Alsalam, J., & Asrar, G. R. (2015). Can Paris pledges avert severe climate change?
1825 *Science*, *350*(6265), 1168-1169.

1826 Flato, G., Marotzke, J., Abiodun, B., Braconnot, P., Chou, S., Collins, W., Cox, P., Driouech, F., Emori,
1827 S., & Eyring, V. (2013). Evaluation of climate models. In T. Stocker, D. Qin, G. Plattner, M.

1828 Tignor, S. Allen, J. Boschung, A. Nauels, Y. Xia, B. Bex, & B. Midgley (Eds.), *Climate change*
1829 *2013: the physical science basis. Contribution of Working Group I to the Fifth Assessment Report*
1830 *of the Intergovernmental Panel on Climate Change* (pp. 741-866). Cambridge University Press.

1831 Folland, C. K., Boucher, O., Colman, A., & Parker, D. E. (2018). Causes of irregularities in trends of
1832 global mean surface temperature since the late 19th century. *Science advances*, 4(6), eaao5297.

1833 Forster, P., Andrews, T., Good, P., Gregory, J., Jackson, L., & Zelinka, M. (2013). Evaluating adjusted
1834 forcing and model spread for historical and future scenarios in the CMIP5 generation of climate
1835 models [Article]. *Journal of Geophysical Research-Atmospheres*, 118(3), 1139-1150.
1836 <https://doi.org/10.1002/jgrd.50174>

1837 Forster, P. M., Maycock, A. C., McKenna, C. M., & Smith, C. J. (2020). Latest climate models confirm
1838 need for urgent mitigation. *Nature Climate Change*, 10(1), 7-10.

1839 Foster, G., & Rahmstorf, S. (2011). Global temperature evolution 1979-2010 [Article]. *Environmental*
1840 *Research Letters*, 6(4), Article ARTN 044022. <https://doi.org/10.1088/1748-9326/6/4/044022>

1841 Friedlingstein, P., Jones, M., O'sullivan, M., Andrew, R., Hauck, J., Peters, G., Peters, W., Pongratz, J.,
1842 Sitch, S., & Le Quéré, C. (2019). Global carbon budget 2019. *Earth System Science Data*, 11(4),
1843 1783-1838.

1844 Fyfe, J., Gillett, N., & Zwiers, F. (2013). Overestimated global warming over the past 20 years [Editorial
1845 Material]. *Nature Climate Change*, 3(9), 767-769.

1846 Gettelman, A., Hannay, C., Bacmeister, J., Neale, R., Pendergrass, A., Danabasoglu, G., Lamarque, J. F.,
1847 Fasullo, J., Bailey, D., & Lawrence, D. (2019). High climate sensitivity in the Community Earth
1848 System Model version 2 (CESM2). *Geophysical Research Letters*, 46(14), 8329-8337.

1849 Goodwin, P., Katavouta, A., Roussenov, V. M., Foster, G. L., Rohling, E. J., & Williams, R. G. (2018).
1850 Pathways to 1.5 C and 2 C warming based on observational and geological constraints. *Nature*
1851 *Geoscience*, 11(2), 102-107.

1852 Gregory, J. (2000). Vertical heat transports in the ocean and their effect on time-dependent climate
1853 change. *Climate Dynamics*, 16(7), 501-515.

1854 Gregory, J., Jones, C., Cadule, P., & Friedlingstein, P. (2009). Quantifying carbon cycle feedbacks.
1855 *Journal of Climate*, 22(19), 5232-5250.

1856 Gryspeerdt, E., Muelmenstadt, J., Gettelman, A., Malavelle, F. F., Morrison, H., Neubauer, D., Partridge,
1857 D. G., Stier, P., Takemura, T., & Wang, H. (2020). Surprising similarities in model and
1858 observational aerosol radiative forcing estimates. *Atmospheric Chemistry and Physics*, 20(1),
1859 613-623.

1860 Hansen, J., Ruedy, R., Sato, M., & Lo, K. (2010). GLOBAL SURFACE TEMPERATURE CHANGE
1861 [Review]. *Reviews of Geophysics*, 48, Article ARTN RG4004.
1862 <https://doi.org/10.1029/2010RG000345>

1863 Hausfather, Z., Drake, H., Abbott, T., & Schmidt, G. (2020). Evaluating the performance of past climate
1864 model projections. *Geophysical Research Letters*, 47(1), e2019GL085378.

1865 Haustein, K., Otto, F., Venema, V., Jacobs, P., Cowtan, K., Hausfather, Z., Way, R., White, B.,
1866 Subramanian, A., & Schurer, A. (2019). A limited role for unforced internal variability in 20 th
1867 century warming. *Journal of Climate*(2019).

1868 Hope, A. P., Canty, T. P., Salawitch, R. J., Tribett, W. R., & Bennett, B. F. (2017). Forecasting Global
1869 Warming. In *Paris Climate Agreement: Beacon of Hope* (pp. 51-113). Springer.

1870 Hourdin, F., Grandpeix, J.-Y., Rio, C., Bony, S., Jam, A., Cheruy, F., Rochetin, N., Fairhead, L., Idelkadi,
1871 A., & Musat, I. (2013). LMDZ5B: the atmospheric component of the IPSL climate model with
1872 revisited parameterizations for clouds and convection. *Climate Dynamics*, 40(9-10), 2193-2222.

1873 IPCC. (2013). Summary for Policymakers. In T. Stocker, D. Qin, G. Plattner, M. Tignor, S. Allen, J.
1874 Boschung, A. Nauels, Y. Xia, B. Bex, & B. Midgley (Eds.), *Climate Change 2013 the Physical
1875 Science Basis: Working Group I Contribution to the Fifth Assessment Report of the
1876 Intergovernmental Panel on Climate Change* (pp. 3-29). Cambridge University Press.

1877 Ishii, M., Fukuda, Y., Hirahara, S., Yasui, S., Suzuki, T., & Sato, K. (2017). Accuracy of global upper
1878 ocean heat content estimation expected from present observational data sets. *SOLA*, 13, 163-167.

1879 Ishii, M., Shouji, A., Sugimoto, S., & Matsumoto, T. (2005). Objective analyses of sea-surface
1880 temperature and marine meteorological variables for the 20th century using ICOADS and the
1881 Kobe collection. *International Journal of Climatology: A Journal of the Royal Meteorological
1882 Society*, 25(7), 865-879.

1883 Jackson, R. B., Le Quéré, C., Andrew, R., Canadell, J. G., Korsbakken, J. I., Liu, Z., Peters, G. P., &
1884 Zheng, B. (2018). Global energy growth is outpacing decarbonization. *Environmental Research
1885 Letters*, 13(12), 120401.

1886 Jones, P., Lister, D., Osborn, T., Harpham, C., Salmon, M., & Morice, C. (2012). Hemispheric and large-
1887 scale land-surface air temperature variations: An extensive revision and an update to 2010
1888 [Article]. *Journal of Geophysical Research-Atmospheres*, 117, Article ARTN D05127.
1889 <https://doi.org/10.1029/2011JD017139>

1890 Kavvada, A., Ruiz-Barradas, A., & Nigam, S. (2013). AMO's structure and climate footprint in
1891 observations and IPCC AR5 climate simulations [Article]. *Climate Dynamics*, 41(5-6), 1345-
1892 1364. <https://doi.org/10.1007/s00382-013-1712-1>

1893 Kiehl, J. (2007). Twentieth century climate model response and climate sensitivity [Article]. *Geophysical*
1894 *Research Letters*, 34(22), Article ARTN L22710. <https://doi.org/10.1029/2007GL031383>

1895 Kirtman, B., Power, S., Adedoyin, A., Boer, G., Bojariu, R., Camilloni, I., Doblus-Reyes, F., Fiore, A.,
1896 Kimoto, M., & Meehl, G. (2013). Near-term climate change: Projections and predictability. In T.
1897 Stocker, D. Qin, G. Plattner, M. Tignor, S. Allen, J. Boschung, A. Nauels, Y. Xia, B. Bex, & B.
1898 Midgley (Eds.), *Climate Change 2013 the Physical Science Basis: Working Group I Contribution*
1899 *to the Fifth Assessment Report of the Intergovernmental Panel on Climate Change* (pp. 953-
1900 1028). Cambridge University Press.

1901 Klein, S. A., Hall, A., Norris, J. R., & Pincus, R. (2017). Low-cloud feedbacks from cloud-controlling
1902 factors: a review. In *Shallow Clouds, Water Vapor, Circulation, and Climate Sensitivity* (pp. 135-
1903 157). Springer.

1904 Knight, J. R., Allan, R. J., Folland, C. K., Vellinga, M., & Mann, M. E. (2005). A signature of persistent
1905 natural thermohaline circulation cycles in observed climate. *Geophysical Research Letters*,
1906 32(20).

1907 Knutti, R., & Hegerl, G. C. (2008). The equilibrium sensitivity of the Earth's temperature to radiation
1908 changes. *Nature Geoscience*, 1(11), 735.

1909 Lamarque, J., Kyle, G., Meinshausen, M., Riahi, K., Smith, S., van Vuuren, D., Conley, A., & Vitt, F.
1910 (2011). Global and regional evolution of short-lived radiatively-active gases and aerosols in the
1911 Representative Concentration Pathways [Article]. *Climatic Change*, 109(1-2), 191-212.
1912 <https://doi.org/10.1007/s10584-011-0155-0>

1913 Le Quéré, C., Andrew, R. M., Friedlingstein, P., Sitch, S., Hauck, J., Pongratz, J., Pickers, P. A.,
1914 Korsbakken, J. I., Peters, G. P., & Canadell, J. G. (2018). Global carbon budget 2018. *Earth*
1915 *System Science Data*, 10(4), 2141-2194.

1916 Lean, J. L., & Rind, D. H. (2008). How natural and anthropogenic influences alter global and regional
1917 surface temperatures: 1889 to 2006 [Article]. *Geophysical Research Letters*, 35(18), Article
1918 ARTN L18701. <https://doi.org/10.1029/2008GL034864>

1919 Lean, J. L., & Rind, D. H. (2009). How will Earth's surface temperature change in future decades?
1920 *Geophysical Research Letters*, 36(15).

1921 Levitus, S., Antonov, J. I., Boyer, T. P., Baranova, O. K., Garcia, H. E., Locarnini, R. A., Mishonov, A.
1922 V., Reagan, J., Seidov, D., & Yarosh, E. S. (2012). World ocean heat content and thermosteric
1923 sea level change (0–2000 m), 1955–2010. *Geophysical Research Letters*, 39(10).

1924 Lewis, N., & Curry, J. (2018). The impact of recent forcing and ocean heat uptake data on estimates of
1925 climate sensitivity. *Journal of Climate*, 31(15), 6051-6071.

- 1926 Lin, Y. J., Hwang, Y. T., Ceppi, P., & Gregory, J. M. (2019). Uncertainty in the evolution of climate
 1927 feedback traced to the strength of the Atlantic Meridional Overturning Circulation. *Geophysical*
 1928 *Research Letters*, *46*(21), 12331-12339.
- 1929 Marvel, K., Pincus, R., Schmidt, G. A., & Miller, R. L. (2018). Internal variability and disequilibrium
 1930 confound estimates of climate sensitivity from observations. *Geophysical Research Letters*,
 1931 *45*(3), 1595-1601.
- 1932 Masters, T. (2014). Observational estimate of climate sensitivity from changes in the rate of ocean heat
 1933 uptake and comparison to CMIP5 models. *Climate dynamics*, *42*(7-8), 2173-2181.
- 1934 Masui, T., Matsumoto, K., Hijioka, Y., Kinoshita, T., Nozawa, T., Ishiwatari, S., Kato, E., Shukla, P.,
 1935 Yamagata, Y., & Kainuma, M. (2011). An emission pathway for stabilization at 6 Wm⁻²
 1936 radiative forcing. *Climatic change*, *109*(1-2), 59.
- 1937 Matthes, K., Funke, B., Anderson, M., Barnard, L., Beer, J., Charbonneau, P., Clilverd, M., Dudok de
 1938 Wit, T., Haberreiter, M., & Hendry, A. (2017). Solar forcing for CMIP6 (v3. 2). *Geoscientific*
 1939 *Model Development*, *10*(6), 2247-2302.
- 1940 Mauritsen, T., & Pincus, R. (2017). Committed warming inferred from observations. *Nature Climate*
 1941 *Change*, *7*(9), 652-655.
- 1942 Medhaug, I., & Furevik, T. (2011). North Atlantic 20th century multidecadal variability in coupled
 1943 climate models: sea surface temperature and ocean overturning circulation.
- 1944 Meehl, G. A., Arblaster, J. M., Fasullo, J. T., Hu, A., & Trenberth, K. E. (2011). Model-based evidence of
 1945 deep-ocean heat uptake during surface-temperature hiatus periods. *Nature Climate Change*, *1*(7),
 1946 360-364.
- 1947 Meinshausen, M., Meinshausen, N., Hare, W., Raper, S. C., Frieler, K., Knutti, R., Frame, D. J., & Allen,
 1948 M. R. (2009). Greenhouse-gas emission targets for limiting global warming to 2 C. *Nature*,
 1949 *458*(7242), 1158.
- 1950 Meinshausen, M., Smith, S., Calvin, K., Daniel, J., Kainuma, M., Lamarque, J., Matsumoto, K., Montzka,
 1951 S., Raper, S., Riahi, K., Thomson, A., Velders, G., & van Vuuren, D. (2011). The RCP
 1952 greenhouse gas concentrations and their extensions from 1765 to 2300 [Article]. *Climatic*
 1953 *Change*, *109*(1-2), 213-241. <https://doi.org/10.1007/s10584-011-0156-z>
- 1954 Millar, R. J., Fuglestedt, J. S., Friedlingstein, P., Rogelj, J., Grubb, M. J., Matthews, H. D., Skeie, R. B.,
 1955 Forster, P. M., Frame, D. J., & Allen, M. R. (2017). Emission budgets and pathways consistent
 1956 with limiting warming to 1.5C. *Nature Geoscience*, *10*(10), 741-747.
- 1957 Molnár, A. (2018). Leaking away the future: The role of methane emission and natural gas supply chains
 1958 in global warming. *Energy Policy Studies*.

- 1959 Myhre, G., Highwood, E. J., Shine, K. P., & Stordal, F. (1998). New estimates of radiative forcing due to
 1960 well mixed greenhouse gases. *Geophysical research letters*, 25(14), 2715-2718.
- 1961 Myhre, G., Shindell, D., Bréon, F., Collins, W., Fuglestedt, J., Huang, J., Koch, D., Lamarque, J., Lee,
 1962 D., & Mendoza, B. (2013). Anthropogenic and Natural Radiative Forcing. In T. Stocker, D. Qin,
 1963 G. Plattner, M. Tignor, S. Allen, J. Boschung, A. Nauels, Y. Xia, B. Bex, & B. Midgley (Eds.),
 1964 *Climate Change 2013 the Physical Science Basis: Working Group I Contribution to the Fifth*
 1965 *Assessment Report of the Intergovernmental Panel on Climate Change* (pp. 659-740). Cambridge
 1966 University Press.
- 1967 Nijssse, F. J., Cox, P. M., & Williamson, M. S. (2020). Emergent constraints on transient climate response
 1968 (TCR) and equilibrium climate sensitivity (ECS) from historical warming in CMIP5 and CMIP6
 1969 models. *Earth System Dynamics*, 11(3), 737-750.
- 1970 Nisbet, E., Manning, M., Dlugokencky, E., Fisher, R., Lowry, D., Michel, S., Myhre, C. L., Platt, S. M.,
 1971 Allen, G., & Bousquet, P. (2019). Very strong atmospheric methane growth in the 4 years 2014–
 1972 2017: Implications for the Paris Agreement. *Global Biogeochemical Cycles*, 33(3), 318-342.
- 1973 Otto, A., Otto, F. E., Boucher, O., Church, J., Hegerl, G., Forster, P. M., Gillett, N. P., Gregory, J.,
 1974 Johnson, G. C., & Knutti, R. (2013). Energy budget constraints on climate response. *Nature*
 1975 *Geoscience*, 6(6), 415-416.
- 1976 Pausata, F. S., Chafik, L., Caballero, R., & Battisti, D. S. (2015). Impacts of high-latitude volcanic
 1977 eruptions on ENSO and AMOC. *Proceedings of the National Academy of Sciences*, 112(45),
 1978 13784-13788.
- 1979 Pincus, R., Forster, P. M., & Stevens, B. (2016). The radiative forcing model intercomparison project
 1980 (RFMIP): Experimental protocol for CMIP6. *Geoscientific Model Development (Online)*, 9(9).
- 1981 Raftery, A. E., Zimmer, A., Frierson, D. M., Startz, R., & Liu, P. (2017). Less than 2 °C warming by 2100
 1982 unlikely. *Nature Climate Change*, 7(9), 637-641.
- 1983 Rahmstorf, S., Box, J., Feulner, G., Mann, M., Robinson, A., Rutherford, S., & Schaffernicht, E. (2015).
 1984 Exceptional twentieth-century slowdown in Atlantic Ocean overturning circulation [Article].
 1985 *Nature Climate Change*, 5(5), 475-480. <https://doi.org/10.1038/NCLIMATE2554>
- 1986 Raper, S., Gregory, J., & Stouffer, R. (2002). The role of climate sensitivity and ocean heat uptake on
 1987 AOGCM transient temperature response [Article]. *Journal of Climate*, 15(1), 124-130.
 1988 [https://doi.org/10.1175/1520-0442\(2002\)015<0124:TROCSA>2.0.CO;2](https://doi.org/10.1175/1520-0442(2002)015<0124:TROCSA>2.0.CO;2)
- 1989 Riahi, K., Rao, S., Krey, V., Cho, C., Chirkov, V., Fischer, G., Kindermann, G., Nakicenovic, N., &
 1990 Rafaj, P. (2011). RCP 8.5—A scenario of comparatively high greenhouse gas emissions. *Climatic*
 1991 *change*, 109(1-2), 33.

- 1992 Rogelj, J., Shindell, D., Jiang, K., Fifita, S., Forester, P., Ginzburg, V., Handa, C., Kheshgi, H.,
 1993 Kobayashi, S., & Kriegler, E. (2018). Mitigation pathways compatible with 1.5° C in the context
 1994 of sustainable development. IPCC Special Report on global warming of 1.5° C.
- 1995 Rohde, R., Muller, R., Jacobsen, R., Perlmutter, S., Rosenfeld, A., Wurtele, J., Curry, J., Wickhams, C.,
 1996 & Mosher, S. (2013). Berkeley Earth Temperature Averaging Process. *Geoinfor Geostat: An*
 1997 *Overview 1: 2. of, 13*, 20-100.
- 1998 Rose, B., Armour, K., Battisti, D., Feldl, N., & Koll, D. (2014). The dependence of transient climate
 1999 sensitivity and radiative feedbacks on the spatial pattern of ocean heat uptake [Article].
 2000 *Geophysical Research Letters*, *41*(3), 1071-1078. <https://doi.org/10.1002/2013GL058955>
- 2001 Saji, N., Goswami, B., Vinayachandran, P., & Yamagata, T. (1999). A dipole mode in the tropical Indian
 2002 Ocean [Article]. *Nature*, *401*(6751), 360-363. <https://doi.org/10.1038/43855>
- 2003 Santer, B., Painter, J., Bonfils, C., Mears, C., Solomon, S., Wigley, T., Gleckler, P., Schmidt, G.,
 2004 Doutriaux, C., Gillett, N., Taylor, K., Thorne, P., & Wentz, F. (2013). Human and natural
 2005 influences on the changing thermal structure of the atmosphere [Article]. *Proceedings of the*
 2006 *National Academy of Sciences of the United States of America*, *110*(43), 17235-17240.
 2007 <https://doi.org/10.1073/pnas.1305332110>
- 2008 Saravanan, R., & McWilliams, J. C. (1998). Advective ocean–atmosphere interaction: An analytical
 2009 stochastic model with implications for decadal variability. *Journal of Climate*, *11*(2), 165-188.
- 2010 Saunio, M., Jackson, R., Bousquet, P., Poulter, B., & Canadell, J. (2016). The growing role of methane
 2011 in anthropogenic climate change. *Environmental Research Letters*, *11*(12), 120207.
- 2012 Saunio, M., Stavert, A. R., Poulter, B., Bousquet, P., Canadell, J. G., Jackson, R. B., Raymond, P. A.,
 2013 Dlugokencky, E. J., Houweling, S., & Patra, P. K. (2020). The global methane budget 2000–
 2014 2017. *Earth system science data*, *12*(3), 1561-1623.
- 2015 Schlesinger, M. E., & Ramankutty, N. (1994). An oscillation in the global climate system of period 65–70
 2016 years. *Nature*, *367*(6465), 723.
- 2017 Schmidt, G., Shindell, D., & Tsigaridis, K. (2014). Reconciling warming trends [Editorial Material].
 2018 *Nature Geoscience*, *7*(3), 158-160. <https://doi.org/10.1038/ngeo2105>
- 2019 Schwartz, S. E. (2012). Determination of Earth's Transient and Equilibrium Climate Sensitivities from
 2020 Observations Over the Twentieth Century: Strong Dependence on Assumed Forcing [Review].
 2021 *Surveys in Geophysics*, *33*(3-4), 745-777. <https://doi.org/10.1007/s10712-012-9180-4>
- 2022 Schwartz, S. E., Charlson, R. J., Kahn, R., & Rodhe, H. (2014). Earth's climate sensitivity: apparent
 2023 inconsistencies in recent assessments. *Earth's Future*, *2*(12), 601-605.

2024 Shen, Z., Ming, Y., & Held, I. M. (2020). Using the fast impact of anthropogenic aerosols on regional
2025 land temperature to constrain aerosol forcing. *Science Advances*, 6(32), eabb5297.
2026 <https://doi.org/10.1126/sciadv.abb5297>

2027 Sherwood, S., Webb, M. J., Annan, J. D., Armour, K. C., Forster, P. M., Hargreaves, J. C., Hegerl, G.,
2028 Klein, S. A., Marvel, K. D., Rohling, E. J., Watanabe, M., Andrews, T., Braconnot, P.,
2029 Bretherton, C. S., Foster, G. L., Hausfather, Z., Heydt, A. S. v. d., Knutti, R., Mauritsen, T.,
2030 Norris, J. R., Proistosescu, C., Rugenstein, M., Schmidt, G. A., Tokarska, K. B., & Zelinka, M. D.
2031 (2020). An assessment of Earth's climate sensitivity using multiple lines of evidence. *Reviews of*
2032 *Geophysics*, n/a(n/a), e2019RG000678. <https://doi.org/10.1029/2019rg000678>

2033 Shindell, D. T. (2014). Inhomogeneous forcing and transient climate sensitivity. *Nature Climate Change*,
2034 4(4), 274-277.

2035 Silver, N. (2012). *The signal and the noise: why so many predictions fail--but some don't*. Penguin.

2036 Smeed, D., Rayner, D., McCarthy, G., Moat, B., Johns, W. E., Baringer, M. O., Meinen, C. S., & Collins,
2037 J. (2017). RAPID-MOC time series April 2004 to February 2017.

2038 Smith, S., Aardenne, J. v., Klimont, Z., Andres, R., Volke, A., & Delgado Arias, S. (2011).
2039 Anthropogenic sulfur dioxide emissions: 1850–2005. *Atmospheric Chemistry and Physics*, 11(3),
2040 1101-1116.

2041 Smith, S., & Bond, T. (2014). Two hundred fifty years of aerosols and climate: the end of the age of
2042 aerosols [Article]. *Atmospheric Chemistry and Physics*, 14(2), 537-549.
2043 <https://doi.org/10.5194/acp-14-537-2014>

2044 Smith, T., Reynolds, R., Peterson, T., & Lawrimore, J. (2008). Improvements to NOAA's historical
2045 merged land-ocean surface temperature analysis (1880-2006) [Article]. *Journal of Climate*,
2046 21(10), 2283-2296. <https://doi.org/10.1175/2007JCLI2100.1>

2047 Solomon, S. (2007). *Climate change 2007-the physical science basis: Working group I contribution to the*
2048 *fourth assessment report of the IPCC* (Vol. 4). Cambridge University Press.

2049 Srokosz, M., & Bryden, H. (2015). Observing the Atlantic Meridional Overturning Circulation yields a
2050 decade of inevitable surprises. *Science*, 348(6241), 1255575.

2051 Steinman, B. A., Mann, M. E., & Miller, S. K. (2015). Atlantic and Pacific multidecadal oscillations and
2052 Northern Hemisphere temperatures. *Science*, 347(6225), 988-991.

2053 Stern, D. I. (2006). Reversal of the trend in global anthropogenic sulfur emissions. *Global Environmental*
2054 *Change*, 16(2), 207-220.

2055 Stocker, T., Qin, D., Plattner, G., Tignor, M., Allen, S., Boschung, J., Nauels, A., Xia, Y., Bex, B., &
2056 Midgley, B. (2013). IPCC, 2013: climate change 2013: the physical science basis. Contribution of
2057 working group I to the fifth assessment report of the intergovernmental panel on climate change.

2058 Stouffer, R. J., Yin, J., Gregory, J., Dixon, K., Spelman, M., Hurlin, W., Weaver, A., Eby, M., Flato, G.,
2059 & Hasumi, H. (2006). Investigating the causes of the response of the thermohaline circulation to
2060 past and future climate changes. *Journal of Climate*, 19(8), 1365-1387.

2061 Suckling, E. B., van Oldenborgh, G. J., Eden, J. M., & Hawkins, E. (2017). An empirical model for
2062 probabilistic decadal prediction: global attribution and regional hindcasts. *Climate Dynamics*,
2063 48(9-10), 3115-3138.

2064 Taylor, K., Stouffer, R., & Meehl, G. (2012). AN OVERVIEW OF CMIP5 AND THE EXPERIMENT
2065 DESIGN [Article]. *Bulletin of the American Meteorological Society*, 93(4), 485-498.
2066 <https://doi.org/10.1175/BAMS-D-11-00094.1>

2067 Thomason, L., Ernest, N., Millán, L., Rieger, L., Bourassa, A., Vernier, J.-P., Manney, G., Luo, B.,
2068 Arfeuille, F., & Peter, T. (2018). A global space-based stratospheric aerosol climatology: 1979-
2069 2016. *Earth System Science Data*, 10(1), 469-492.

2070 Thomason, L., Vernier, J.-P., Bourassa, A., Millan, L., & Manney, G. (2016). A global, space-based
2071 stratospheric aerosol climatology: 1979 to 2014. AGU Fall Meeting Abstracts,

2072 Thompson, D. W., Wallace, J. M., Jones, P. D., & Kennedy, J. J. (2009). Identifying signatures of natural
2073 climate variability in time series of global-mean surface temperature: Methodology and insights.
2074 *Journal of Climate*, 22(22), 6120-6141.

2075 Thomson, A. M., Calvin, K. V., Smith, S. J., Kyle, G. P., Volke, A., Patel, P., Delgado-Arias, S., Bond-
2076 Lamberty, B., Wise, M. A., & Clarke, L. E. (2011). RCP4. 5: a pathway for stabilization of
2077 radiative forcing by 2100. *Climatic change*, 109(1-2), 77-94.

2078 Thornhill, G., Collins, W., Olivié, D., Archibald, A., Bauer, S., Checa-Garcia, R., Fiedler, S., Folberth,
2079 G., Gjermundsen, A., Horowitz, L., Lamarque, J.-F., Michou, M., Mulcahy, J., Nabat, P., Naik,
2080 V., O'Connor, F. M., Paulot, F., Schulz, M., Scott, C. E., Seferian, R., Smith, C., Takemura, T.,
2081 Tilmes, S., & Weber, J. (2020). Climate-driven chemistry and aerosol feedbacks in CMIP6 Earth
2082 system models. *Atmospheric Chemistry and Physics Discussion (in review)*.
2083 <https://doi.org/https://doi.org/10.5194/acp-2019-1207>

2084 Tokarska, K. B., & Gillett, N. P. (2018). Cumulative carbon emissions budgets consistent with 1.5 C
2085 global warming. *Nature Climate Change*, 8(4), 296.

2086 Tokarska, K. B., Schleussner, C.-F., Rogelj, J., Stolpe, M. B., Matthews, H. D., Pfleiderer, P., & Gillett,
2087 N. P. (2019). Recommended temperature metrics for carbon budget estimates, model evaluation
2088 and climate policy. *Nature Geoscience*, 12(12), 964-971.

2089 Tokarska, K. B., Stolpe, M. B., Sippel, S., Fischer, E. M., Smith, C. J., Lehner, F., & Knutti, R. (2020).
2090 Past warming trend constrains future warming in CMIP6 models. *Science advances*, 6(12),
2091 eaaz9549.

2092 Trenberth, K. E. (1997). The definition of el nino. *Bulletin of the American Meteorological Society*,
2093 78(12), 2771-2777.

2094 Tung, K., & Zhou, J. (2013). Using data to attribute episodes of warming and cooling in instrumental
2095 records [Article]. *Proceedings of the National Academy of Sciences of the United States of*
2096 *America*, 110(6), 2058-2063. <https://doi.org/10.1073/pnas.1212471110>

2097 [Record #124 is using a reference type undefined in this output style.]

2098 Van Vuuren, D. P., Edmonds, J., Kainuma, M., Riahi, K., Thomson, A., Hibbard, K., Hurtt, G. C., Kram,
2099 T., Krey, V., & Lamarque, J.-F. (2011). The representative concentration pathways: an overview.
2100 *Climatic change*, 109(1-2), 5.

2101 Van Vuuren, D. P., Stehfest, E., den Elzen, M. G., Kram, T., van Vliet, J., Deetman, S., Isaac, M.,
2102 Goldewijk, K. K., Hof, A., & Beltran, A. M. (2011). RCP2. 6: exploring the possibility to keep
2103 global mean temperature increase below 2 C. *Climatic change*, 109(1-2), 95.

2104 Vaughan, M. A., Young, S. A., Winker, D. M., Powell, K. A., Omar, A. H., Liu, Z., Hu, Y., & Hostetler,
2105 C. A. (2004). Fully automated analysis of space-based lidar data: An overview of the CALIPSO
2106 retrieval algorithms and data products. *Laser radar techniques for atmospheric sensing*,

2107 Vial, J., Dufresne, J., & Bony, S. (2013). On the interpretation of inter-model spread in CMIP5 climate
2108 sensitivity estimates [Article]. *Climate Dynamics*, 41(11-12), 3339-3362.
2109 <https://doi.org/10.1007/s00382-013-1725-9>

2110 Voigt, C., Lamprecht, R. E., Marushchak, M. E., Lind, S. E., Novakovskiy, A., Aurela, M., Martikainen,
2111 P. J., & Biasi, C. (2017). Warming of subarctic tundra increases emissions of all three important
2112 greenhouse gases—carbon dioxide, methane, and nitrous oxide. *Global Change Biology*, 23(8),
2113 3121-3138.

2114 Volodin, E., Dianskii, N., & Gusev, A. (2010). Simulating present-day climate with the INMCM4. 0
2115 coupled model of the atmospheric and oceanic general circulations. *Izvestiya, Atmospheric and*
2116 *Oceanic Physics*, 46(4), 414-431.

2117 Voosen, P. (2019). New climate models forecast a warming surge. *Science (New York, NY)*, 364(6437),
2118 222-223.

2119 Weaver, C. J., Wu, D. L., Bhartia, P. K., Labow, G. J., & Haffner, D. P. (2020). A Long-Term Cloud
2120 Albedo Data Record Since 1980 from UV Satellite Sensors. *Remote Sensing*, 12(12), 1982.

2121 Wolter, K., & Timlin, M. S. (1993). Monitoring ENSO in COADS with a Seasonally Adjusted Principal.
2122 Proc. of the 17th Climate Diagnostics Workshop, Norman, OK, NOAA/NMC/CAC, NSSL,
2123 Oklahoma Clim. Survey, CIMMS and the School of Meteor., Univ. of Oklahoma, 52,

- 2124 Wolter, K., & Timlin, M. S. (2011). El Niño/Southern Oscillation behaviour since 1871 as diagnosed in
2125 an extended multivariate ENSO index (MEI. ext). *International Journal of Climatology*, *31*(7),
2126 1074-1087.
- 2127 Wu, L., & Liu, Z. (2003). Decadal variability in the North Pacific: the eastern North Pacific mode.
2128 *Journal of Climate*, *16*(19), 3111-3131.
- 2129 Yukimoto, S., Adachi, Y., Hosaka, M., Sakami, T., Yoshimura, H., Hirabara, M., Tanaka, T. Y., Shindo,
2130 E., Tsujino, H., & Deushi, M. (2012). A new global climate model of the Meteorological
2131 Research Institute: MRI-CGCM3—Model description and basic performance—. *Journal of the*
2132 *Meteorological Society of Japan. Ser. II*, *90*, 23-64.
- 2133 Zanchettin, D., Khodri, M., Timmreck, C., Toohey, M., Schmidt, A., Gerber, E., Hegerl, G., Robock, A.,
2134 Pausata, F., & Ball, W. (2016). The Model Intercomparison Project on the climatic response to
2135 Volcanic forcing (VolMIP): experimental design and forcing input data for CMIP6. *Geoscientific*
2136 *Model Development*, *9*(8), 2701-2719.
- 2137 Zelinka, M., Klein, S., Taylor, K., Andrews, T., Webb, M., Gregory, J., & Forster, P. (2013).
2138 Contributions of Different Cloud Types to Feedbacks and Rapid Adjustments in CMIP5 [Article].
2139 *Journal of Climate*, *26*(14), 5007-5027. <https://doi.org/10.1175/JCLI-D-12-00555.1>
- 2140 Zelinka, M. D., Myers, T. A., McCoy, D. T., Po-Chedley, S., Caldwell, P. M., Ceppi, P., Klein, S. A., &
2141 Taylor, K. E. (2020). Causes of higher climate sensitivity in CMIP6 models. *Geophysical*
2142 *Research Letters*, *47*(1), e2019GL085782.
- 2143 Zelinka, M. D., Zhou, C., & Klein, S. A. (2016). Insights from a refined decomposition of cloud
2144 feedbacks. *Geophysical Research Letters*, *43*(17), 9259-9269.
- 2145 Zeng, X., & Geil, K. (2016). Global warming projection in the 21st century based on an observational
2146 data-driven model. *Geophysical Research Letters*, *43*(20).
- 2147 Zhang, H., Lawrimore, J., Huang, B., Menne, M., Yin, X., Sánchez-Lugo, A., Gleason, B., Vose, R.,
2148 Arndt, D., & Rennie, J. (2019). Updated temperature data give a sharper view of climate trends.
2149 *Eos*, *100*.
- 2150 Zhang, Y., Wallace, J. M., & Battisti, D. S. (1997). ENSO-like interdecadal variability: 1900-93. *Journal*
2151 *of climate*, *10*(5), 1004-1020.
- 2152 Zharkova, V. V., Shepherd, S. J., Popova, E., & Zharkov, S. I. (2015). Heartbeat of the Sun from
2153 Principal Component Analysis and prediction of solar activity on a millenium timescale.
2154 *Scientific reports*, *5*, 15689.
- 2155 Zhou, C., Zelinka, M. D., Dessler, A. E., & Klein, S. A. (2015). The relationship between interannual and
2156 long-term cloud feedbacks. *Geophysical Research Letters*, *42*(23).

- 2157 Zhou, J., & Tung, K. (2013). Deducing Multidecadal Anthropogenic Global Warming Trends Using
2158 Multiple Regression Analysis [Article]. *Journal of the Atmospheric Sciences*, 70(1), 3-8.
2159 <https://doi.org/10.1175/JAS-D-12-0208.1>
- 2160 Zhu, J., Poulsen, C. J., & Otto-Bliesner, B. L. (2020). High climate sensitivity in CMIP6 model not
2161 supported by paleoclimate. *Nature Climate Change*, 10(5), 378-379.
2162